

**The Vera C. Rubin Observatory Data Preview 1**

1  
2 VERA C. RUBIN OBSERVATORY TEAM,<sup>1</sup> TATIANA ACERO-CUELLAR <sup>2</sup> EMILY ACOSTA <sup>1</sup> CHRISTINA L. ADAIR <sup>3</sup>  
3 PRAKRUTH ADARI <sup>4</sup> JENNIFER K. ADELMAN-McCARTHY <sup>5</sup> ANASTASIA ALEXOV <sup>1</sup> RUSS ALLBERY <sup>1</sup>  
4 ROBYN ALLSMAN,<sup>1</sup> YUSRA ALSAYYAD <sup>6</sup> JHONATAN AMADO <sup>5</sup> NATHAN AMOUROUX <sup>7</sup> PIERRE ANTILOGUS <sup>8</sup>  
5 ALEXIS ARACENA ALCAYAGA,<sup>9</sup> GONZALO ARAVENA-ROJAS <sup>9</sup> CLAUDIO H. ARAYA CORTES,<sup>9</sup> ÉRIC AUBOURG <sup>10</sup>  
6 TIM S. AXELROD <sup>11</sup> JOHN BANOVETZ <sup>12</sup> CARLOS BARRÍA,<sup>9</sup> AMANDA E. BAUER <sup>13</sup> BRIAN J. BAUMAN,<sup>14</sup>  
7 ELLEN BECHTOL <sup>15</sup> KEITH BECHTOL <sup>1,16</sup> ANDREW C. BECKER <sup>17</sup> VALERIE R. BECKER <sup>18</sup> MARK G. BECKETT <sup>19</sup>  
8 ERIC C. BELLM <sup>20</sup> PEDRO H. BERNARDINELLI <sup>21</sup> FEDERICA B. BIANCO <sup>2,22,23</sup> ROBERT D. BLUM <sup>18</sup>  
9 JOANNE BOGART,<sup>24</sup> ADAM BOLTON <sup>3</sup> MICHAEL T. BOOTH,<sup>1</sup> JAMES F. BOSCH <sup>6</sup> ALEXANDRE BOUCAUD <sup>25</sup>  
10 DOMINIQUE BOUTIGNY <sup>7</sup> ROBERT A. BOVILL,<sup>1</sup> ANDREW BRADSHAW,<sup>3,24</sup> JOHAN BREGEON <sup>26</sup> BRIAN J. BRONDEL <sup>27</sup>  
11 ALEXANDER BROUGHTON <sup>24</sup> AUDREY BUDLONG <sup>28</sup> DIMITRI BUFFAT,<sup>26</sup> RODOLFO CANESTRARI <sup>29</sup>  
12 NEVEN CAPLAR <sup>20</sup> JEFFREY L. CARLIN <sup>1</sup> ROSS CEBALLO <sup>18</sup> COLIN ORION CHANDLER <sup>30,20,31</sup>  
13 CHIHWAY CHANG <sup>32</sup> GLENAVER CHARLES-EMERSON,<sup>1</sup> HSIN-FANG CHIANG <sup>3</sup> JAMES CHIANG <sup>24</sup> YUMI CHOI <sup>33</sup>  
14 ERIC J. CHRISTENSEN,<sup>9</sup> CHARLES F. CLAVER,<sup>1</sup> ANDY W. CLEMENTS,<sup>1</sup> JOSEPH J. COCKRUM,<sup>1</sup> FRANCO COLLEONI,<sup>9</sup>  
15 CÉLINE COMBET <sup>26</sup> ANDREW J. CONNOLLY <sup>21</sup> JULIO EDUARDO CONSTANZO CÓRDOVA <sup>9</sup> HANS E CONTRERAS,<sup>9</sup>  
16 JOHN FRANKLIN CRENSHAW <sup>21</sup> SYLVIE DAGORET-CAMPAGNE <sup>34</sup> SCOTT F. DANIEL,<sup>20</sup> FELIPE DARUICH,<sup>9</sup>  
17 GUILLAUME DAUBARD <sup>8</sup> GREG DAUES,<sup>35</sup> ERIK DENNIHY <sup>1</sup> STEPHANIE J. H. DEPPE <sup>18</sup> SETH W. DIGEL <sup>3</sup>  
18 PETER E. DOHERTY,<sup>36</sup> ALEX DRLICA-WAGNER <sup>5</sup> GREGORY P. DUBOIS-FELSMANN <sup>37</sup> FROSSIE ECONOMOU <sup>1</sup>  
19 ORION EIGER <sup>3,24</sup> LUKAS EISERT <sup>3</sup> ALAN M. EISNER <sup>38</sup> ANTHONY ENGLERT <sup>39</sup> BADEN ERB,<sup>9</sup> JUAN A. FABREGA,<sup>9</sup>  
20 PARKER FAGRELIUS,<sup>1</sup> KEVIN FANNING <sup>3</sup> ANGELO FAUSTI NETO <sup>1</sup> PETER S. FERGUSON <sup>21,16</sup> AGNÈS FERTÉ <sup>3</sup>  
21 MERLIN FISHER-LEVINE <sup>40</sup> GLORIA FONSECA ALVAREZ <sup>33</sup> MICHAEL D. FOSS,<sup>3</sup> DOMINIQUE FOUCHEZ <sup>41</sup>  
22 DAN C. FUCHS <sup>3</sup> EMMANUEL GANGLER <sup>42</sup> IGOR GAPONENKO,<sup>3</sup> JULEN GARCIA <sup>43</sup> JOHN H GATES,<sup>3</sup>  
23 RANPAL K. GILL <sup>27</sup> ENRICO GIRO <sup>44</sup> THOMAS GLANZMAN <sup>3</sup> ROBINSON GODOY,<sup>9</sup> IAIN GOODENOW,<sup>1</sup>  
24 MIRANDA R. GORSUCH <sup>16</sup> MICHELLE GOWER <sup>35</sup> MIKAEL GRANVIK <sup>45,46</sup> SARAH GREENSTREET <sup>33</sup> WEN GUAN <sup>12</sup>  
25 THIBAUT GUILLEMIN <sup>7</sup> LEANNE P. GUY <sup>9</sup> DIANE HASCALL,<sup>3</sup> AREN NATHANIEL HEINZE <sup>21</sup> FABIO HERNANDEZ <sup>47</sup>  
26 KENNETH HERNER <sup>5</sup> ARDIS HERROLD,<sup>1</sup> CLARE R. HIGGS <sup>18</sup> JOSHUA HOBLITT <sup>1</sup> ERIN LEIGH HOWARD <sup>20</sup>  
27 MINHEE HYUN <sup>9</sup> PATRICK INGRAHAM <sup>11</sup> DAVID H. IRVING <sup>18</sup> ŽELJKO IVEZIĆ <sup>1,20</sup> SUZANNE H. JACOBY,<sup>1</sup>  
28 BUELL T. JANNUZI <sup>48</sup> SREEVANI JARUGULA <sup>5</sup> M. JAMES JEE <sup>49,50</sup> TIM JENNESS <sup>1</sup> TOBY C. JENNINGS <sup>3</sup>  
29 ANDREA JEREMIE <sup>7</sup> GARRETT JERNIGAN,<sup>51,\*</sup> DAVID JIMÉNEZ MEJÍAS,<sup>9</sup> ANTHONY S. JOHNSON <sup>3</sup> R. LYNNE JONES <sup>20</sup>  
30 ROGER WILLIAM LEWIS JONES <sup>52</sup> CLAIRE JURAMY-GILLES <sup>8</sup> MARIO JURÍĆ <sup>21</sup> STEVEN M. KAHN <sup>53</sup>  
31 J. BRYCE KALMBACH <sup>3</sup> YIJUNG KANG <sup>24,9</sup> ARUN KANAWADI <sup>54,6</sup> JEFFREY P. KANTOR,<sup>1</sup> EDWARD KARAVAKIS <sup>12</sup>  
32 KSHITIJ KALKAR <sup>9</sup> LEE S. KELVIN <sup>6</sup> IVAN V. KOTOV,<sup>12</sup> GÁBOR KOVÁCS <sup>21</sup> MIKOLAJ KOWALIK <sup>35</sup>  
33 VICTOR L. KRABBENDAM,<sup>1</sup> K. SIMON KRUGHOFF <sup>1,\*</sup> PETR KUBÁNEK <sup>9</sup> JACOB A. KURLANDER <sup>21</sup> MILE KUSULJA,<sup>26</sup>  
34 CRAIG S. LAGE <sup>50</sup> PAULO J. A. LAGO <sup>27</sup> KATHERINE LALIOTIS <sup>55</sup> TRAVIS LANGE <sup>3</sup> DIDIER LAPORTE,<sup>8</sup>  
35 RYAN M. LAU <sup>33</sup> JUAN CARLOS LAZARTE,<sup>3</sup> QUENTIN LE BOULC'H <sup>47</sup> PIERRE-FRANÇOIS LÉGET <sup>6</sup>  
36 LAURENT LE GUILLOU <sup>8</sup> BENJAMIN LEVINE <sup>4</sup> MING LIANG,<sup>1</sup> SHUANG LIANG,<sup>3</sup> KIAN-TAT LIM <sup>3</sup>  
37 ANJA VON DER LINDEN <sup>4</sup> HUAN LIN <sup>5</sup> MARGAUX LOPEZ <sup>3</sup> JUAN J. LOPEZ TORO,<sup>9</sup> PETER LOVE,<sup>52</sup>  
38 ROBERT H. LUPTON <sup>6</sup> NATE B. LUST <sup>6</sup> LAUREN A. MACARTHUR <sup>6</sup> SEAN PATRICK MACBRIDE <sup>56</sup>  
39 GREG M. MADEJSKI,<sup>24</sup> GABRIELE MAINETTI <sup>47</sup> STEVEN J. MARGHEIM <sup>27</sup> THOMAS W. MARKIEWICZ <sup>3</sup>  
40 PHIL MARSHALL <sup>3</sup> STUART MARSHALL,<sup>24</sup> GUIDO MAULEN,<sup>9</sup> MORGAN MAY,<sup>57,12</sup> JEREMY McCORMICK <sup>3</sup>  
41 DAVID MCKAY <sup>58</sup> ROBERT MCKERCHER,<sup>1</sup> GUILLEM MEGIAS HOMAR <sup>59</sup> AARON M. MEISNER <sup>33</sup>  
42 FELIPE MENANTEAU,<sup>35</sup> HEATHER R. MENTZER <sup>38</sup> KRISTEN METZGER,<sup>18</sup> JOSHUA E. MEYERS <sup>24</sup> MICHELLE MILLER,<sup>33</sup>  
43 DAVID J. MILLS,<sup>1</sup> JOACHIM MOEYENS <sup>21</sup> MARC MONIEZ,<sup>34</sup> FRED E. MOOLEKAMP <sup>60</sup> C. A. L. MORALES MARÍN <sup>9</sup>  
44 FRITZ MUELLER <sup>3</sup> JAMES R. MULLANEY <sup>61</sup> FREDDY MUÑOZ ARANCIBIA,<sup>1</sup> KATE NAPIER <sup>24</sup> HOMER NEAL,<sup>3</sup>  
45 ERIC H. NEILSEN, JR. <sup>5</sup> JEREMY NEVEU <sup>34</sup> TIMOTHY NOBLE,<sup>62</sup> ERFAN NOURBAKHSH <sup>6</sup> KNUT OLSEN <sup>33</sup>  
46 WILLIAM O'MULLANE <sup>9</sup> DMITRY ONOPRIENKO,<sup>3</sup> MARCO ORIUNNO <sup>3</sup> SHAWN OSIER,<sup>3</sup> RUSSELL E. OWEN,<sup>20</sup>  
47 AASHAY PAI <sup>32</sup> JOHN K. PAREJKO <sup>20</sup> HYE YUN PARK <sup>54</sup> JAMES B. PARSONS,<sup>35,\*</sup> MARIA T. PATTERSON <sup>20</sup>  
48 MARINA S. PAVLOVIC <sup>9</sup> KARLA PEÑA RAMÍREZ <sup>9</sup> JOHN R. PETERSON <sup>63</sup> STEPHEN R. PIETROWICZ <sup>35</sup>  
49 ANDRÉS A. PLAZAS MALAGÓN <sup>3,24</sup> REBEKAH POLEN,<sup>54</sup> HANNAH MARY MARGARET POLLEK,<sup>3</sup> PAUL A. PRICE <sup>6</sup>

BRUNO C. QUINT <sup>1</sup>, JOSÉ MIGUEL QUINTERO MARIN,<sup>9</sup> MARKUS RABUS <sup>64</sup>, BENJAMIN RACINE <sup>41</sup>, VELJKO RADEKA,<sup>12</sup>  
 MANON RAMEL,<sup>26</sup> ARIANNA RANABHAT <sup>65</sup>, ANDREW P. RASMUSSEN <sup>24</sup>, DAVID A. RATHFELDER,<sup>66</sup>  
 MEREDITH L. RAWLS <sup>20,21</sup>, SOPHIE L. REED <sup>6</sup>, KEVIN A. REIL <sup>3</sup>, DAVID J. REISS,<sup>20</sup> MICHAEL A. REUTER <sup>1</sup>,  
 TIAGO RIBEIRO <sup>1</sup>, MICKAEL RIGAUT <sup>67</sup>, VINCENT J. RIOT <sup>14</sup>, STEVEN M. RITZ <sup>38</sup>, MARIO F. RIVERA RIVERA,<sup>9</sup>  
 BRANT E. ROBERTSON <sup>38</sup>, WILLIAM ROBY <sup>37</sup>, GABRIELE RODEGHIERO <sup>68</sup>, AARON ROODMAN <sup>24</sup>,  
 LUCA ROSIGNOLI <sup>69,68</sup>, CÉCILE ROUCELLE <sup>25</sup>, MATTHEW R. RUMORE <sup>12</sup>, STEFANO RUSSO,<sup>8</sup> ELI S. RYKOFF <sup>24</sup>,  
 ANDREI SALNIKOV <sup>3</sup>, BRUNO O. SÁNCHEZ <sup>41</sup>, DAVID SANMARTIN <sup>9</sup>, CLARE SAUNDERS <sup>6</sup>, RAFE H. SCHINDLER,<sup>24</sup>  
 SAMUEL J. SCHMIDT <sup>50</sup>, JACQUES SEBAG,<sup>9</sup> BRIAN SELVY,<sup>1</sup> EDGARD ESTEBAN SEPULVEDA VALENZUELA,<sup>9</sup>  
 GONZALO SERICHE <sup>9</sup>, JACQUELINE C. SERON-NAVARETE <sup>9</sup>, IGNACIO SEVILLA-NOARBE <sup>70</sup>, ALYSHA SHUGART <sup>9</sup>,  
 JONATHAN SICK <sup>71,1</sup>, CRISTIÁN SILVA <sup>9</sup>, MATHEW C. SIMS <sup>72</sup>, JALADH SINGHAL <sup>37</sup>, KEVIN BENJAMIN SIRUNO,<sup>9</sup>  
 COLIN T. SLATER <sup>20</sup>, BRIANNA M. SMART <sup>20</sup>, ADAM SNYDER <sup>50</sup>, CHRISTINE SOLDAHL,<sup>3</sup>  
 IOANA SOTUELA ELORRIAGA <sup>9</sup>, BRIAN STALDER <sup>1</sup>, HERNAN STOCKEBRAND <sup>9</sup>, ALAN L. STRAUSS <sup>18</sup>,  
 MICHAEL A. STRAUSS <sup>6</sup>, KRZYSZTOF SUBERLAK <sup>20</sup>, IAN S. SULLIVAN <sup>20</sup>, JOHN D. SWINBANK <sup>73,6</sup>, DIEGO TAPIA <sup>9</sup>,  
 ALESSIO TARANTO <sup>68,69</sup>, DAN S. TARANU <sup>6</sup>, JOHN GREGG THAYER <sup>3</sup>, SANDRINE THOMAS <sup>1</sup>,  
 ADAM J. THORNTON <sup>1</sup>, ROBERTO TIGHE,<sup>9</sup> LAURA TORIBIO SAN CIPRIANO,<sup>70</sup> TE-WEI TSAI <sup>1</sup>, DOUGLAS L. TUCKER <sup>5</sup>,  
 MAX TURRI,<sup>3</sup> J. ANTHONY TYSON <sup>50</sup>, ELANA K. URBACH <sup>74</sup>, YOUSUKE UTSUMI <sup>75</sup>, BRIAN VAN KLAVEREN,<sup>3</sup>  
 WOUTER VAN REEVEN <sup>9</sup>, PETER ANTHONY VAUCHER <sup>3</sup>, PAULINA VENEGAS,<sup>9</sup> APRAJITA VERMA <sup>76</sup>,  
 ANTONIA SIERRA VILLARREAL <sup>3</sup>, STELIOS VOUTSINAS <sup>1</sup>, CHRISTOPHER W. WALTER <sup>54</sup>, YUANKUN (DAVID) WANG <sup>21</sup>,  
 CHRISTOPHER Z. WATERS <sup>6</sup>, CHRISTINA C. WILLIAMS <sup>33</sup>, BETH WILLMAN <sup>77</sup>, MATTHIAS WITTGEN <sup>3</sup>,  
 W. M. WOOD-VASEY <sup>78</sup>, WEI YANG <sup>3</sup>, ZHAOYU YANG <sup>12</sup>, BRIAN P. YANNY <sup>5</sup>, PETER YOACHIM <sup>20</sup>,  
 TIANQING ZHANG <sup>78</sup> AND CONGHAO ZHOU <sup>38</sup>

<sup>1</sup> Vera C. Rubin Observatory Project Office, 950 N. Cherry Ave., Tucson, AZ 85719, USA

<sup>2</sup> Department of Physics and Astronomy, University of Delaware, Newark, DE 19716-2570, USA

<sup>3</sup> SLAC National Accelerator Laboratory, 2575 Sand Hill Rd., Menlo Park, CA 94025, USA

<sup>4</sup> Department of Physics and Astronomy, Stony Brook University, Stony Brook, NY 11794, USA

<sup>5</sup> Fermi National Accelerator Laboratory, P. O. Box 500, Batavia, IL 60510, USA

<sup>6</sup> Department of Astrophysical Sciences, Princeton University, Princeton, NJ 08544, USA

<sup>7</sup> Université Savoie Mont-Blanc, CNRS/IN2P3, LAPP, 9 Chemin de Bellevue, F-74940 Annecy-le-Vieux, France

<sup>8</sup> Sorbonne Université, Université Paris Cité, CNRS/IN2P3, LPNHE, 4 place Jussieu, F-75005 Paris, France

<sup>9</sup> Vera C. Rubin Observatory, Avenida Juan Cisternas #1500, La Serena, Chile

<sup>10</sup> Université Paris Cité, CNRS/IN2P3, CEA, APC, 4 rue Elsa Morante, F-75013 Paris, France

<sup>11</sup> Steward Observatory, The University of Arizona, 933 N. Cherry Ave., Tucson, AZ 85721, USA

<sup>12</sup> Brookhaven National Laboratory, Upton, NY 11973, USA

<sup>13</sup> Yerkes Observatory, 373 W. Geneva St., Williams Bay, WI 53191, USA

<sup>14</sup> Lawrence Livermore National Laboratory, 7000 East Avenue, Livermore, CA 94550, USA

<sup>15</sup> Wisconsin IceCube Particle Astrophysics Center, University of Wisconsin—Madison, Madison, WI 53706, USA

<sup>16</sup> Department of Physics, University of Wisconsin-Madison, Madison, WI 53706, USA

<sup>17</sup> Amazon Web Services, Seattle, WA 98121, USA

<sup>18</sup> Vera C. Rubin Observatory/NSF NOIRLab, 950 N. Cherry Ave., Tucson, AZ 85719, USA

<sup>19</sup> Institute for Astronomy, University of Edinburgh, Royal Observatory, Blackford Hill, Edinburgh EH9 3HJ, UK

<sup>20</sup> University of Washington, Dept. of Astronomy, Box 351580, Seattle, WA 98195, USA

<sup>21</sup> Institute for Data-intensive Research in Astrophysics and Cosmology, University of Washington, 3910 15th Avenue NE, Seattle, WA 98195, USA

<sup>22</sup> Joseph R. Biden, Jr., School of Public Policy and Administration, University of Delaware, Newark, DE 19717 USA

<sup>23</sup> Data Science Institute, University of Delaware, Newark, DE 19717 USA

<sup>24</sup> Kavli Institute for Particle Astrophysics and Cosmology, SLAC National Accelerator Laboratory, 2575 Sand Hill Rd., Menlo Park, CA 94025, USA

<sup>25</sup> Université Paris Cité, CNRS/IN2P3, APC, 4 rue Elsa Morante, F-75013 Paris, France

<sup>26</sup> Université Grenoble Alpes, CNRS/IN2P3, LPSC, 53 avenue des Martyrs, F-38026 Grenoble, France

<sup>27</sup> Vera C. Rubin Observatory/NSF NOIRLab, Casilla 603, La Serena, Chile

<sup>28</sup> University of Washington, Dept. of Physics, Box 351580, Seattle, WA 98195, USA

<sup>29</sup> INAF Istituto di Astrofisica Spaziale e Fisica Cosmica di Palermo, Via Ugo la Malfa 153, 90146, Palermo, Italy

<sup>30</sup> LSST Interdisciplinary Network for Collaboration and Computing, Tucson, USA

<sup>31</sup> Department of Astronomy and Planetary Science, Northern Arizona University, P.O. Box 6010, Flagstaff, AZ 86011, USA

<sup>32</sup> Department of Astronomy and Astrophysics, University of Chicago, 5640 South Ellis Avenue, Chicago, IL 60637, USA

<sup>33</sup> NSF NOIRLab, 950 N. Cherry Ave., Tucson, AZ 85719, USA

- 106 <sup>34</sup> *Université Paris-Saclay, CNRS/IN2P3, IJCLab, 15 Rue Georges Clemenceau, F-91405 Orsay, France*  
 107 <sup>35</sup> *NCSA, University of Illinois at Urbana-Champaign, 1205 W. Clark St., Urbana, IL 61801, USA*  
 108 <sup>36</sup> *Smithsonian Astrophysical Observatory, 60 Garden St., Cambridge MA 02138, USA*  
 109 <sup>37</sup> *Caltech/IPAC, California Institute of Technology, MS 100-22, Pasadena, CA 91125-2200, USA*  
 110 <sup>38</sup> *Santa Cruz Institute for Particle Physics and Physics Department, University of California–Santa Cruz, 1156 High St., Santa Cruz,*  
 111 *CA 95064, USA*  
 112 <sup>39</sup> *Department of Physics, Brown University, 182 Hope Street, Providence, RI 02912, USA*  
 113 <sup>40</sup> *D4D CONSULTING LTD., Suite 1 Second Floor, Everdene House, Deansleigh Road, Bournemouth, UK BH7 7DU*  
 114 <sup>41</sup> *Aix Marseille Université, CNRS/IN2P3, CPPM, 163 avenue de Luminy, F-13288 Marseille, France*  
 115 <sup>42</sup> *Université Clermont Auvergne, CNRS/IN2P3, LPCA, 4 Avenue Blaise Pascal, F-63000 Clermont-Ferrand, France*  
 116 <sup>43</sup> *C. Iñaki Goenaga, 5, 20600, Guipúzcoa, Spain*  
 117 <sup>44</sup> *INAF Osservatorio Astronomico di Trieste, Via Giovan Battista Tiepolo 11, 34143, Trieste, Italy*  
 118 <sup>45</sup> *Department of Physics, P.O. Box 64, 00014 University of Helsinki, Finland*  
 119 <sup>46</sup> *Asteroid Engineering Laboratory, Luleå University of Technology, Box 848, SE-981 28 Kiruna, Sweden*  
 120 <sup>47</sup> *CNRS/IN2P3, CC-IN2P3, 21 avenue Pierre de Coubertin, F-69627 Villeurbanne, France*  
 121 <sup>48</sup> *University of Arizona, Department of Astronomy and Steward Observatory, 933 N. Cherry Ave, Tucson, AZ 85721, USA*  
 122 <sup>49</sup> *Department of Astronomy, Yonsei University, 50 Yonsei-ro, Seoul 03722, Republic of Korea*  
 123 <sup>50</sup> *Physics Department, University of California, One Shields Avenue, Davis, CA 95616, USA*  
 124 <sup>51</sup> *Space Sciences Lab, University of California, 7 Gauss Way, Berkeley, CA 94720-7450, USA*  
 125 <sup>52</sup> *Lancaster University, Lancaster, UK*  
 126 <sup>53</sup> *Physics Department, University of California, 366 Physics North, MC 7300 Berkeley, CA 94720, USA*  
 127 <sup>54</sup> *Department of Physics, Duke University, Durham, NC 27708, USA*  
 128 <sup>55</sup> *Center for Cosmology and Astro-Particle Physics, The Ohio State University, Columbus, OH 43210, USA*  
 129 <sup>56</sup> *Physik-Institut, University of Zurich, Winterthurerstrasse 190, 8057 Zurich, Switzerland*  
 130 <sup>57</sup> *Department of Physics Columbia University, New York, NY 10027, USA*  
 131 <sup>58</sup> *EPCC, University of Edinburgh, 47 Potterrow, Edinburgh, EH8 9BT, UK*  
 132 <sup>59</sup> *Division of Physics, Mathematics and Astronomy, California Institute of Technology, Pasadena, CA 91125, USA*  
 133 <sup>60</sup> *soZen Inc., 105 Clearview Dr, Penfield, NY 14526*  
 134 <sup>61</sup> *Astrophysics Research Cluster, School of Mathematical and Physical Sciences, University of Sheffield, Sheffield, S3 7RH, United*  
 135 *Kingdom*  
 136 <sup>62</sup> *Science and Technology Facilities Council, Rutherford Appleton Laboratory, Harwell, UK*  
 137 <sup>63</sup> *Department of Physics and Astronomy, Purdue University, 525 Northwestern Ave., West Lafayette, IN 47907, USA*  
 138 <sup>64</sup> *Departamento de Matemática y Física Aplicadas, Facultad de Ingeniería, Universidad Católica de la Santísima Concepción, Alonso de*  
 139 *Rivera 2850, Concepción, Chile*  
 140 <sup>65</sup> *Australian Astronomical Optics, Macquarie University, North Ryde, NSW, Australia*  
 141 <sup>66</sup> *AURA, 950 N. Cherry Ave., Tucson, AZ 85719, USA*  
 142 <sup>67</sup> *Université Claude Bernard Lyon 1, CNRS/IN2P3, IP2I, 4 Rue Enrico Fermi, F-69622 Villeurbanne, France*  
 143 <sup>68</sup> *INAF Osservatorio di Astrofisica e Scienza dello Spazio Bologna, Via P. Gobetti 93/3, 40129, Bologna, Italy*  
 144 <sup>69</sup> *Department of Physics and Astronomy (DIFA), University of Bologna, Via P. Gobetti 93/2, 40129, Bologna, Italy*  
 145 <sup>70</sup> *Centro de Investigaciones Energéticas, Medioambientales y Tecnológicas, Av. Complutense 40, 28040 Madrid, Spain*  
 146 <sup>71</sup> *J.Sick Codes Inc., Penetanguishene, Ontario, Canada*  
 147 <sup>72</sup> *Science and Technology Facilities Council, UK Research and Innovation, Polaris House, North Star Avenue, Swindon, SN2 1SZ, UK*  
 148 <sup>73</sup> *ASTRON, Oude Hoogeveensedijk 4, 7991 PD, Dwingeloo, The Netherlands*  
 149 <sup>74</sup> *Department of Physics, Harvard University, 17 Oxford St., Cambridge MA 02138, USA*  
 150 <sup>75</sup> *National Astronomical Observatory of Japan, Chile Observatory, Los Abedules 3085, Vitacura, Santiago, Chile*  
 151 <sup>76</sup> *Department of Physics, University of Oxford, Denys Wilkinson Building, Keble Road, Oxford, OX1 3RH, UK*  
 152 <sup>77</sup> *LSST Discovery Alliance, 933 N. Cherry Ave., Tucson, AZ 85719, USA*  
 153 <sup>78</sup> *Department of Physics and Astronomy, University of Pittsburgh, 3941 O'Hara Street, Pittsburgh, PA 15260, USA*

(Dated: January 29, 2026)

## ABSTRACT

We present Rubin Data Preview 1 (DP1), the first data from the NSF-DOE Vera C. Rubin Observatory, comprising raw and calibrated single-epoch images, coadds, difference images, detection catalogs, and ancillary data products. DP1 is based on 1792 optical/near-infrared exposures acquired over 48 distinct nights by the Rubin Commissioning Camera, LSSTComCam, on the Si-

159 monyi Survey Telescope at the Summit Facility on Cerro Pachón, Chile in late 2024. DP1 covers  
 160  $\sim 15$  deg<sup>2</sup> distributed across seven roughly equal-sized non-contiguous fields, each independently ob-  
 161 served in six broad photometric bands, *ugrizy*. The median FWHM of the point-spread function  
 162 across all bands is approximately 1''14, with the sharpest images reaching about 0''58. The  $5\sigma$  point  
 163 source depths for coadded images in the deepest field, Extended Chandra Deep Field South, are:  
 164  $u = 24.55, g = 26.18, r = 25.96, i = 25.71, z = 25.07, y = 23.1$ . Other fields are no more than 2.2  
 165 magnitudes shallower in any band, where they have nonzero coverage. DP1 contains approximately  
 166 2.3 million distinct astrophysical objects, of which 1.6 million are extended in at least one band in  
 167 coadds, and 431 solar system objects, of which 93 are new discoveries. DP1 is approximately 3.5 TB  
 168 in size and is available to Rubin data rights holders via the Rubin Science Platform, a cloud-based  
 169 environment for the analysis of petascale astronomical data. While small compared to future LSST  
 170 releases, its high quality and diversity of data support a broad range of early science investigations  
 171 ahead of full operations in late 2025.

172 *Keywords:* Rubin Observatory – LSST

## 173 1. INTRODUCTION

174 The National Science Foundation (NSF)–Department  
 175 of Energy (DOE) Vera C. Rubin Observatory is a  
 176 ground-based, wide-field optical/near-infrared facility  
 177 located on Cerro Pachón in northern Chile. Named in  
 178 honor of Vera C. Rubin, a pioneering astronomer whose  
 179 groundbreaking work in the 20th century provided the  
 180 first convincing evidence for the existence of dark mat-  
 181 ter (V. C. Rubin & W. K. Ford 1970; V. C. Rubin et al.  
 182 1980), the observatory’s prime mission is to carry out the  
 183 Legacy Survey of Space and Time (formerly Large Syn-  
 184 optic Survey Telescope) (LSST) (Ž. Ivezić et al. 2019a).  
 185 This 10-year survey is designed to obtain rapid-cadence,  
 186 multi-band imaging of the entire visible southern sky  
 187 approximately every 3–4 nights. Over its main 18,000  
 188 deg<sup>2</sup> footprint, the LSST is expected to reach a depth  
 189 of  $\sim 27$  magnitude in the r-band, with  $\sim 800$  visits per  
 190 pointing in all filters (F. B. Bianco et al. 2022).

191 The Rubin Observatory system consists of four main  
 192 components: the *Simonyi Survey Telescope*, featuring  
 193 an 8.4 m diameter (6.5 m effective aperture) primary  
 194 mirror that delivers a wide field of view; a 3.2-gigapixel  
 195 camera, capable of imaging 9.6 square degrees per ex-  
 196 posure<sup>79</sup> with seeing-limited quality in six broadband  
 197 filters, *ugrizy* (320–1050 nm); an automated *Data Man-*  
 198 *agement System* that processes and archives tens of ter-  
 199 abytes of data per night, generating science-ready data  
 200 products within minutes for a global community of sci-  
 201 entists; and an *Education and Public Outreach (EPO)*

202 program that provides real-time data access, interactive  
 203 tools, and educational content to engage the public. The  
 204 integrated system’s étendue<sup>80</sup> of 319 m<sup>2</sup> deg<sup>2</sup>, is over an  
 205 order of magnitude larger than that of any previous op-  
 206 tical observatory, enabling a fast, large-scale survey with  
 207 exceptional depth in a fraction of the time compared to  
 208 other observatories.

209 The observatory’s design is driven by four key science  
 210 themes: probing dark energy and dark matter; taking  
 211 an inventory of the solar system; exploring the tran-  
 212 sient and variable optical sky; and mapping the Milky  
 213 Way (Ž. Ivezić et al. 2019a). These themes inform the  
 214 optimization of a range of system parameters, includ-  
 215 ing image quality, photometric and astrometric accu-  
 216 racy, the depth of a single visit and the co-added survey  
 217 depth, the filter complement, the total number of visits  
 218 per pointing as well as the distribution of visits on the  
 219 sky, and total sky coverage. Additionally, they inform  
 220 the design of the data processing and access systems.  
 221 By optimizing the system parameters to support a wide  
 222 range of scientific goals, we maximize the observatory’s  
 223 scientific output across all areas, making Rubin a pow-  
 224 erful discovery machine capable of addressing a broad  
 225 range of astrophysical questions.

226 Throughout the duration of the LSST, Rubin Obser-  
 227 vatory will issue a series of Data Releases, each repre-  
 228 senting a complete reprocessing of all LSST data col-  
 229 lected up to that point. Prior to the start of the LSST  
 230 survey, commissioning activities will generate a signifi-  
 231 cant volume of science-grade data. To make this early  
 232 data available to the community, the Rubin Early Sci-  
 233 ence Program (L. P. Guy et al. 2026) was established.

\* Author is deceased

<sup>79</sup> We define an “exposure” as the process of exposing all detectors in the focal plane. It is synonymous with the term “visit” in *Data Preview 1 (DP1)*. By contrast, an “image” is the output of a single detector following an exposure.

<sup>80</sup> The product of the primary mirror area and the angular area of its field of view for a given set of observing conditions.

234 One key component of this program is a series of Data  
 235 Previews; early versions of the [LSST Data Releases](#).  
 236 These previews include preliminary data products derived  
 237 from both simulated and commissioning data,  
 238 which, together with early versions of the data access  
 239 services, are intended to support high-impact early sci-  
 240 ence, facilitate community readiness, and inform the de-  
 241 velopment of Rubin’s operational capabilities ahead of  
 242 the start of full survey operations. All data and services  
 243 provided through the Rubin Early Science Program are  
 244 offered on a shared-risk basis <sup>81</sup>.

245 This paper describes Rubin’s second of three planned  
 246 Data Previews: [DP1 \(NSF-DOE Vera C. Rubin Observa-](#)  
 247 [tory 2025a\)](#). The first, [Data Preview 0 \(DP0\)](#), con-  
 248 tained data products produced from the processing of  
 249 simulated [LSST-like](#) data sets. These were released to-  
 250 gether with a very early version of the Rubin [Science](#)  
 251 [Platform \(M. Jurić et al. 2019\)](#), which provided the data  
 252 access services. [DP0](#) was released in multiple phases;  
 253 [DP0.1](#), [DP0.2](#), and [DP0.3](#), each building upon the pre-  
 254 vious and incorporating new data and functionalities.  
 255 [DP0.1](#) and [DP0.2](#) uses data from the [cosmoDC2](#) simula-  
 256 tions ([LSST Dark Energy Science Collaboration \(LSST](#)  
 257 [DESC\) et al. 2021\)](#) prepared by the Dark Energy Science  
 258 Collaboration ([DESC](#)), whereas [DP0.3](#) is based on simu-  
 259 lated datasets from the [Solar System Science Collabora-](#)  
 260 [tion \(SSSC\)](#). Online documentation for [DP0](#) is available  
 261 at <https://dp0.lsst.io>.

262 [DP1](#) contains data products derived from the repro-  
 263 cessing of science-grade exposures acquired by the [Ru-](#)  
 264 [bin Commissioning Camera \(LSSTComCam\)](#), in late  
 265 2024. The third and final Data Preview, [Data Preview](#)  
 266 [2 \(DP2\)](#), is planned to be based on a reprocessing of all  
 267 science-grade data taken with the Rubin’s [LSST Science](#)  
 268 [Camera \(LSSTCam\)](#) during commissioning.

269 All Rubin Data Releases and Previews are subject  
 270 to a two-year proprietary period, with immediate ac-  
 271 cess granted exclusively to LSST data rights holders  
 272 ([R. Blum & the Rubin Operations Team 2020](#)). Data  
 273 rights holders <sup>82</sup>See <https://www.lsst.org/scientists/>  
 274 [international-drh-list](#) are individuals or institutions with  
 275 formal authorization to access proprietary data collected  
 276 by the Vera C. Rubin Observatory. After the two-year  
 277 proprietary period, [DP1](#) will be made public. However,  
 278 even once the data become public, access for non-data  
 279 rights holders will not be provided through Rubin Data

280 Access Centers in the US and Chile ([R. Blum & the Ru-](#)  
 281 [bin Operations Team 2020](#)). Alternative access mecha-  
 282 nisms are still under discussion and have not yet been  
 283 finalized.

284 In this paper, we describe the contents and valida-  
 285 tion of Rubin [DP1](#), the first Data Preview to deliver  
 286 data derived from observations conducted by the Vera  
 287 C. Rubin Observatory, as well as the data-access mecha-  
 288 nisms and community-support services that accompany  
 289 it. [DP1](#) is based on the reprocessing of 1792 science-  
 290 grade exposures acquired during the first on-sky com-  
 291 missioning campaign, conducted over 48 nights between  
 292 2024-10-24 and 2024-12-11. It covers a total area of  
 293 approximately  $\sim 15$  deg<sup>2</sup> distributed across seven dis-  
 294 tinct non-contiguous fields. The data products include  
 295 raw and calibrated single-epoch images, coadded images,  
 296 difference images, detection catalogs, and other derived  
 297 data products. [DP1](#) is about 3.5 TB in size and con-  
 298 tains around 2.3 million distinct astronomical objects,  
 299 detected in 2644 coadded images. Full [DP1](#) release doc-  
 300 umentation is available at <https://dp1.lsst.io>. Despite  
 301 Rubin Observatory still being in commissioning and not  
 302 yet complete at the time the observations were acquired,  
 303 Rubin [DP1](#) provides an important first look at the data,  
 304 showcasing its characteristics and capabilities.

305 The structure of this paper is as follows. In section  
 306 2 we describe the observatory system and overall con-  
 307 struction and commissioning status at the time of data  
 308 acquisition, the seven fields included in [DP1](#), and the  
 309 observing strategy used. Section 3 summarizes the con-  
 310 tents of [DP1](#) and the data products contained in the  
 311 release. The data processing pipelines are described in  
 312 section 4, followed by a description of the data valida-  
 313 tion and performance assessment in section 5. Section  
 314 6 describes the Rubin [Science Platform \(RSP\)](#), a cloud-  
 315 based data science infrastructure that provides tools and  
 316 services to Rubin data rights holders to access, visual-  
 317 ize and analyze peta-scale data generated by the [LSST](#).  
 318 Section 7 presents the Rubin Observatory’s model for  
 319 community support, which emphasizes self-help via doc-  
 320 umentation and tutorials, and employs an open platform  
 321 for issue reporting that enables crowd-sourced solutions.  
 322 Finally, a summary of the [DP1](#) release and information  
 323 on expected future releases of data is given in section 8.  
 324 The appendix contains a useful glossary of terms used  
 325 throughout this paper.

326 All magnitudes quoted are in the AB system ([J. B.](#)  
 327 [Oke & J. E. Gunn 1983](#)), unless otherwise specified.

## 328 2. ON-SKY COMMISSIONING CAMPAIGN

329 The first Rubin on-sky commissioning campaign was  
 330 conducted using the [LSSTComCam](#). The campaign’s

<sup>81</sup> Shared risk means early access with caveats: the community benefits from getting a head start on science, preparing analyses, and providing feedback, while also accepting that the system may not work as well as it will during full operations.

<sup>82</sup> (

primary objective was to optically align the Simonyi Survey Telescope and verify its ability to deliver acceptable image quality using *LSSTComCam*. In addition, the campaign provided valuable operations experience to facilitate commissioning the full *LSSTCam* (T. Lange et al. 2024; A. Roodman et al. 2024). We note that commissioning *LSSTComCam* was not an objective of the campaign. Instead, *LSSTComCam* was used as a tool to support broader observatory commissioning, including early testing of the *Active Optics System* (AOS) and the LSST Science Pipelines. As a result, many artifacts present in the data are specific to *LSSTComCam* and will be addressed only if they persist with *LSSTCam*. Accordingly, the image quality achieved during this campaign, and in the *DP1* data, may not reflect the performance ultimately expected from *LSSTCam*.

Approximately 16,000 exposures<sup>83</sup> were collected during this campaign, the majority in support of AOS commissioning, system-level verification, and end-to-end testing of the telescope’s hardware and software. This included over 10000 exposures for AOS commissioning, more than 2000 bias and dark calibration frames, and over 2000 exposures dedicated to commissioning the LSST Science Pipelines. For *DP1*, we have selected a subset of 1792 science-grade exposures from this campaign that are most useful for the community to begin preparing for early science.

At the time of the campaign, the observatory was still under construction, with several key components, such as dome thermal control, full mirror control, and the final AOS configuration either incomplete or still undergoing commissioning. As a result, image quality varied widely throughout the campaign and exhibited a broader distribution than is expected with *LSSTCam*. Despite these limitations, the campaign successfully demonstrated system integration and established a functional observatory.

### 2.1. *Simonyi Survey Telescope*

The Simonyi Survey Telescope (B. Stalder et al. 2024) features a unique three-mirror design, including an 8.4-meter *Primary Mirror Tertiary Mirror* (M1M3) fabricated from a single substrate and a 3.5-meter *Secondary Mirror* (M2). This compact configuration supports a wide 3.5-degree field of view while enabling exceptional stability, allowing the telescope to slew and settle in under five seconds. To achieve the scientific goals of the

10-year *LSST*, the Observatory must maintain high image quality across its wide field of view (Ž. Ivezić et al. 2019b). This is accomplished through the AOS (B. Xin et al. 2015; G. Megias Homar et al. 2024), which corrects, between successive exposures, wavefront distortions caused by optical misalignments and mirror surface deformations, primarily due to the effect of gravitational and thermal loads.

The AOS, which comprises an open-loop component and a closed-loop component, optimizes image quality by aligning the camera and M2 relative to M1M3, as well as adjusting the shapes of all three mirrors to nanometer precision. The AOS open-loop component corrects for predictable distortions and misalignments, while the closed-loop component addresses unpredictable or slowly varying aberrations using feedback from the corner wavefront sensors. The closed-loop wavefront sensing technique is curvature wavefront sensing, which infers wavefront errors in the optical system by analyzing extra- and intra-focal star images (S. Thomas et al. 2023). Since *LSSTComCam* lacks dedicated wavefront sensors, wavefront errors were instead estimated by defocusing the telescope  $\pm 1.5$  mm on either side of focus and applying the curvature wavefront sensing pipeline to the resulting images. Each night began with an initial alignment correction using a laser tracker to position the system within the capture range of the closed-loop algorithm (G. Megias Homar et al. 2024). Once this coarse alignment was complete, the AOS refined the optical alignment and applied mirror surfaces corrections to optimize the image quality across the *LSSTComCam* field of view.

During *LSST Science Pipelines* commissioning (§2.4), observations were conducted using the AOS in open-loop mode only, without closed-loop corrections between exposures. Closed-loop operation, which requires additional intra- and extra-focal images with *LSSTComCam*, was not compatible with the continuous data acquisition needed by the pipelines. The image quality for these data was monitored by measuring the *Point Spread Function* (PSF) *Full Width at Half-Maximum* (FWHM), and closed-loop sequences were periodically run when image quality degradation was observed.

### 2.2. *The LSST Commissioning Camera*

*LSSTComCam* (B. Stalder et al. 2022, 2020; J. Howard et al. 2018; SLAC National Accelerator Laboratory & NSF-DOE Vera C. Rubin Observatory 2024) is a 144-megapixel version of the 3.2-gigapixel *LSSTCam*. It covers approximately 5% of the *LSSTCam* focal plane area, with a field of view of  $\sim 0.5$  deg<sup>2</sup> ( $40' \times 40'$ ), compared to *LSSTCam*’s 9.6 deg<sup>2</sup>. It was developed to val-

<sup>83</sup> We define an exposure as the process of exposing all *LSSTComCam* detectors. It is synonymous with visit in *DP1*. By contrast, an image is the output of a single *LSSTComCam* detector following an exposure.

428 idate camera interfaces with other observatory compo-  
 429 nents and evaluate overall system performance prior to  
 430 the start of **LSSTCam** commissioning. Although **LSST-**  
 431 **ComCam** has a smaller imaging area, it shares the same  
 432 plate scale of  $0''.2$  per pixel and is housed in a support  
 433 structure that replicates the mass, center of gravity, and  
 434 physical dimensions of **LSSTCam**. All mechanical and  
 435 utility interfaces to the telescope are implemented iden-  
 436 tically, enabling full end-to-end testing of observatory  
 437 systems, including readout electronics, image acquisi-  
 438 tion, and data pipelines. Although the **LSSTComCam**  
 439 cryostat employs a different cooling system (Cryotels) to  
 440 that of **LSSTCam**, it included a refrigeration pathfinder  
 441 to validate the cryogenic system intended for **LSSTCam**.

442 The **LSSTCam** focal plane comprises 25 modular rafts  
 443 arranged in a  $5 \times 5$  grid, of which 21 are science rafts de-  
 444 dicated to imaging and 4 are corner rafts used for guid-  
 445 ing and wavefront sensing. **LSSTCam** employs CCD  
 446 sensors from two vendors: **Imaging Technology Labora-**  
 447 **tory, University of Arizona (UA)** (ITL) and **Teledyne**  
 448 **(E2V)**. In contrast, **LSSTComCam** contains only a sin-  
 449 gle science raft equipped exclusively with ITL sensors.  
 450 **Figure 1** presents a schematic of the **LSSTCam** focal  
 451 plane, with the **LSSTComCam** raft positioned at the  
 452 center, corresponding to the **LSSTCam** central science  
 453 raft location. The perspective is from above, looking  
 454 down through the **LSSTComCam** lenses onto the focal  
 455 plane.

456 Each science raft is a self-contained unit compris-  
 457 ing nine  $4K \times 4K$  **Charge-Coupled Device (CCD)** (G. E.  
 458 **Smith 2010**) sensors arranged in a  $3 \times 3$  mosaic, complete  
 459 with integrated readout electronics and cooling systems.  
 460 Each sensor is subdivided into 16 segments arranged in  
 461 a  $2 \times 8$  layout, with each segment consisting of  $512 \times 2048$   
 462 pixels and read out in parallel using individual ampli-  
 463 fiers. This design is identical across all science rafts.  
 464 To maintain uniform performance and **calibration**, each  
 465 raft is populated exclusively with sensors from a single  
 466 vendor.

467 **LSSTComCam** consists of a single science raft, desig-  
 468 nated Raft 22 (R22), equipped solely with ITL sensors.  
 469 These sensors were selected from the best-performing re-  
 470 maining ITL devices after the **LSSTCam** rafts were fully  
 471 populated. Some exhibit known issues such as high read-  
 472 out noise (e.g., Detector 8) and elevated **Charge Transfer**  
 473 **Inefficiency (CTI)** (e.g., Detector 5). Consequently, cer-  
 474 tain image artifacts present in the **DP1** dataset may be  
 475 specific to **LSSTComCam**. **Figure 2** shows the **LSST-**  
 476 **ComCam** R22 focal plane layout and the placement and  
 477 numbering scheme of sensors (S) and amplifiers (C).  
 478 This configuration is identical across all science rafts  
 479 in **LSSTCam**. The **LSSTCam** and **LSSTComCam** focal

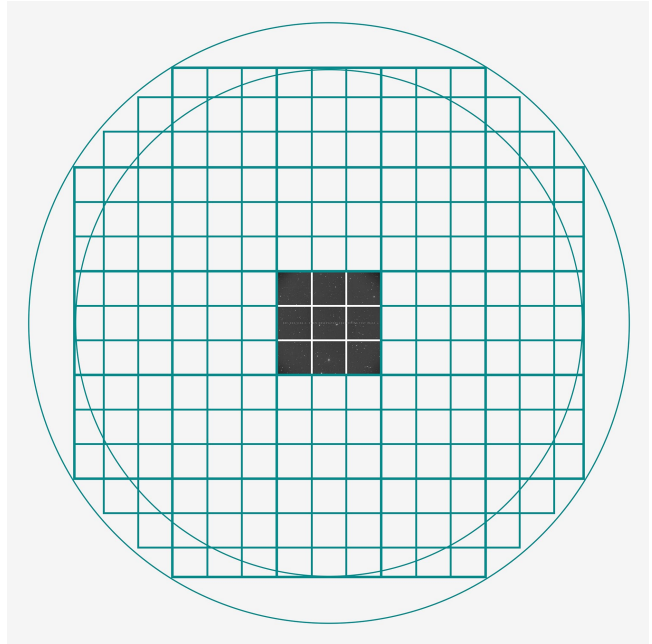


**Figure 1.** **LSSTComCam** focal plane layout illustrating the placement and numbering scheme of sensors (S) and amplifiers (C). The view is looking down from above the focal plane through the **LSSTComCam** lenses. Each sensor contains 16 amplifiers, and a group of nine sensors comprises one raft. **LSSTComCam** is Raft 22 (R22). The detector number for each sensor is shown in parentheses.

481 planes are described in detail in A. A. Plazas Malagón  
 482 et al. (2025).

#### 483 2.2.1. Filter Complement

484 **LSSTComCam** supports imaging with six broadband  
 485 filters *ugrizy* spanning 320–1050 nm, identical in de-  
 486 sign to **LSSTCam**. However, its filter exchanger can  
 487 hold only three filters at a time, compared to five with  
 488 **LSSTCam**. The full-system throughput of the six **LSST-**  
 489 **ComCam** filters, which encompasses contributions from  
 490 a standard atmosphere at airmass 1.2, telescope optics,  
 491 camera surfaces, and the mean ITL detector quantum  
 492 efficiency is shown in **Figure 3**. The corresponding trans-  
 493 mission curves are provided as a **DP1** data product, see  
 494 §3.6.1

#### 495 2.2.2. Timing Calibration

496 The absolute time accuracy of data taken with **LSST-**  
 497 **ComCam** relies on the **Network Time Protocol (NTP)**  
 498 for clock synchronization, which should be accurate  
 499 to approximately 1 millisecond. In order to evaluate  
 500 the absolute timing accuracy of the entire system we  
 501 observed the geosynchronous satellite EUTELSAT 117  
 502 West B with a set of 10 usable 10-second exposures over  
 503 two nights. EUTELSAT 117 West B is part the **Global**  
 504 **Positioning System (GPS)** system and serves as one of  
 505

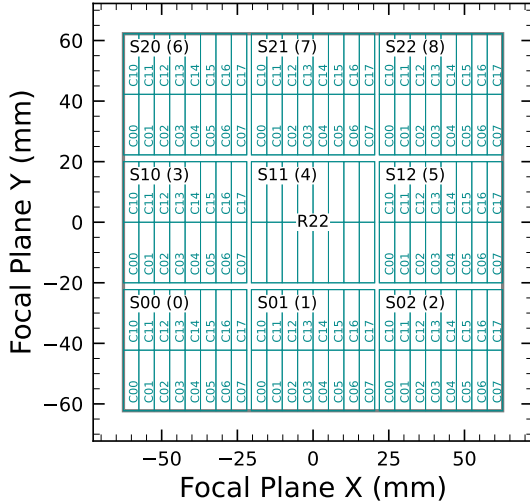


**Figure 2.** LSSTComCam focal plane layout, showing Raft 22 (R22) and the placement and numbering scheme of sensors (S) and amplifiers (C). The view is from above, looking through the LSSTComCam lenses onto the focal plane. Each sensor contains 16 amplifiers, and the raft is composed of a  $3 \times 3$  array of sensors. The detector number for each sensor is indicated in parentheses.

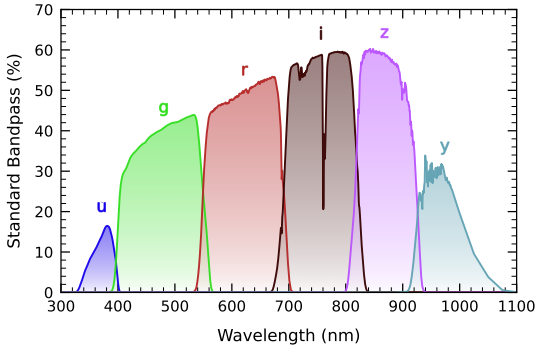


**Figure 3.** LSSTComCam standard bandpasses, illustrating full system throughput. The bandpasses include a standard atmosphere at airmass 1.2, telescope optics, camera surfaces, and mean ITL detector quantum efficiency. The corresponding transmission curves are provided as a DP1 data product.

the Wide Area Augmentation System (WAAS) satellites operated for the U.S. Federal Aviation Administration (FAA) and used to broadcast GPS corrections to air traffic.

As these satellites are part of the GPS system, their positions are tracked very precisely and the record of their locations is published after the fact and can be downloaded. Following the technique previously employed by other surveys, (J. L. Tonry et al. 2018), we observed the satellite while tracking the sky and then downloaded the data-files with its precise locations from

the National Satellite Test Bed web site<sup>84</sup>. By comparing the measured and predicted locations of the start of the satellite track on the sky, we determined that (relative to the start of integration-time recorded in the Flexible Image Transport System (FITS) headers) our time was accurate to  $53.6 \pm 11.0$  milliseconds.

This work continues to be an area of ongoing study, with the exact timing of when the shutter open command is issued, and the complete profile of the shutter movement not yet determined. However the open command is on average near 29 milliseconds later. Incorporating the delays into the fit reduces the offset to  $24.8 \pm 11.0$  milliseconds.

The full shutter takes approximately 396 milliseconds to completely open. As the LSSTComCam sensors are centered in the aperture, the center of the focal plane should be exposed about half-way through the shutter open procedure, 198 milliseconds after the open command. There are uncertainties on the full motion profile, and the blade direction motions are currently not known, but the fraction of the shutter aperture subtended by the focal plane is 52%. This implies that that the shutter will pass any pixel between  $198 \pm 103$  milliseconds. Subtracting this from the fitted delay of 24.8 milliseconds and adding the fitted error of 11.0 milliseconds in quadrature, results in a current conservative estimate of the delay of  $-173.2 \pm 104.1$  milliseconds, consistent with and smaller than the constraints on the timing offset determined using astrometric residuals from known asteroid associations presented in §5.9.2.

### 2.3. Flat Field System

During the on-sky campaign, key components of the Rubin calibration system (P. Ingraham et al. 2022), including the flat field screen, had not yet been installed. As a result, flat fielding for DP1 relied entirely on twilight flats. While twilight flats pose challenges such as non-uniform illumination and star print-through, they were the only available option during LSSTComCam commissioning and for DP1 processing. To mitigate these limitations, dithered, tracked exposures were taken over a broad range of azimuth and rotator angles to construct combined flat calibration frames. Exposure times were dynamically adjusted to reach target signal levels of between 10,000 and 20,000 electrons. Future campaigns with LSSTCam will benefit from more stable and uniform flat fielding using the Rubin flat field system, described in P. Fagrelus & E. S. Rykoff (2025).

<sup>84</sup> <https://www.nstb.tc.faa.gov/nstbarchive.html>

#### 2.4. LSST Science Pipelines Commissioning

Commissioning of the LSST Science Pipelines, (Rubin Observatory Science Pipelines Developers 2025), began once the telescope was able to routinely deliver sub-arcsecond image quality. The goals included testing the internal astrometric and photometric calibration across a range of observing conditions, validating the difference image analysis and Prompt Processing (K.-T. Lim 2023) framework, and accumulating over 200 visits per band to evaluate deep coadded images with integrated exposure times roughly equivalent to those of the planned LSST Wide-Fast-Deep (WFD) 10-year depth. To support these goals, seven target fields were selected that span a range of stellar densities, overlap with external reference datasets, and collectively span the full breadth of the four primary LSST science themes. These seven fields form the basis of the DP1 dataset. Figure 4 shows the locations of these seven fields on the sky, overlaid on the LSST baseline survey footprint (R. L. Jones et al. 2021; P. Yoachim 2022; Rubin’s Survey Cadence Optimization Committee et al. 2022, 2023, 2025), along with sky coverage of both the LSSTCam and LSSTComCam focal planes. Each of the seven target fields was observed repeatedly in multiple bands over many nights. A typical observing epoch on a given target field consisted of 5-20 visits in each of the three loaded filters. Only images taken as 1x30 second exposures have been included in DP1. All images were acquired using the Rubin Feature-Based Scheduler (FBS), version 3.0 (E. Naghib et al. 2019; P. Yoachim et al. 2024). Table 1 lists the seven DP1 fields and their pointing centers, and provides a summary of the band coverage in each.

Figure 5 shows the temporal sampling of observations by filter and by night. The figure indicates the dates on which each field was observed in a given band but does not convey the total number of observations obtained per filter on any individual night. Gaps in coverage across some bands arise from the fact that LSST-ComCam can only accommodate three filters at a time (see §2.2). As the campaign progressed, the temporal sampling became denser across all fields, reflecting improved efficiency and increased time allocated for science observations. The Extended Chandra Deep Field-South Survey (ECDFS) field received the most consistent and densest temporal sampling. It is important to note that the time sampling in the DP1 dataset differs significantly from what will be seen in the final LSST data. All fields except for the low ecliptic latitude field, Rubin\_SV\_38\_7, used a small random dithering pattern. The random translational dithers of the telescope boresight were applied for each visit, with offsets of up to 0.2 degrees around the pointing center (Table 1). The

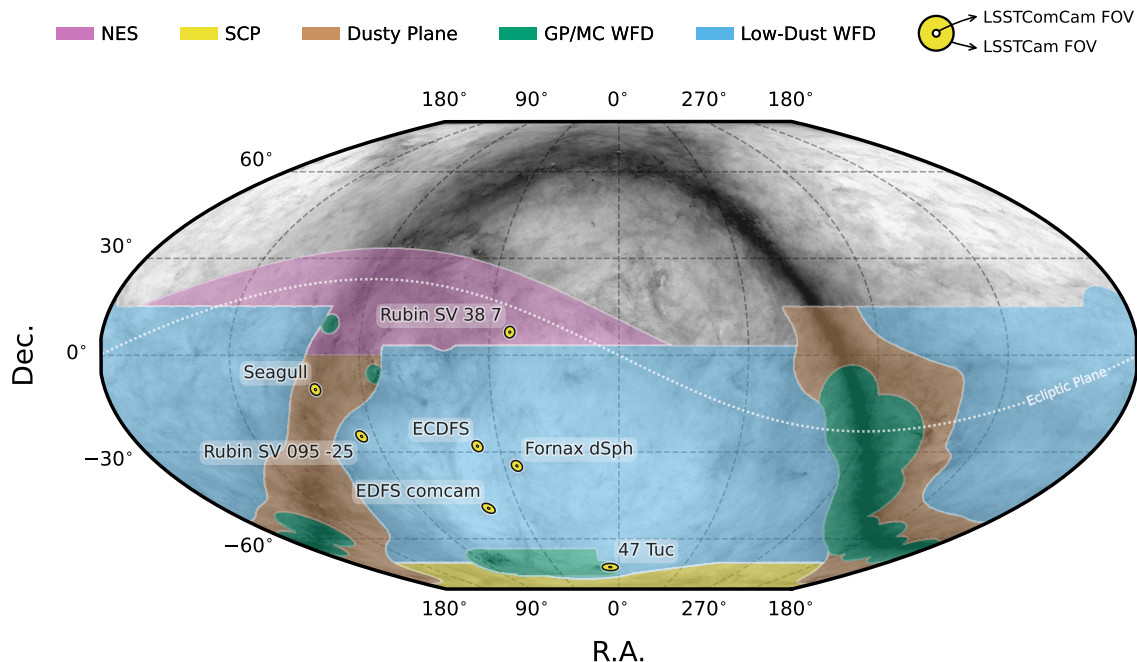
rotational dithers of the camera rotator were typically approximately 1 degree per visit, with larger random offsets at each filter change, which worked to keep operational efficiency high. The Rubin\_SV\_38\_7 field used a different dither pattern to optimize coverage of Solar System Objects and test Solar System Object linking across multiple nights. These observations used a 2x2 grid of LSSTComCam pointings to cover an area of about 1.3 degreex1.3 degrees. The visits cycled between the grid’s four pointing centers, each separated by 0.65 degrees, and used small random translational dithers to fill chip gaps with the goal of acquiring 3-4 visits per pointing center per band in each observing epoch. The ra/dec vale giving in table 1 for this field is approximately the center of the 4 files.

Figure 6 shows sky coverage maps showing the distribution of visits in each of the seven DP1 fields, color coded by band. The images clearly show the focal plane chip gaps and dithering pattern. DP1 Only the detectors for which single frame processing succeeded are included in the plots, which explains why the central region of 47\_Tuc looks thinner than the other fields (see §5.10). Table 2 reports the 5 $\sigma$  point source depths for coadded images per field and per band, where coverage in a band is non-zero, together with the expected 10-year LSST depths derived from the baseline simulated survey (F. B. Bianco et al. 2022).

#### 2.5. Delivered Image Quality

The delivered image quality is influenced by contributions from both the observing system (i.e., dome, telescope and camera) and the atmosphere. During the campaign, the Rubin Differential Image Motion Monitor (DIMM) was not operational, so atmospheric seeing was estimated using live data from the Southern Astrophysical Research Telescope (SOAR) Ring-Image Next Generation Scintillation Sensor (RINGSS) seeing monitor, also located on Cerro Pachón. Although accelerometers mounted on the mirror cell and top-end assembly were available to track dynamic optics effects, such as mirror oscillations that can degrade optical alignment, this data was not used during the campaign. Mount encoder data were used to measure the mount jitter in every image, with a measured median contribution of 0.004 arcseconds to image degradation. As the pointing model was not fine tuned, tracking errors could range from 0.2 to 0.4 arcseconds per image, depending on RA and Dec. Dome and mirror-induced seeing were not measured during the campaign.

The DP1 median delivered image quality, quantified as the PSF at FWHM across all filters and target fields, is 1".14. The best images achieve a PSF FWHM of ap-



**Figure 4.** Locations of the seven DP1 fields overlaid on the LSST baseline survey footprint. NES: North Ecliptic Spur, SCP: South Celestial Pole, Low-Dust WFD: regions away from the Galactic Plane (GP) observed with a WFD cadence, GP/MC WFD: Galactic Plane and Magellanic Clouds regions observed with a WFD cadence. The field of view covered by the LSSTCam and LSSTComCam focal planes is shown as concentric yellow circles about the pointing center of each field.

**Table 1.** DP1 fields and pointing centers with the number of exposures in each band per field. ICRS coordinates are in units of decimal degrees, and are specified as J2000.

Field Code	Field Name	RA	DEC	Band						Total
				deg	deg	<i>u</i>	<i>g</i>	<i>r</i>	<i>i</i>	
47_Tuc	47 Tucanae Globular Cluster	6.128	-72.090	6	10	32	19	0	5	72
ECDFS	Extended Chandra Deep Field South	53.160	-28.100	43	230	237	162	153	30	855
EDFS_comcam	Rubin SV Euclid Deep Field South	59.150	-48.730	20	61	87	42	42	20	272
Fornax_dSph	Fornax Dwarf Spheroidal Galaxy	40.080	-34.450	0	5	25	12	0	0	42
Rubin_SV_095_-25	Rubin SV Low Galactic Latitude Field	95.040	-25.000	33	82	84	23	60	10	292
Rubin_SV_38_7	Rubin SV Low Ecliptic Latitude Field	37.980	7.015	0	44	40	55	20	0	159
Seagull	Seagull Nebula	106.300	-10.510	10	37	43	0	10	0	100
Total				112	469	548	313	285	65	1792

671 proximately  $0''.58$ . Both the per-sensor PSF FWHM and  
 672 the overall median vary depending on the filter and the  
 673 specific target field. The median delivered image quality  
 674 per band and target field is provided in Table 3. Fig-  
 675 ure 7 shows the distribution of PSF FWHM (in arcsec)  
 676 over all 16071 individual sensors images. Ongoing efforts  
 678 aim to quantify all sources of image degradation, includ-  
 679 ing contributions from the camera system; static and  
 680 dynamic optical components; telescope mount motion;

681 observatory-induced seeing from the dome and primary  
 682 mirror; and atmospheric conditions. For the LSST, the  
 683 design specification for the median delivered image qual-  
 684 ity, referenced to the zenith and 550 nm, is  $0''.7$ . This  
 685 value corresponds to the measured median atmospheric  
 686 seeing at the Cerro Pachón site and a system contribu-  
 687 tion to delivered image quality of  $0''.35$  added in quadra-  
 688 ture.

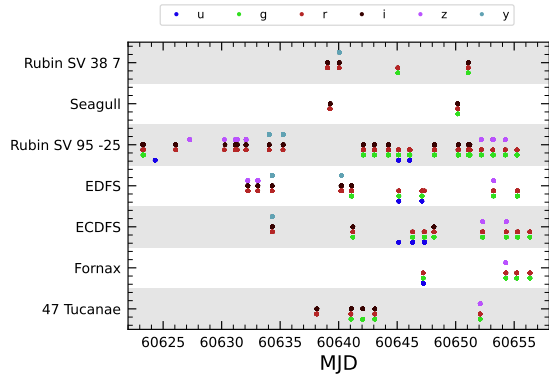


**Figure 5.** Temporal distribution of DP1 observations, grouped by field as a function of Modified Julian Date (MJD) and color-coded by filter. Each point indicates that a given field was observed at least once in the corresponding filter on that date.

**Table 2.** DP1 median  $5\sigma$  coadded point-source detection limits per field and band, compared with the expected 10-year LSST values derived from the baseline simulated survey (F. B. Bianco et al. 2022).

Field Code	Band					
	<i>u</i>	<i>g</i>	<i>r</i>	<i>i</i>	<i>z</i>	<i>y</i>
47_Tuc	-	24.03	24.24	23.90	-	21.79
ECDFS	24.55	26.18	25.96	25.71	25.07	23.10
EDFS_comcam	23.42	25.77	25.72	25.17	24.47	23.14
Fornax_dSph	-	24.53	25.07	24.64	-	-
Rubin_SV_095_-25	24.29	25.46	24.95	24.86	24.32	22.68
Rubin_SV_38_7	-	25.46	25.15	24.86	23.52	-
Seagull	23.51	24.72	24.19	-	23.30	-
LSST 10-year	25.73	26.86	26.88	26.34	25.63	24.87

The DP1 median delivered image quality across all bands is  $1''.14$ , as measured by the PSF FWHM.

### 3. OVERVIEW OF THE CONTENTS OF RUBIN DP1

In this section we describe the Rubin DP1 data products and provide summary statistics for each. For more detailed information, we refer the reader to the DOI-registered DP1 release documentation available at <https://dp1.lsst.io> and the catalog schemas available at <https://sdm-schemas.lsst.io>.<sup>85</sup>

<sup>85</sup> Searchable catalog schemas are also available to Data Rights Holders via the Rubin Science Platform at <https://data.lsst.cloud>.

**Table 3.** DP1 Median image quality per field and per band quantified as the PSF at FWHM in arcseconds.

Field Code	Band						All
	<i>u</i>	<i>g</i>	<i>r</i>	<i>i</i>	<i>z</i>	<i>y</i>	
47_Tuc	-	1.27	1.25	1.11	-	1.33	1.22
ECDFS	1.40	1.14	1.08	1.00	1.00	1.07	1.08
EDFS_comcam	1.88	1.25	1.20	1.10	1.18	0.99	1.19
Fornax_dSph	-	1.16	0.82	0.93	-	-	0.85
Rubin_SV_095_-25	1.40	1.25	1.14	0.97	1.17	0.82	1.19
Rubin_SV_38_7	-	1.13	1.13	1.10	1.22	-	1.13
Seagull	1.50	1.34	1.19	-	1.19	-	1.25
All	1.48	1.17	1.12	1.03	1.11	1.01	1.13

The DP1 science data products are derived from the 15972 individual CCD images taken across 1792 exposures in the seven LSSTComCam commissioning fields (§2.4). To aid legibility, we have separated the descriptions of the data products from the description of the data release processing pipeline (§4). Similarly, as the DP1 data products can be accessed via one or both of International Virtual Observatory Alliance (IVOA) Services (§6.2.1) or the Data Butler (§6.2.2), we describe them here in a manner that is agnostic to the means of access.

The data products that comprise DP1 provide an early preview of future LSST data releases and are strongly dependent on the type and quality of the data that was collected during the LSSTComCam on-sky campaign (§2.4). Consequently not all anticipated LSST data products, as described in the Data Product Definition Document (DPDD) (M. Jurić et al. 2023), were produced for the DP1 dataset.

Rubin Observatory has adopted the convention by which single-epoch detections are referred to as “Sources”, and the astrophysical object associated with a given detection is referred to as an “Object”<sup>86</sup>. As such, a given Object will likely have multiple associated Sources, since it will be observed in multiple epochs.

At the highest level, the DP1 data products fall into one of five types:

- **Science Images**, including single-epoch images, deep and template coadded images, and difference images (§3.1);

<sup>86</sup> We caution that this nomenclature is not universal; for example, some surveys use “detections” for what we call “sources”, and “sources” for what we call “objects”.

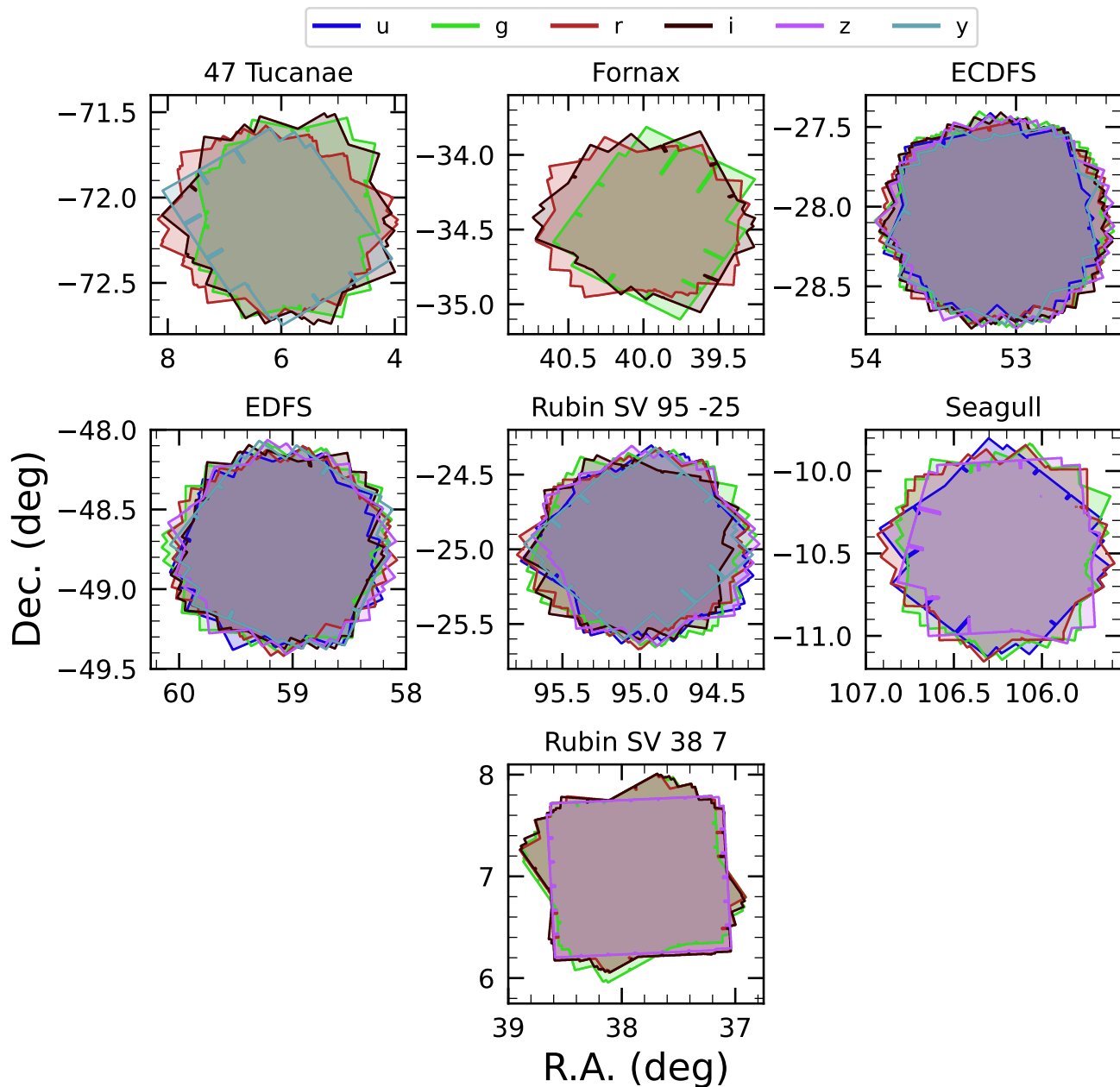


**Figure 6.** Sky coverage maps showing the distribution of visits in each field, color coded by band. The images clearly show the focal plane chip gaps and dithering pattern. Only the detectors for which single frame processing succeeded are included in the plots, which explains why the central region of 47\_Tuc looks thinner than the other fields.

- 729 • **Catalogs** of astrophysical Sources and Objects detected and measured in the aforementioned images. We also provide the astrometric and photometric reference catalog generated from external sources that was used during processing to generate the DP1 data products (§3.2);

730

731

732

733

734

737 for example, zoomable multi-band images and coverage maps (§3.4.1);

738

739 • **Ancillary data products**, including, for example, the parameters used to configure the data processing pipelines, log and processing performance files, and calibration data products (§3.6);

740

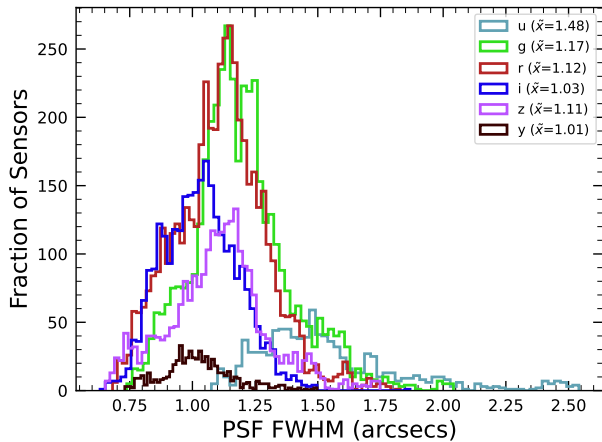
741

742
- 735 • **Maps**, which provide non-science-level visualizations of the data within the release. They include,

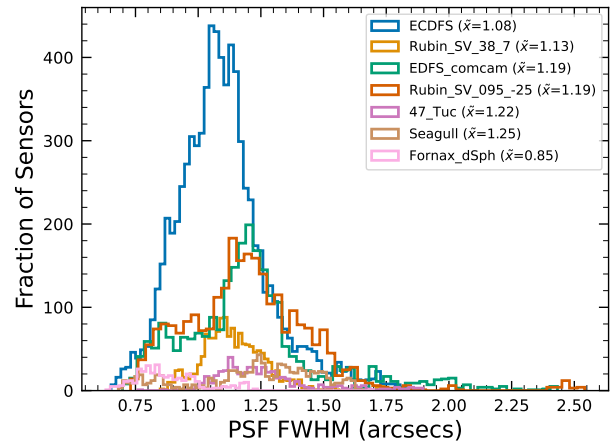
736

743

744 • **Metadata** in the form of tables containing information about each visit and processed image, such



(a) PSF FWHM (arcsecs) per passband across all DP1 target fields.



(b) PSF FWHM (arcsecs) per DP1 target field across all passbands

**Figure 7.** Histograms showing the distribution of delivered image quality for all 16071 single-epoch individual sensors in the DP1 dataset per passband (a) and per field (b). The median values are given in the legend.

745 as pointing, exposure time, and a range of image  
746 quality summary statistics (§3.5).

747 While images and catalogs are expected to be the pri-  
748 mary data products for scientific research, we also rec-  
749 ognize the value of providing access to other data types  
750 to support investigations and ensure transparency.

751 To facilitate processing, Rubin DP1 uses a single  
752 skymap<sup>87</sup> that covers the entire sky area encompass-  
753 ing the seven DP1 fields. The DP1 skymap divides the  
754 entire celestial sphere into 18938 tracts, each covering  
755 approximately 2.8 deg<sup>2</sup>. The tracts are arranged in rings  
756 of declination, ordered from south to north, then with  
757 increasing right ascension within a ring. Each tract is  
758 further subdivided into 10 × 10 equally-sized patches.  
759 Both tracts and patches overlap with their neighboring  
760 regions. The amount of overlap between tracts changes  
761 with declination, with tracts nearest the poles having  
762 the greatest degree of overlap; the minimum overlap be-  
763 tween tracts is 1′.0. By contrast, the amount of overlap  
764 between patches is constant, with each patch overlap-  
765 ping each of its neighbouring patches by 80′.0. Each  
766 patch covers 0.036 deg<sup>2</sup> which, due to the patch over-  
767 lap, is slightly larger than the tract area divided by the  
768 number of patches in a tract. The aerial coverage of  
769 a patch is comparable to, but somewhat smaller than,  
770 the 0.058 deg<sup>2</sup> field-of-view of a single LSSTComCam or  
771 LSSTCam detector, meaning each detector image spans

772 multiple patches. The size of a tract is larger than the  
773 LSSTComCam field of view. However, since each ob-  
774 served field extends across more than one tract, each  
775 field covers multiple tracts.

776 The skymap is integral to the production of co-added  
777 images. To create a coadded image, the processing  
778 pipeline selects all calibrated science images in a given  
779 field that meet specific quality thresholds (§3.1 and  
780 §4.5.1) for a given patch, warps them onto a single  
781 consistent pixel grid for that patch, as defined by the  
782 skymap, then coadds them. Each individual coadd im-  
783 age therefore covers a single patch.

784 Throughout this section, the data product names are  
785 indicated using monospace font. Data products are ac-  
786 cessed via either the IVOA Services (§6.2.1) or the Data  
787 Butler (§6.2.2).

### 788 3.1. Science Images

789 Science images are exposures of the night sky, as dis-  
790 tinct from calibration images (§3.6.3). Although the re-  
791 lease includes calibration images, thereby allowing users  
792 to reprocess the raw images if needed, this is expected  
793 to be necessary only in rare cases. Users are strongly  
794 encouraged to start from the visit\_image provided.  
795 The data product names shown here are those used by  
796 the Data Butler, but the names used in the IVOA Ser-  
797 vices differ only slightly in that they are prepended by  
798 “lsst.”.

#### 799 3.1.1. Raw Image

800 raw images (NSF-DOE Vera C. Rubin Observatory  
801 2025b) are unprocessed data received directly from the  
802 camera. Each raw corresponds to a single CCD from a  
803 single LSSTComCam exposure of 30 s duration. Each

<sup>87</sup> A skymap is a tiling of the celestial sphere, organizing large-scale sky coverage into manageable sections for processing and analysis. While the skymap described here is specific to DP1, we do not anticipate major changes to the skymap in future data releases.

**Table 4.** Number of raw images per field and band. Each raw image corresponds to a single 30-second LSSTComCam exposure on one CCD. Most exposures produce nine raw images, one per sensor in the focal plane, however some yield fewer due to occasional hardware or readout issues.

Field Code	Band						Total
	<i>u</i>	<i>g</i>	<i>r</i>	<i>i</i>	<i>z</i>	<i>y</i>	
47_Tuc	54	90	288	171	0	45	648
ECDFS	387	2070	2133	1455	1377	270	7692
EDFS_comcam	180	549	783	378	378	180	2448
Fornax_dSph	0	45	225	108	0	0	378
Rubin_SV_095_-25	297	738	756	207	540	90	2628
Rubin_SV_38_7	0	396	360	495	180	0	1431
Seagull	90	333	387	0	90	0	900
Total	1008	4221	4932	2814	2565	585	16125

LSSTComCam exposure typically produces up to nine raws, one per sensor in the focal plane. However, a small number of exposures resulted in fewer than nine raw images due to temporary hardware issues or readout faults.

In total, DP1 includes 16125 raw images. Table 4 provides a summary by target and band. A raw contains  $4608 \times 4096$  pixels, including prescan and overscan, and occupies around 18 MB of disk space.<sup>88</sup> The field of view of a single raw, excluding prescan and overscan regions, is roughly  $0^{\circ}23 \times 0^{\circ}22 \approx 0.051 \text{ deg}^2$ , corresponding to a plate scale of  $0''.2$  per pixel.

### 3.1.2. Visit Image

visit\_images (NSF-DOE Vera C. Rubin Observatory 2025c) are fully-calibrated processed images. They have undergone instrument signature removal (§4.2.1) and all the single frame processing steps described in §4.2 which are, in summary: PSF modeling, background subtraction, and astrometric and photometric calibration. As with raws, a visit\_image contains processed data from a single CCD resulting from a single 30 s LSSTComCam exposure. As a consequence, a single LSSTComCam exposure typically results in nine visit\_images. The handful of exposures with fewer than nine raw images also have fewer than nine visit\_images, but there are an additional 153 raw that failed processing and for which there is thus no corresponding visit\_image.

<sup>88</sup> Each amplifier image contains 3 and 64 columns of serial prescan and overscan pixels, respectively, and 48 rows of parallel overscan pixels, meaning a raw contains  $4072 \times 4000$  exposed pixels.

The majority of failures – 131 in total – were due to challenges with astrometric fits or PSF models in the 47\_Tuc crowded field. The other failures were in the Rubin\_SV\_095\_-25 (9 failures), ECDFS (8), Fornax\_dSph (3), and EDFS\_comcam (2) fields.

In total, there are 15972 visit\_images in DP1. Each visit\_image comprises three images: a calibrated science image, a variance image, and a pixel-level bit-mask that flags issues such as saturation, cosmic rays, or other artifacts. Each visit\_image also contains a position-dependent PSF model, World Coordinate System (WCS) information, and various metadata providing information about the observation and processing. The science and variance images and the pixel mask each contain  $4072 \times 4000$  pixels. In total, a single visit\_image, including all extensions and metadata, occupies around 110 MB of disk space. A plot showing the normalized cumulative histogram of the  $5\sigma$  depths of all the visit\_images in DP1 is shown in Figure 8.

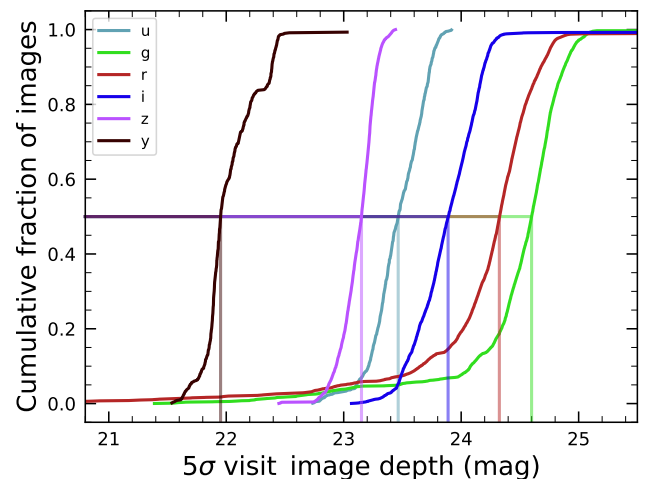


**Figure 8.** Normalized cumulative histograms of the  $5\sigma$  depths of all visit\_images in each band. The vertical lines indicate the 50th percentiles for each band (see legend).

### 3.1.3. Deep Coadd

deep\_coadds are created on a per-band basis, meaning only data from exposures taken with a common filter are coadded. As such, there are up to six deep\_coadds covering each patch – one for each of the six LSSTComCam bands. The process of producing deep\_coadds is described in §4.5 but, to summarize, it involves the selection of suitable visit\_images (both in terms of patch coverage, band, and image quality), the warping of those visit\_images onto a common pixel grid, and the co-adding of the warped visit\_images. To be included in a DP1 deep\_coadd, a visit\_image needed to have a

863 PSF FWHM smaller than  $1''.7$ . Of the 15972 `visit_`  
 864 `images`, 15375 satisfied this criterion and were therefore  
 865 used to create `deep_coadds`.

866 There are a total of 2644 `deep_coadds` in DP1. As  
 867 mentioned above, a single `deep_coadd` covers one `patch`,  
 868 and includes a small amount of overlap with its neigh-  
 869 boring `patch`. The skymap used for DP1 defines a `patch`  
 870 as having an on-sky area of  $0.028 \text{ deg}^2$  excluding overlap,  
 871 and  $0.036 \text{ deg}^2$  including overlap. A single `deep_coadd`  
 872 – including overlap – contains  $3400 \times 3400$  equal-sized  
 873 pixels, corresponding to a platescale of  $0''.2$  per pixel.  
 874 Each `deep_coadd` contains the science image (i.e., the  
 875 coadd), a variance image, and a pixel mask; all three  
 876 contain the same number of pixels. Each `deep_coadd`  
 877 also contains a position-dependent PSF model (which  
 878 is the weighted sum of the PSF models of the input  
 879 `visit_images`), WCS information, plus various `meta-`  
 880 `data`.

881 The number of `visit_images` that contributed to a  
 882 given `deep_coadd` varies across the patch; the Survey  
 883 Property Maps can be consulted to gain insights into  
 884 the total exposure time at all locations covered by the  
 885 survey. Similarly, since coadds always cover an entire  
 886 `patch`, it is common for a `deep_coadd` to contain regions  
 887 that were not covered by any of the selected `visit_`  
 888 `images`, particularly if the `patch` is on the outskirts of  
 889 a field and was thus not fully observed. By the nature  
 890 of how coadds are produced, such regions may contain  
 891 seemingly valid `flux` values (i.e., not necessarily zeros or  
 892 NaNs), but will instead be flagged with the `NO_DATA` flag  
 893 in the pixel mask. It is therefore crucial that the pixel  
 894 mask be referred to when analyzing `deep_coadds`.

#### 3.1.4. Template Coadd

895 `template_coadds` (NSF-DOE Vera C. Rubin Obser-  
 896 vatory 2025d) are those created to use as templates for  
 897 difference imaging, i.e., the process of subtracting a tem-  
 898 plate image from a `visit_image` to identify either vari-  
 899 able or `transient` objects. It should be noted, however,  
 900 that `template_coadds` are not themselves subtracted  
 901 from `visit_images` but are, instead, warped to match  
 902 the WCS of a `visit_image`. It is this warped template  
 903 that is subtracted from the `visit_image` to create a  
 904 difference image.<sup>89</sup> As with `deep_coadds`, `template_`  
 905 `coadds` are produced by warping and co-adding multiple  
 906 `visit_images` covering a given skymap-defined `patch`.  
 907 The process of building `template_coadds` is the same  
 908 as that for `deep_coadds`, but the selection criteria differ  
 909

<sup>89</sup> For storage space reasons, warped templates are not retained for DP1, as they can be readily and reliably recreated from the `template_coadds`.

910 between the two types of coadd. In the case of `tem-`  
 911 `plate_coadds`, one third of `visit_images` covering the  
 912 `patch` in question with the narrowest PSF FWHM are  
 913 selected. If one third corresponds to fewer than twelve  
 914 `visit_images` (i.e., there are fewer than 36 `visit_im-`  
 915 `ages` covering the `patch`), then the twelve `visit_images`  
 916 with the narrowest PSF FWHM are selected. Finally, if  
 917 there are fewer than twelve `visit_images` covering the  
 918 `patch`, then all `visit_images` are selected. Of the 15972  
 919 `visit_images`, 13113 were used to create `template_`  
 920 `coadds`. This selection strategy is designed to opti-  
 921 mize for seeing when a `patch` is well-covered by `visit_`  
 922 `images`, yet still enable the production of `template_`  
 923 `coadds` for poorly-covered patches. As with `deep_`  
 924 `coadds`, the number of `visit_images` that contributed  
 925 to a `template_coadd` varies across the patch.

926 DP1 contains a total of 2730 `template_coadds`.<sup>90</sup> As  
 927 with `deep_coadds`, a single `template_coadd` covers a  
 928 single `patch`. Since the same skymap is used when cre-  
 929 ating both `deep_coadd` and `template_coadds`, the on-  
 930 sky area and pixel count of `template_coadds` are the  
 931 same as that of a `deep_coadd` (see above). Similarly,  
 932 `template_coadds` contain the science image (i.e., the  
 933 coadd), a variance image, and a pixel mask; all three  
 934 contain the same number of pixels. Also included are  
 935 the PSF model, WCS information, and `metadata`. As  
 936 is the case for `deep_coadd`, those pixels within `tem-`  
 937 `plate_coadds` that are not covered by any of the se-  
 938 lected `visit_images` may still have seemingly valid val-  
 939 ues, but are indicated with the `NO_DATA` flag within the  
 940 pixel mask.

#### 3.1.5. Difference Image

941 `difference_images` (NSF-DOE Vera C. Rubin Obser-  
 942 vatory 2025e) are generated by the subtraction of  
 943 the warped, scaled, and PSF-matched `template_coadd`  
 944 from the `visit_image` (see §4.6.1). In principle, only  
 945 those sources whose `flux` has changed relative to the  
 946 `template_coadd` should be apparent (at a significant  
 947 level) within a `difference_image`. In practice, how-  
 948 ever, there are numerous spurious sources present in  
 949 `difference_images` due to unavoidably imperfect tem-  
 950 plate matching.

951 In total, there are 15972 `difference_images` in DP1,  
 952 one for each `visit_image`.

953 Like `visit_images`, `difference_images` contain the  
 954 science (i.e., difference) image, a variance image, and a  
 955 pixel mask; all three contain the same number of pixels,  
 956

<sup>90</sup> The difference in the number of `deep_coadds` and `template_coadds` is due to the difference in the `visit_image` selection criteria for each coadd.

957 which is the same as that of the input `visit_image`. 1004  
 958 Also included is the PSF model, WCS information, and 1005  
 959 `metadata`. 1006

### 960 3.1.6. Background Images 1007

961 Background images contain the model `background` 1008  
 962 that has been generated and removed from a science 1009  
 963 image. `visit_images`, `deep_coadds` and `template_` 1010  
 964 `coadds` all have associated `background` images.<sup>91</sup> Back- 1011  
 965 ground images contain the same number of pixels as 1012  
 966 their respective science image, and there is one `back-` 1013  
 967 `ground` image for each `visit_image`, `deep_coadd`, and 1014  
 968 `template_coadd`. Difference imaging analysis also mea- 1015  
 969 sures and subtracts a `background` model, but the `dif-` 1016  
 970 `ference_background` data product is not written out 1017  
 971 by default and is not part of DP1. 1018

972 Background images are not available via the IVOA 1020  
 973 Service; they can only be accessed via the Butler Data 1021  
 974 Service. 1022

### 975 3.2. Catalogs 1023

976 In this section we describe science-ready tables pro- 1025  
 977 duced by the science pipelines. All catalogs contain data 1026  
 978 for detections in the images described in §3.1, except 1027  
 979 the `Calibration` catalog, which contains reference data 1028  
 980 obtained from previous surveys. Observatory-produced 1029  
 981 `metadata` tables are described in §3.5. 1030

982 The catalogs contains measurements for either Sources 1031  
 983 detected in `visit_images` and `difference_images`, or 1032  
 984 Objects detected in `deep_coadds`. All catalogs store 1033  
 985 fluxes rather than magnitudes, with fluxes measured in 1034  
 986 nanojansky ( $1 \text{ nJy} = 10^{35} \text{ Wm}^2\text{Hz}^{-1}$ ). Fluxes are pre- 1035  
 987 ferred for multi-epoch observations, as they can be av- 1036  
 988 eraged across epochs, unlike magnitudes. Additionally, 1037  
 989 flux measurements on difference images (§3.1) are com- 1038  
 990 puted against a template, representing a flux difference. 1039  
 991 As a result, flux measurements on difference images can 1040  
 992 be negative, particularly for faint sources in the presence 1041  
 993 of noise. 1042

994 The `Source`, `Object`, `ForcedSource`, `DiaSource`, 1043  
 995 `DiaObject`, and `ForcedSourceOnDiaObject` catalogs 1044  
 996 described below each vary in terms of their specific 1045  
 997 columns but generally contain: one or more unique 1046  
 998 identification numbers, positional information, multiple 1047  
 999 types of `flux` measurements (e.g., aperture fluxes, PSF 1048  
 1000 fluxes, Gaussian fluxes, etc.), and a series of boolean 1049  
 1001 flags indicating characteristics such as saturation or cos- 1050  
 1002 mic ray contamination for each source/object. The Solar 1051  
 1003 System catalogs `SSObject` and `SSSource` deviate from 1052

91 In future data releases, `background` images may be included as part of their respective science image data product.

1003 this general structure in that they instead contain or- 1004  
 1005 bital parameters for all known asteroids. 1006

1007 Where applicable, quantities are prefixed with the 1008  
 1009 band in which they were measured, and all measured 1010  
 1011 properties are reported with their associated  $1\sigma$  uncer- 1012  
 1013 tainties. For example, `g_ra` and `g_raErr` refer to right 1014  
 1015 ascension and its uncertainty, measured in the g-band. 1016

1017 Fluxes for various apertures are provided together 1018  
 1019 with an uncertainty and a flag, and named in the for- 1020  
 1021 mat `[band]_ap[size]Flux`, where `[size]` is the aper- 1022  
 1023 ture diameter in pixels. For example, `g_ap03Flux`, `g_` 1024  
 1025 `ap03FluxErr`, `g_ap03Flux_flag` provide the flux, un- 1026  
 1027 certainty and flag measured within a 3.0-pixel aperture 1027  
 1028 in the g-band. Similarly for flux measurements using 1028  
 1029 difference algorithms, e.g. `g_psfFlux` provides the flux 1029  
 1030 derived using the PSF model as a weight function, forced 1030  
 1031 on g-band. 1031

1032 A complete list of columns with description and 1033  
 1034 units for all tables in DP1 is available at [https://sdm-](https://sdm-schemas.lsst.io/dp1.html) 1034  
 1035 [schemas.lsst.io/dp1.html](https://sdm-schemas.lsst.io/dp1.html) Since DP1 is a preview release, 1035  
 1036 it does not include all the catalogs expected in a full 1036  
 1037 LSST Data Release. Additionally, some catalogs may 1037  
 1038 be missing columns, as not all quantities have been com- 1038  
 1039 puted yet. These quantities will be included in future 1039  
 1040 releases, and, where it is known to be the case, missing 1040  
 1041 data are noted in the catalog descriptions that follow. 1041

1042 Catalog data are stored in the Qserv database (§6.5.1) 1042  
 1043 and are accessible via Table Access Protocol (IVOA 1043  
 1044 standard) (IVOA), and an online DP1 catalog schema 1044  
 1045 is available at <https://sdm-schemas.lsst.io/dp1.html>. 1045  
 1046 Catalog data are also accessible via the Data Butler (see 1046  
 1047 §6.2.2). 1047

#### 1048 3.2.1. Source Catalog 1049

1050 The `Source` catalog (NSF-DOE Vera C. Rubin Ob- 1050  
 1051 servatory 2025f) contains data on all sources which are, 1051  
 1052 prior to deblending (§4.5.2), detected with a greater 1052  
 1053 than  $5\sigma$  significance in each individual visit. The de- 1053  
 1054 tectations reported in the `Source` catalog have undergone 1054  
 1055 deblending; in the case of blended detections, only the 1055  
 1056 deblended sources are included in the `Source` catalog. It 1056  
 1057 is important to note that while the criterion for inclusion 1057  
 1058 in a `Source` catalog is a  $> 5\sigma$  detection in a `visit_` 1058  
 1059 `image` prior to deblending, the positions and fluxes are 1059  
 1060 reported post-deblending. Hence, it is possible for the 1060  
 1061 `Source` catalog to contain sources whose `flux-to-error` 1061  
 1062 ratios – potentially of all types (i.e., aperture `flux`, PSF 1062  
 1063 `flux`, etc.) – are less than 5. 1063

1064 In addition to the general information mentioned 1064  
 1065 above (i.e., IDs, positions, fluxes, flags), the `Source` cat- 1065  
 1066 alog also includes basic `shape` and extendedness informa- 1066  
 1067 tion. 1067

1055 The **Source** catalog contains data for 46 million  
1056 **sources** in DP1.

1057 A cumulative histogram showing the PSF magnitudes  
1058 of all **sources** contained within the **Source** catalogue is  
1059 presented in the top panel of Figure 9

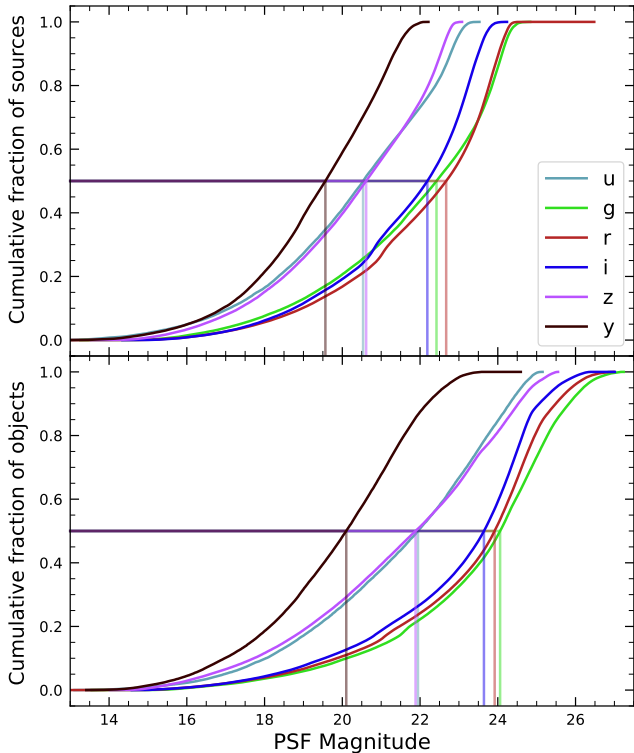


**Figure 9.** Normalized cumulative histograms of the PSF magnitudes of all  $> 5\sigma$ -detected **sources** (top panel) and **objects** (bottom panel) contained in the **Source** and **Object** catalogs, respectively, separated according to band (see legend). The vertical lines indicate the 50th percentile for each band.

### 3.2.2. Object Catalog

1060  
1061 The **Object** catalog (NSF-DOE Vera C. Rubin Ob-  
1062 servatory 2025g) contains data on all objects detected  
1063 with a greater than  $5\sigma$  significance in the **deep\_coadds**.  
1064 With coadd images produced on a per-band basis, a  
1065  $> 5\sigma$  detection in one or more of the bands will re-  
1066 sult in an object being included in the **Object** catalog.  
1067 For cases where an object is detected at  $> 5\sigma$  in more  
1068 than one band, a cross-matching has been performed  
1069 between bands to associate an object in one band with  
1070 its counterpart(s) in the other bands. As such, unlike  
1071 the **Source** catalog, the **Object** catalog contains data  
1072 from multiple bands. The objects reported in the **Ob-**  
1073 **ject** catalog have also undergone deblending; in the case  
1074 of blended detections, only the deblended child objects

1075 are included in the catalog. As with the **Source** cat-  
1076 alog, the criterion for inclusion in the **Object** catalog  
1077 is a  $> 5\sigma$  detection in one of the **deep\_coadds** prior to  
1078 deblending, yet the positions and fluxes of objects are re-  
1079 ported post-deblending. Hence, it is possible for **Object**  
1080 catalog to contain **objects** whose **flux**-to-error ratios —  
1081 potentially of all types and in all bands — are less than  
1082 5.

1083 In addition to the general information mentioned  
1084 above (i.e., IDs, positions, fluxes, flags), the **Object** cat-  
1085 alog also includes basic **shape** and extendedness informa-  
1086 tion. While they may be included in future data releases,  
1087 no photometric redshifts, Petrosian magnitudes (V. **Pet-**  
1088 **rosian 1976**), proper motions or periodicity information  
1089 are included in the DP1 object catalogs.

1090 The **Object** catalog contains data for 2.3 million ob-  
1091 jects in DP1.

### 3.2.3. ForcedSource Catalog

1092  
1093 The **ForcedSource** catalog (NSF-DOE Vera C. Ru-  
1094 bin Observatory 2025h) contains forced PSF photome-  
1095 try measurements performed on both **difference\_im-**  
1096 **ages** (i.e., the **psfDiffFlux** column) and **visit\_images**  
1097 (i.e., the **psfFlux** column) at the positions of all the  
1098 objects in the **Object** catalog, to allow assessment of  
1099 the time variability of the fluxes. We recommend using  
1100 the **psfDiffFlux** column when generating light curves  
1101 because this quantity is less sensitive to **flux** from nei-  
1102 ghboring sources than **psfFlux**. In addition to **forced pho-**  
1103 **tometry PSF** fluxes, a number of boolean flags are also  
1104 included in the **ForcedSource** catalog.

1105 The **ForcedSource** catalog contains a total of 269 mil-  
1106 lion entries across 2.3 million unique objects.

### 3.2.4. DiaSource Catalog

1107  
1108 The **DiaSource** catalogs (NSF-DOE Vera C. Rubin  
1109 Observatory 2025i) contains data on all the sources de-  
1110 tected at  $> 5\sigma$  significance — including those associ-  
1111 ated with known Solar System objects — in the **dif-**  
1112 **ference\_images**. Unlike sources detected in **visit\_im-**  
1113 **ages**, sources detected in difference images (hereafter,  
1114 “**DiaSource**”) have gone through an association step in  
1115 which an attempt has been made to associate them into  
1116 underlying objects called “**DiaObject**”. The **DiaSource**  
1117 catalog consolidates all this information across multiple  
1118 visits and bands. The detections reported in the **Dia-**  
1119 **Source** catalog have not undergone deblending.

1120 The **DiaSource** catalog contains data for 3.1 million  
1121 **DiaSources** in DP1.

### 3.2.5. DiaObject Catalog

1122  
1123 The **DiaObject** catalog (NSF-DOE Vera C. Rubin  
1124 Observatory 2025j) contains the astrophysical objects

that `DiaSources` are associated with (i.e., the `DiaObjects`). The `DiaObject` catalog contains only non-Solar System Objects; Solar System Objects are, instead, recorded in the `SSObject` catalog. When a `DiaSource` is identified, the `DiaObject` and `SSObject` catalogs are searched for objects to associate it with. If no association is found, a new `DiaObject` is created and the `DiaSource` is associated to it. Along similar lines, an attempt has been made to associate `DiaObjects` across multiple bands, meaning the `DiaObject` catalog, like the `Object` catalog, contains data from multiple bands. Since `DiaObjects` are typically [transient](#) or variable (by the nature of their means of detection), the `DiaObject` catalog contains summary statistics of their fluxes, such as the mean and standard deviation over multiple epochs; users must refer to the `ForcedSourceOnDiaObject` catalog (see below) or the `DiaSource` catalog for single [epoch flux](#) measurements of `DiaObjects`.

The `DIAObject` catalog contains data for 1.1 million `DiaObjects` in [DP1](#).

### 3.2.6. *ForcedSourceOnDiaObject Catalog*

The `ForcedSourceOnDiaObject` catalog ([NSF-DOE Vera C. Rubin Observatory 2025k](#)) is equivalent to the `ForcedSource` catalog, but contains [forced photometry](#) measurements obtained at the positions of all the `DiaObjects` in the `DiaObject` catalog.

The `ForcedSourceOnDiaObject` catalog contains a total of 197 million entries across 1.1 million unique `DiaObjects`.

## 3.3. *SSObject Catalog*

The `SSObject` catalog ([NSF-DOE Vera C. Rubin Observatory 2025l](#)), [Minor Planet Center Orbit database \(MPCORB\)](#) and `SSObject`, carry information about solar system objects. The [MPCORB](#) table provides the [Minor Planet Center](#)-computed orbital elements for all known asteroids, including those that Rubin discovered. For [DP1](#), the `SSObject` catalog serves primarily to provide the mapping between the [International Astronomical Union \(IAU\)](#) designation of an object (listed in [MPCORB](#)), and the internal `ssObjectId` identifier, which is used as a key to find solar system object observations in the `DiaSource` and `SSSource` tables. The `SSObject` catalog contains data for 431 `SSObjects` in [DP1](#).

### 3.3.1. *SSSource Catalog*

The `SSSource` catalog ([NSF-DOE Vera C. Rubin Observatory 2025m](#)) contains data on all `DiaSources` that are either associated with previously-known Solar System Objects, or have been confirmed as newly-discovered Solar System Objects by confirmation of their

orbital properties. As entries in the `SSSource` catalog stem from the `DiaSource` catalog, they have all been detected at  $> 5\sigma$  significance in at least one band. The `SSSource` catalog contains data for 5988 Solar System Sources.

### 3.3.2. *CcdVisit Catalog*

The `CcdVisit` catalog ([NSF-DOE Vera C. Rubin Observatory 2025n](#)) contains data for each individual processed `visit_image`. In addition to technical information, such as the on-sky coordinates of the central pixel and measured pixel scale, the `CcdVisit` catalog contains a range of data quality measurements, such as whole-image summary statistics for the [PSF](#) size, zeropoint, sky [background](#), sky noise, and quality of astrometric solution. It provides an efficient method to access `visit_image` properties without needing to access the image data. When combined with the data contained in the `Visit` table described in [§3.5](#), it provides a full picture of the telescope pointing and sky conditions at the time of observation.

The `CcdVisit` catalog contains entries summarizing data for all 16071 `visit_images`.

### 3.3.3. *Calibration Catalog*

The `Calibration` catalog is the reference catalog that was used to perform astrometric and photometric [calibration](#). It is a whole-sky catalog built specifically for [LSST](#), as no single prior reference catalog had both the depth and coverage needed to calibrate [LSST](#) data. It combines data from multiple previous reference catalogs and contains only stellar sources. Full details on how the `Calibration` catalog was built are provided in [P. S. Ferguson et al. \(2025\)](#)<sup>92</sup>. We provide a brief summary here.

For the *grizy* bands, the input catalogs were (in order of decreasing priority): [Dark Energy Survey \(DES\) Y6 Calibration Stars \(E. S. Rykoff et al. 2023\)](#); [Gaia-B or R Photometry \(Gaia\) \(XP\) Synthetic Magnitudes \(Gaia Collaboration et al. 2023a\)](#); the [Panoramic Survey Telescope and Rapid Response System \(Pan-STARRS\)1 3PI Survey \(K. C. Chambers et al. 2016\)](#); [Data Release 2 of the SkyMapper survey \(C. A. Onken et al. 2019\)](#); and [Data Release 4 of the VLT Survey Telescope \(VST\) Asteroid Terrestrial-impact Last Alert System \(ATLAS\) survey \(T. Shanks et al. 2015\)](#). For the *u*-band, the input catalogs were (in order of decreasing priority): [Standard Stars from Sloan Digital Sky Survey \(SDSS\) Data Release 16 \(R. Ahumada et al. 2020\)](#); [Gaia-XP Synthetic](#)

<sup>92</sup> In [P. S. Ferguson et al. \(2025\)](#), the calibration reference catalog is referred to as “The Monster”. This terminology is also carried over to the [DP1 Butler](#).

Magnitudes (Gaia Collaboration et al. 2023a); and synthetic magnitudes generated using *Single Lens Reflex (SLR)*, which estimates the  $u$ -band flux from the  $g$ -band flux and  $g-r$  colors. This SLR estimates were used to boost the number of  $u$ -band reference sources, as otherwise the source density from the  $u$ -band input catalogs is too low to be useful for the LSST.

Only stellar sources were selected from each input catalog. Throughout, the *Calibration* catalog uses the DES bandpasses for the *grizy* bands and the SDSS bandpass for the  $u$ -band; color transformations derived from high quality sources were used to convert fluxes from the various input catalogs (some of which did not use the DES/SDSS bandpasses) to the respective bandpasses. All sources from the input catalogs are matched to *Gaia-Data Release 3 (DR3)* sources for robust astrometric information, selecting only isolated sources (i.e., no neighbors within  $1''$ ).

After collating the input catalogs and transforming the fluxes to the standard DES/SDSS bandpasses, the catalog was used to identify sources within a specific region of the sky. This process generated a set of standard columns containing positional and flux information, along with their associated uncertainties.

### 3.3.4. Source and Object Designations

To refer to individual sources or objects from the DP1 catalogs, one should follow the LSST DP1 naming convention that has been registered with the International Astronomical Union. Because the *Source*, *Object*, *DiaSource*, *DiaObject*, and *SSObject* tables each have their own unique IDs, their designations should differ. In general, source designations should begin with the string “LSST-DP1” (denoting the Legacy Survey of Space and Time, Data Preview 1), followed by a string specifying the table from which the source was obtained. These strings should be “O” (for the *Object* table), “S” (*Source*), “DO” (*DiaObject*), “DS” (*DiaSource*), or “SSO” (*SSObject*). Following the table identifier, the designation should contain the full unique numeric identifier from the specified table (i.e., the *objectId*, *sourceId*, *diaObjectId*, *diaSourceId*, or *ssObjectId*). Each component of the identifier should be separated by dashes, resulting in a designation such as “LSST-DP1-TAB-123456789012345678”. In summary, source designations should adhere to the formats listed below:

- Object: LSST-DP1-O-609788942606161356 (for *objectId* 609788942606161356)
- Source: LSST-DP1-S-600408134082103129 (for *sourceId* 600408134082103129)

- *DiaObject*: LSST-DP1-DO-609788942606140532 (for *diaObjectId* 609788942606140532)
- *DiaSource*: LSST-DP1-DS-600359758253260853 (for *diaSourceId* 600359758253260853)
- *SSObject*: LSST-DP1-SSO-21163611375481943 (for *ssObjectId* 21163611375481943)

Tables that were not explicitly mentioned in the description above do not have their own unique IDs, but are instead linked to one of the five tables listed above via a unique ID. For example, the *ForcedSource* table is keyed on *objectId*, *ForcedSourceOnDiaObject* uses *diaObjectId*, *SSSource* is linked to *diaSourceId* and *ssObjectId*, and *MPCORB* uses *ssObjectId*.

### 3.4. Maps

Maps are two-dimensional visualizations of survey data. In DP1, these fall into two categories: Survey Property Maps and Hierarchical Progressive Survey (HiPS) Maps (P. Fernique et al. 2015).

#### 3.4.1. Survey Property Maps

Survey Property Maps (NSF-DOE Vera C. Rubin Observatory 2025o) summarize how properties such as observing conditions or exposure time vary across the observed sky. Each map provides the spatial distribution of a specific quantity at a defined sky position for each band by aggregating information from the images used to make the *deep\_coadd*. Maps are initially created per *tract* and then combined to produce a final consolidated map. At each sky location, represented by a spatial pixel in the Hierarchical Equal-Area iso-Latitude Pixelisation (HEALPix)(K. M. Górski et al. 2005) grid, values are derived using statistical operations, such as minimum, maximum, mean, weighted mean, or sum, depending on the property.

DP1 contains 14 survey property maps. The available maps describe total exposure times, observation epochs (one each for the earliest, mean, and latest observation epoch), PSF size and *shape* (one for each of the  $e^1$  and  $e^2$  shape parameters; see §5.2), PSF magnitude limits, sky background and noise levels, as well as astrometric shifts (one each for right ascension and declination) and PSF distortions (one for each of the  $e^1$  and  $e^2$  shape parameters) due to wavelength-dependent atmospheric Differential Chromatic Refraction (DCR) effects. They all use the dataset type format *deep\_coadd\_<PROPERTY>\_consolidated\_map\_<STATISTIC>*. For example, *deep\_coadd\_exposure\_time\_consolidated\_map\_sum* provides a spatial map of the total exposure time accumulated per sky position in

units of seconds. All maps are stored in `HealSparse`<sup>93</sup> format. Survey property maps are only available via the `Data Butler` (§6.2.2).

Figure 10 presents three survey property maps for exposure time, PSF magnitude limit, and sky noise, computed for representative tracts and bands. Because full consolidated maps cover widely separated tracts, we use clipped per-tract views here to make the spatial patterns more discernible.

### 3.4.2. HiPS Maps

HiPS Maps (P. Fernique et al. 2015), offer an interactive way to explore seamless, multi-band tiles of the sky regions covered by DP1, allowing for smooth panning and zooming. DP1 provides multi-band HiPS images created by combining data from individual bands of `deep_coadd` and `template_coadd` images, using an improved version (Lust et al. in prep) of the algorithm presented in R. Lupton et al. (2004). These images are false-color representations generated using various filter combinations for the red, green, and blue channels.

The available filter combinations include `gri`, `izy`, `riz`, and `ugr` for both `deep_coadd` and `template_coadd`. Additionally, for `deep_coadd` only, we provide color blends such as `uug` and `grz`. Post-DP1, we plan to also provide single-band HiPS images for all `ugrizy` bands in both `Portable Network Graphics` (PNG) and `FITS` formats.

HiPS maps are only accessible through the HiPS viewer in the `Rubin Science Platform` (RSP) Portal (§6.3) and cannot be accessed via the `Data Butler` (§6.2.2). All multi-band HiPS images are provided in PNG format.

### 3.5. Metadata

DP1 also includes `metadata` about the observations, which are stored in the `Visit` table. We distinguish it from a catalog as the data it contains was produced by the observatory directly, rather than the science pipelines. The `Visit` table contains technical data for each visit, such as telescope pointing, camera rotation, `airmass`, exposure start and end time, and total exposure time. Some of the information contained within the `Visit` table is also contained in the `CCDVisit` catalogue described in §3.2 (e.g., exposure time), although the latter also includes information produced by the processing pipelines at a per-detector level, such as the PSF size and limiting magnitudes of a given `visit_image`.

<sup>93</sup> A sparse `HEALPix` representation that efficiently encodes data values on the celestial sphere. <https://healsparse.readthedocs.io>

## 3.6. Ancillary Data Products

DP1 also includes several ancillary data products. While we do not expect most users to need these, we describe them here for completeness. All the Data Products described in this section can only be accessed via the `Data Butler` (§6.2.2).

### 3.6.1. Standard Bandpasses

Figure 3 shows the full-system throughput of the six `LSSTComCam` filters. The corresponding transmission curves are provided as a DP1 data product. These datasets tabulate the full-system transmission of the six `LSSTComCam` filters as a function of wavelength and were used as a reference for the `LSSTComCam` DP1 photometry. The `standard_passband` dataset is keyed by band and is stored in `Astropy Table` format.

### 3.6.2. Task configuration, log, and metadata

DP1 includes `provenance`-related data products such as task logs, `configuration` files, and task metadata. Configuration files record the parameters used in each processing task, while logs and `metadata` contain information output during processing. These products help users understand the processing setup and investigate potential processing failures.

### 3.6.3. Calibration Data Products

Calibration data products include a variety of images and models that are used to characterize and correct the performance of the camera and other system components. These include bias, dark, and flat-field images, `Photon Transfer Curve` (PTC) gains, brighter-fatter kernels (P. Antilogus et al. 2014), charge transfer inefficiency (CTI) models, linearizers, and illumination corrections. For flat-field corrections, DP1 processing used combined flats, which are averaged from multiple individual flat-field exposures to provide a stable `calibration`. These `calibration` products are essential inputs to `Instrument Signal Removal` (ISR) (§4.2.1). While these products are included in DP1 for transparency and completeness, users should not need to rerun ISR for their science and are advised to start with the processed `visit_image`.

## 4. DATA RELEASE PROCESSING

`Data Release Processing` (DRP) is the systematic processing of all Rubin Observatory data collected up to a certain date to produce the calibrated images, catalogs of detections, and derived data products described in Section 3. DP1 was processed entirely at the `United`

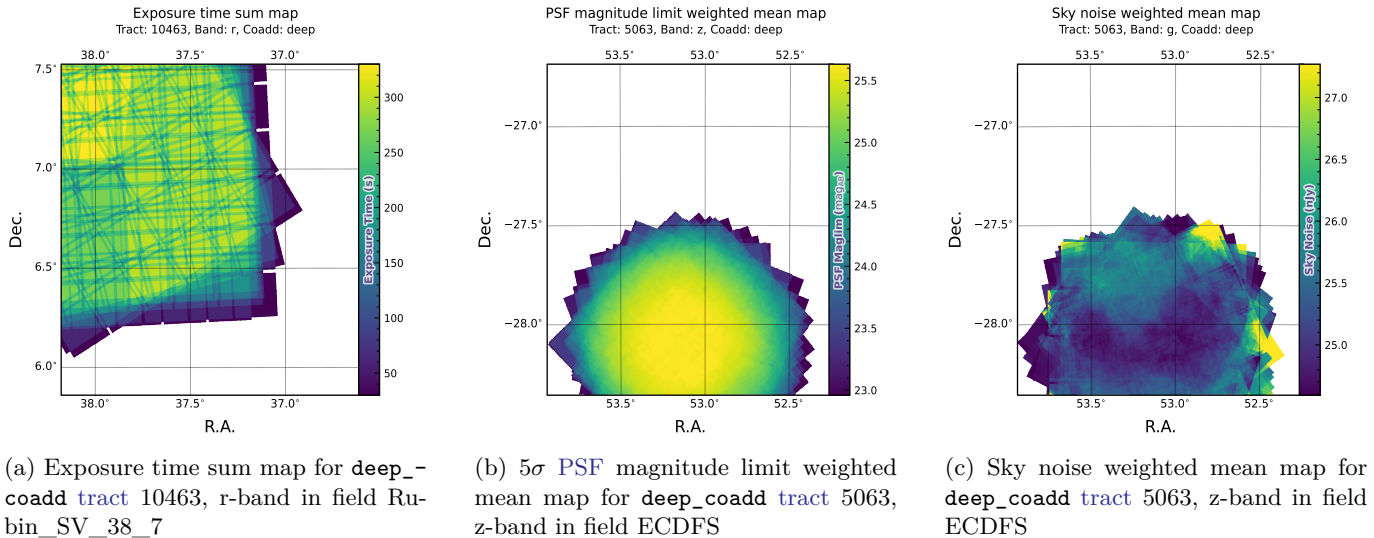


**Figure 10.** Examples of survey property maps from Rubin DP1 across different bands, clipped to the boundary of a single tract for visual clarity.

1412 States Data Facility (USDF) at SLAC using 17,024 CPU 1437  
 1413 hours.<sup>94</sup> 1438

1414 This section describes the pipeline algorithms used to 1439  
 1415 produce DP1 and how they differ from those planned for 1440  
 1416 full-scale LSST data releases. Data Release Production 1441  
 1417 consists of four major stages: (1) single-frame processing, 1442  
 1418 (2) calibration, (3) coaddition, and (4) difference 1443  
 1419 image analysis (DIA). 1444

#### 1420 4.1. LSST Science Pipelines Software

1421 The LSST Science Pipelines software (Rubin Observa- 1447  
 1422 tory Science Pipelines Developers 2025; J. D. Swinbank 1448  
 1423 et al. 2020) will be used to generate all Rubin Observa- 1449  
 1424 tory and LSST data products. It provides both the algo- 1450  
 1425 rithms and middleware frameworks necessary to process 1451  
 1426 raw data into science-ready products, enabling analysis 1452  
 1427 by the Rubin scientific community. Version v29.1 of the 1453  
 1428 pipelines was used to produce DP1<sup>95</sup>. 1454

#### 1429 4.2. Single Frame Processing

##### 1430 4.2.1. Instrument Signature Removal

1431 The first step in processing LSSTComCam images is 1458  
 1432 to correct for the effects introduced by the telescope and 1459  
 1433 detector. Each sensor and its readout amplifiers can 1460  
 1434 vary slightly in performance, causing images of even a 1461  
 1435 uniformly illuminated focal plane to exhibit discontinu- 1462  
 1436 ities and shifts due to detector effects. The ISR pipeline 1463  
 1464

1437 aims to recover the original astrophysical signal as best 1438  
 1439 as possible and produce science-ready single-epoch im- 1440  
 1441 ages for source detection and measurement. A detailed 1442  
 1443 description of the ISR procedures can be found in P. 1444  
 1445 Fagrelius & E. S. Rykoff (2025); A. A. Plazas Malagón 1445  
 1446 et al. (2025). Figure 11 illustrates the model of detector 1446  
 1447 components and readout electronics and their impact 1447  
 1448 on the signal, tracing the process from photons incident 1448  
 1449 on the detector surface to the final quantized values<sup>96</sup> 1449  
 1450 recorded in the image files. The ISR pipeline essentially 1450  
 1451 “works backward” through the signal chain, correct- 1451  
 1452 ing the integer analog-to-digital units (ADU) raw 1452  
 1453 camera output back to a floating-point number of pho- 1453  
 1454 toelectrons created in the silicon. The physical detector, 1454  
 1455 shown on the left in Figure 11, is the source of effects 1455  
 1456 that arise from the silicon itself, such as the dark current 1456  
 1457 and the brighter-fatter effect (A. A. Plazas et al. 2018; 1457  
 1458 A. Broughton et al. 2024). After the integration time 1458  
 1459 has elapsed, the charge is shifted to the serial register 1459  
 1460 and read out, which can introduce charge transfer ineffi- 1460  
 1461 ciencies and a clock-injected offset level. The signals 1461  
 1462 for all amplifiers are transferred via cables to the Read- 1462  
 1463 out Electronics Board (REB), during which crosstalk 1463  
 1464 between the amplifiers may occur. The Analog Signal 1464  
 1465 Processing Integrated Circuit (ASPIC) on the REB con- 1465  
 1466 verts the analog signal from the detector into a digital 1466  
 1467 signal, adding both quantization and a bias level to the 1467  
 1468 image. Although the signal chain is designed to be stable 1468  
 1469 and linear, the presence of numerous sources of non- 1469  
 1470 linearity indicates otherwise. 1470

<sup>94</sup> For future Data Releases, data processing will be distributed across the USDF, the French (FrDF) and UK (UKDF) data facilities.

<sup>95</sup> Documentation for this version is available at: [https://pipelines.lsst.io/v/v29\\_1\\_1](https://pipelines.lsst.io/v/v29_1_1)

<sup>96</sup> The images written to disk by the camera have values that are integers that come from the ADC converting an analog voltage.

The *ISR* processing pipeline for *DP1* performs, in the following order: **Analogue-to-Digital Unit (ADU)** dithering to reduce quantization effects, serial overscan subtraction, saturation masking, gain normalization, crosstalk correction, parallel overscan subtraction, linearity correction, serial **CTI** correction, image assembly, bias subtraction, dark subtraction, brighter-fatter correction, defect masking and interpolation, variance plane construction, flat fielding, and amplifier offset (amp-offset) correction<sup>97</sup>. Flat fielding for *DP1* was performed using combined flats produced from twilight flats acquired with sufficient rotational dithering to mitigate artifacts from print-through stars, as described in §2.3.

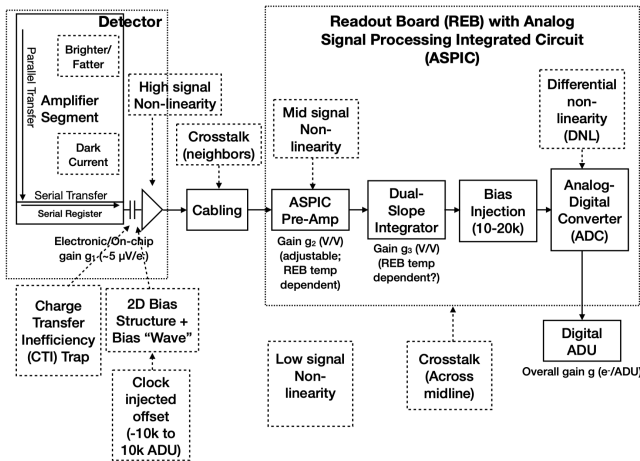


**Figure 11.** The model of the detector and REB components, labeled with the effects that they impart on signal.

#### 4.2.2. Background Subtraction

The background subtraction algorithms in the LSST Science Pipelines estimate and remove large-scale background signals from science imaging. Such signals may include sky brightness from airglow, moonlight, scattered light instrumental effects, zodiacal light, and diffuse astrophysical emission. In so doing, true astrophysical sources are isolated to allow for accurate detection and measurement.

To generate a **background** model, each post-*ISR* image is divided into superpixels of  $128 \times 128$  pixels. Pixels with a mask flag set that indicates that they contain no useful science data or that they contain **flux** from a preliminary source detection are masked. The iterative

<sup>97</sup> Amp-offset corrections are designed to address systematic discontinuities in background sky levels across amplifier boundaries. The implementation in the LSST Science Pipelines is based on the **Pan-STARRS** Pattern Continuity algorithm (C. Z. Waters et al. 2020).

$3\sigma$  clipped mean of the remaining pixels is calculated for each superpixel, constructing a **background** statistics image. A sixth-order Chebyshev polynomial is fit to these values on the scale of a single detector to allow for an extrapolation back to the native pixel resolution of the post-*ISR* image.

#### 4.3. Calibration

Stars are detected in each post-*ISR* image using a  $5\sigma$  threshold. Detections of the same star across multiple images are then associated to identify a consistent set of isolated stars with repeated observations suitable for use in PSF modeling, photometric **calibration**, and astrometric **calibration**.

Initial astrometric and photometric solutions are derived using only the calibration reference catalogs (see §3.2), and an initial PSF model is fit using PSFEx (E. Bertin 2011). These preliminary solutions provide approximate source positions, fluxes, and PSF shapes that serve as essential inputs to the **calibration** process, enabling reliable source matching, selection of high-quality stars, and iterative refinement of the final astrometric, photometric, and PSF models. These preliminary solutions are subsequently replaced by more accurate fits, as described in the following sections.

##### 4.3.1. PSF Modeling

PSF modeling in *DP1* uses the Piff (M. Jarvis et al. 2021) package. Our configuration of Piff utilizes its **PixelGrid** model with a fourth-order polynomial interpolation per **CCD**, except in the *u*-band, where star counts are insufficient to support a fourth-order fit. In this case, a second-order polynomial is used instead. Details on the choice of polynomial order, overall PSF modeling performance, and known issues are discussed in §5.2.

##### 4.3.2. Astrometric Calibration

Starting from the astrometric solution calculated in single frame processing (§4.2), the final astrometric solution is computed using the ensemble of visits in a given band that overlap a given **tract**. This allows the astrometric solution to be further refined by using all of the isolated point sources of sufficient signal-to-noise ratio in an image, rather than only those that appear in the reference catalog, as is done in single frame processing. Using multiple whole visits rather than a single detector also allows us to account for effects that impact the full focal plane, and for the proper motion and parallax of the sources.

In order to perform the fit of the astrometric solution, isolated point sources are associated between overlapping visits and with the **Gaia DR3** (Gaia Collaboration et al. 2023b) reference catalog where possible. The

1544 model used for DP1 consists of a static map from pixel  
 1545 space to an intermediate frame (the per-detector model),  
 1546 followed by a per-visit map from the intermediate frame  
 1547 to the plane tangent to the telescope boresight (the per-  
 1548 visit model), then finally a deterministic mapping from  
 1549 the tangent plane to the sky. The fit is done using the  
 1550 `gbdes` package (G. M. Bernstein et al. 2017), and a full  
 1551 description is given in C. Saunders (2024).

1552 The per-detector model is intended to capture quasi-  
 1553 static characteristics of the telescope and camera. Dur-  
 1554 ing Rubín Operations, the astrometric solution will al-  
 1555 low for separate epochs with different per-detector mod-  
 1556 els, to account for changes in the camera due to warm-  
 1557 ing and cooling and other discrete events. However, for  
 1558 DP1, LSSTComCam was assumed to be stable enough  
 1559 that all visits use the same per-detector model. The  
 1560 model itself is a separate two-dimensional polynomial for  
 1561 each detector. For DP1, a degree 4 polynomial was used;  
 1562 the degree of the polynomial mapping is tuned for each  
 1563 instrument and may be different for LSSTCam. Fur-  
 1564 ther improvements may be made by including a pixel-  
 1565 based astrometric offset mapping, which would be fit  
 1566 from the ensemble of astrometric residuals, but this is  
 1567 not included in the DP1 processing.

1568 The per-visit model attempts to account for the path  
 1569 of a photon from both atmospheric sources and those  
 1570 dependent on the telescope orientation. This model is  
 1571 also a polynomial mapping, in this case a degree 6 two-  
 1572 dimensional polynomial. Correction for DCR (§5.4) was  
 1573 not done for DP1, but will be included in LSSTCam pro-  
 1574 cessing during Rubín Operations. Future processing will  
 1575 also likely include a Gaussian Process fit to better ac-  
 1576 count for atmospheric turbulence, as was demonstrated  
 1577 by W. F. Fortino et al. (2021) and P. F. Léget et al.  
 1578 (2021).

1579 The final component of the astrometric calibration  
 1580 involves the positions of the isolated point sources in-  
 1581 cluded in the fit, which are described by five parameters:  
 1582 sky coordinates, proper motion, and parallax. While  
 1583 proper motions and parallaxes are not released for DP1,  
 1584 they are fitted for these sources in the astrometric solu-  
 1585 tion to improve the astrometric calibration.

#### 1586 4.3.3. Photometric Calibration

1587 Photometric calibration of the DP1 dataset is based  
 1588 on the Forward Global Calibration Method (FGCM)  
 1589 (FGCM D. L. Burke et al. 2018), adapted for the LSST  
 1590 Science Pipelines (H. Aihara et al. 2022; P. Fagrelus &  
 1591 E. S. Rykoff 2025). We used the FGCM to calibrate  
 1592 the full DP1 dataset with a forward model that uses a  
 1593 parameterized model of the atmosphere as a function of  
 1594 airmass along with a model of the instrument through-

1595 put as a function of wavelength. The FGCM process  
 1596 typically begins with measurements of the instrumental  
 1597 throughput, including the mirrors, filters, and detectors.  
 1598 However, because full scans of the LSSTComCam as-  
 1599 built filters and individual detectors were not available,  
 1600 we instead used the nominal reference throughputs for  
 1601 the Simonyi Survey Telescope and LSSTCam.<sup>98</sup> These  
 1602 nominal throughputs were sufficient for the DP1 cali-  
 1603 bration, given the small and homogeneous focal plane  
 1604 consisting of only nine ITL detectors. The FGCM atmo-  
 1605 sphere model, provided by MODTRAN (A. Berk et al.  
 1606 1999), was used to generate a look-up table for atmo-  
 1607 spheric throughput as a function of zenith distance at  
 1608 Cerro Pachón. This model accounts for absorption and  
 1609 scattering by molecular constituents of the atmosphere,  
 1610 including  $O_2$  and  $O_3$ ; absorption by water vapor; and  
 1611 Mie scattering by airborne aerosol particulates. Nightly  
 1612 variations in the atmosphere are modeled by minimiz-  
 1613 ing the variance in repeated observations of stars with  
 1614 a Signal to Noise Ratio (SNR) greater than 10, mea-  
 1615 sured using “compensated aperture fluxes”. These fluxes  
 1616 include a local background subtraction (see §4.2.2) to  
 1617 mitigate the impact of background offsets. The model  
 1618 fitting process incorporates all six bands (*ugrizy*) but  
 1619 does not include any gray (achromatic) terms, except  
 1620 for a linear assumption of mirror reflectance degrada-  
 1621 tion, which is minimal over the short duration of the  
 1622 DP1 observation campaign. As an additional constraint  
 1623 on the fit, we use a subset of stars from the reference  
 1624 catalog (P. S. Ferguson et al. 2025), primarily to con-  
 1625 strain the system’s overall throughput and establish the  
 1626 “absolute” calibration.

1627 Photometric transformation relations between LSST-  
 1628 Cam and LSSTComCam systems and other photomet-  
 1629 ric systems are under development and are provided in  
 1630 (M. N. Porter et al. 2025)

#### 1631 4.4. Visit Images and Source Catalogs

1632 With the final PSF models, WCS solutions, and pho-  
 1633 tometric calibrations in place, we reprocess each single-  
 1634 epoch image to produce a final set of calibrated visit  
 1635 images and source catalogs. Source detection is per-  
 1636 formed down to a  $5\sigma$  threshold using the updated PSF  
 1637 models, followed by measurement of PSF and aperture  
 1638 fluxes. These catalogs represent the best single-epoch  
 1639 source characterization, but they are not intended for  
 1640 constructing light curves. For time-domain analysis,  
 1641 we recommend using the forced photometry tables de-  
 1642 scribed in §4.6.2.

<sup>98</sup> Available at: <https://github.com/lstt/throughputs/tree/1.9>

## 4.5. Coaddition Processing

### 4.5.1. Coaddition

Only exposures with a *seeing* better than 1.7 arcseconds FWHM are included in the deep coadded images. For the template coadds, typically only the top third of visits with the best *seeing* are used (although see §3.1 for more details), resulting in an even tighter image quality cutoff for the template coadds. Exposures with poor PSF model quality, identified using internal diagnostics, are excluded to prevent contamination of the coadds with unreliable PSF estimates. The remaining exposures are combined using an inverse-variance weighted mean stacking algorithm.

To mitigate transient artifacts before coaddition, we apply the artifact rejection procedure described in Y. Al-Sayyad (2018) that identifies and masks features such as satellite trails, optical ghosts, and cosmic rays. It operates on a time series of PSF-matched images resampled onto a common pixel grid (“warps”) and leverages their temporal behavior to distinguish persistent astrophysical sources from transient artifacts.

Artifact rejection uses both direct (where no PSF-matching is performed) and PSF-matched warps, homogenized to a standard PSF of 1.8 arcseconds FWHM, broadly consistent with the 1.7 arcsecond FWHM *seeing* threshold used in data screening. A sigma-clipped mean of the PSF-matched warps serves as a static sky model, against which individual warps are differenced to identify significant positive and negative residuals. Candidate artifact regions are classified as *transient* if they appear in less than a small percentage of the total number of exposures, with the threshold based on the number of visits,  $N$ , as follows:

- $N = 1$  or  $2$ : threshold = 0 (no clipping).
- $N = 3$  or  $4$ : threshold = 1.
- $N = 5$ : threshold = 2.
- $N > 5$ : threshold =  $2 + 0.03N$ .

Identified *transient* regions are masked before coaddition, improving image quality and reducing contamination in derived catalogs.

### 4.5.2. Detection, Deblending and Measurement

After constructing coadded images, sources are detected in each band, merged across bands, deblended, and measured to generate the final object catalogs (§3.2). For each coadd in all six bands, we perform source detection at a  $5\sigma$  detection threshold and then adjust the background with a per-patch constant (coadds are built from background-subtracted images,

but the deeper detection on coadds redefines what is considered source versus background). Detections across bands are merged in a fixed priority order, *irzygu*, to form a union detection catalog, which serves as input to deblending.

Deblending is performed using the Scarlet Lite algorithm, which implements the same model as Scarlet (P. Melchior et al. 2018), but operates on a single pixel grid. This allows the use of analytic gradients, resulting in greater computational speed and memory efficiency.

*Object* measurement is then performed on the deblended detection footprints in each band. Measurements are conducted in three modes: independent per-band measurements, forced measurements in each band, and multiband measurements.

Most measurement algorithms operate through a single-band plugin system, largely as originally described in J. Bosch et al. (2018). The same plugins are run separately for each object on a deblended image, which uses the Scarlet model as a template to re-weight the original noisy coadded pixel values. This effectively preserves the original image in regions where objects are not blended, while dampening the noise elsewhere.

A reference band is chosen for each object based on detection significance and measurement quality using the same priority order as detection merging (*irzygu*) and a second round of measurements is performed in forced mode using the shape and position from the reference band to ensure consistent colors (J. Bosch et al. 2018).

Measurement algorithm outputs include object fluxes, centroids, and higher-order moments thereof like sizes and shapes. A variety of *flux* measurements are provided, from aperture fluxes and forward modeling algorithms.

Composite model (CModel) magnitudes (K. Abazajian et al. 2004; J. Bosch et al. 2018) are used to calculate the extendedness parameter, which functions as a star-galaxy classifier. Extendedness is a binary classifier that is set to 1 if the PSF model flux is less than 98.5% of the (free, not forced) CModel flux in a given band. Additionally, the extendedness in the reference band is provided as a separate column for convenience as a multiband star-galaxy classification, and is recommended generally but also specifically for objects with low signal-to-noise ratio in some bands.

Gaussian-Aperture-and-PSF (Gaussian Aperture and PSF (GAaP) K. Kuijken 2008; A. Kannawadi 2025) fluxes are provided to ensure consistent galaxy colors across bands. Sérsic model (J. L. Sérsic 1963; J. L. Sérsic 1968) fits are run on all available bands simultaneously (MultiProFit, D. S. Taranu 2025). The resulting Sérsic model fluxes are provided as an alternative to CModel

and are intended to represent total galaxy fluxes. Like CModel, the Sérsic model is a Gaussian mixture approximation to a true Sérsic profile, convolved with a Gaussian mixture approximation to the PSF. Sérsic model fits also include a free centroid, with all other structural parameters shared across all bands. That is, the intrinsic model has no color gradients, but the convolved model may have color gradients if the PSF parameters vary significantly between bands.

CModel measurements use a double “shapelet” (A. Refregier 2003) PSF model with a single shared shape. The Sérsic fits are intended to use a double Gaussian with independent shape parameters for each component. Due to a pipeline misconfiguration, the Sérsic fits actually used the shapelet PSF parameters, with the higher-order terms ignored (since MultiProFit does not support shapelet PSFs). This bug is not expected to impact the galaxy fluxes significantly, since the higher-order shapelet PSF parameters tend to be small, and the fix will be applied in future campaigns. Either way, the double Gaussian PSF parameters are included for each object.

Further details on the performance of these algorithms are found in §5.7.

#### 4.6. Variability Measurement

##### 4.6.1. Difference Imaging Analysis

Difference Image Analysis (DIA) uses the decorrelated Alard & Lupton image differencing algorithm (D. J. Reiss & R. H. Lupton 2016). We detected both positive and negative DIASources at  $5\sigma$  in the difference image. Sources with footprints containing both positive and negative peaks due to offsets from the template position or blending were fit with a dipole centroid code, which simultaneously fits offset positive and negative PSFs. We filter the resulting DIASource catalog to remove detections with pixel flags indicative of artifacts, non-astrophysical trail lengths, or unphysically negative direct fluxes. Finally, we perform a simple spatial association of DIASources into DIAObjects using a one-arcsecond matching radius.

The Machine Learning reliability model applied to DP1 was developed with the aim to meet the latency requirements for Rubin Alert Production when executed on CPUs. Accordingly we developed a relatively simple model: a Convolutional Neural Network with three convolutional layers, and two fully connected layers. The convolutional layers have a  $5 \times 5$  kernel size, with 16, 32, and 64 filters, respectively. A max-pooling layer of size 2 is applied at the end of each convolutional layer, followed by a dropout layer of 0.4 to reduce overfitting. The last fully connected layers have sizes of 32 and 1. The ReLU

activation function is used for the convolutional layers and the first fully connected layer, while a sigmoid function is used for the output layer to provide a probabilistic interpretation. The cutouts are generated by extracting postage stamps of  $51 \times 51$  pixels centered on the detected sources. The input data of the model consist of the template, science, and difference image stacked to have an array of shape (3, 51, 51). The model is implemented using PyTorch (J. Ansel et al. 2024). The Binary Cross Entropy loss function was used, along with the Adaptive Moment Estimation (Adam) optimizer with a fixed learning rate of  $1 \times 10^{-4}$ , weight decay of  $3.6 \times 10^{-2}$ , and a batch size of 128. The final model uses the weights that achieved the best precision/purity for the test set. Training was done on the SLAC Shared Scientific Data Facility (S3DF) with an NVIDIA model L40S GPU.

The model was initially trained using simulated data from the second DESC Data Challenge (DC2; (LSST Dark Energy Science Collaboration (LSST DESC) et al. 2021)) plus randomly located injections of PSFs to increase the number of real sources, for a total of 89,066 real sources. The same number of bogus sources were selected at random from non-injected DIASources. Once the LSSTComCam data were available, the model was fine-tuned on a subset of the data containing 183,046 sources with PSF injections. On the LSSTComCam test set, the model achieved an accuracy of 98.06%, purity of 97.87%, and completeness of 98.27%. As discussed in §5.8, the injections used to train this model version do not capture all types of astrophysical variability, so performance on the test set will not be representative for variable stars, comets, and other types of variable objects. The machine-learning reliability score, reported in the reliability column of the DIASource catalog, is a scalar value between 0 and 1 that quantifies the model’s confidence that a given detection is astrophysical.

##### 4.6.2. Light Curves

To produce light curves, we perform multi-epoch forced photometry on both the direct visit images and the difference images. For light curves we recommend the forced photometry on the difference images (psDiffFlux on the ForcedSource Table), as it isolates the variable component of the flux and avoids contamination from static sources. In contrast, forced photometry on direct images includes flux from nearby or blended static objects, and this contamination can vary with seeing. Centroids used in the multi-epoch forced photometry stage are taken either from object positions measured on the coadds or from the DIAObjects (the associated DIASources detected on difference images).

## 4.6.3. Solar System Processing

Solar system processing in DP1 consists of two key components: the association of observations (sources) with known solar system objects, and the discovery of previously unknown objects by linking sets of *tracklets*<sup>99</sup>.

The association component begins by generating expected positions for all objects in the Minor Planet Center orbit catalog, using ephemerides computed with the *Sorcha* survey simulation toolkit (Merritt et al., in press)<sup>100</sup>. To enable fast lookup of objects potentially present in an observed visit, we use the *mpsky* package (M. Juric 2025). In each image, the closest *DiaSource* within 1 arcsecond of a known solar system object’s predicted position is associated to that object. In DP1 we used a simple positional association to tag *DiaSources* that are likely observations of known asteroids. The 1 arcsecond radius is intentionally generous; we did not see evidence of mismatches at DP1 depth and volume. This radius will be tuned for future processing campaigns.

The discovery component of Solar System processing uses the *heliolinx* package<sup>101</sup>, which provides tools for asteroid identification and linking (A. Heinze et al. 2023). The repository contains code for the following tasks:

- Tracklet creation with `make_tracklets`
- Multi-night *tracklet* linking with an algorithm
- Linkage post processing (orbit fitting, outlier rejection, and de-duplication) with `link_purify`

The inputs to the discovery processing comprised all sources detected in difference images, regardless of whether they were tagged in the association step. These inputs were produced by an early processing of *LSST-ComCam* commissioning data, some of which were later rejected during DP1 processing and therefore do not appear in the final DP1 data products.

About 10% of all commissioning visits targeted the near-ecliptic field *Rubin\_SV\_38\_7*, chosen to facilitate asteroid discovery. *Rubin\_SV\_38\_7* produced the vast majority of asteroid discoveries in DP1, as expected, but a few were found in off-ecliptic fields as well.

Tracklet creation with `make_tracklets` used an upper limit angular velocity of 1.5 *deg/day*, faster than any main belt asteroid and in the range of many *Near-*

*Earth Object (NEO)* discoveries. While no formal minimum angular velocity was imposed, in practice it would be unlikely to detect objects moving slower than about 0.01 *deg day*<sup>-1</sup>. To minimize false *tracklets* from fields observed multiple times per night, the minimum *tracklet* length was set to three detections, and a minimum on-sky motion of five arcseconds was required for a valid *tracklet*. To claim a discovery candidate, we required *tracklets* to be linked across at least three nights.

Multi-night *tracklet* linking is the heart of Solar system discovery, which connects (“links”) *tracklets* belonging to the same object over a series of nights. It employs the *HelioLinC3D* algorithm (S. Eggl et al. 2020; A. Heinze et al. 2022), a refinement of the original *HelioLinC* algorithm of M. J. Holman et al. (2018). Each processing run tested each *tracklet* with 324 different hypotheses spanning heliocentric distances from 1.5 to 9.8 *astronomical unit (au)* and radial velocities spanning the full range of possible bound orbits (eccentricity 0.0 to nearly 1.0). The upper limit of 10 *au* was chosen because searches targeting more distant populations require different parameter choices. This range of distance encompasses all main belt asteroids and Jupiter Trojans, as well as many comets and Mars-crossers and some *NEOs*. A dedicated search for objects at heliocentric distances out to 50 *au* was also conducted; no distant objects were detected, consistent with expectations for the size of the DP1 data set. Smaller heliocentric distances were not attempted here because nearby objects move rapidly across the sky and hence were not likely to remain long enough in an *LSSTComCam* field to be discovered.

Candidate linkages, defined as groups of *tracklets* whose propagated orbits cluster within a radius of  $1.33 \times 10^3$  *au* at 1 *au*, are identified, then post-processed via `link_purify` to yield a final, non-overlapping set of high-confidence asteroid candidates, ranked by orbit-fit residuals and related metrics. While *heliolinx* can produce false-positive or redundant raw linkages by design, these are filtered during post-processing by `link_purify`, which applies a Rubin-specific, more stringent version of the MPC validation rules<sup>102</sup>. This step both rejects spurious linkages and deduplicates multiple hypotheses for the same object, ensuring that only the highest-quality, non-redundant linkages are carried forward for orbit determination and for distinguishing new discoveries from rediscoveries of known objects.

<sup>99</sup> A *tracklet* is defined as two or more detections of a moving object candidate taken in close succession in a single night.

<sup>100</sup> Available at <https://github.com/dirac-institute/sorcha>

<sup>101</sup> <https://github.com/heliolinx/heliolinx>

<sup>102</sup> <https://minorplanetcenter.net/mpcops/documentation/identifications/additional/>

## 5. PERFORMANCE CHARACTERIZATION AND KNOWN ISSUES

In this section, we provide an assessment of the DP1 data quality and known issues.

### 5.1. Sensor Anomalies and ISR

In addition to the known detector features identified before LSSTComCam commissioning, most of which are handled by the ISR processing (see §4.2.1), we discovered a number of new types of anomalies in the DP1 data. Since no corrections are currently available for these anomalies, they are masked and excluded from downstream data products.

#### 5.1.1. Vampire Pixels

“Vampire” pixels are visible on the images as a bright defect surrounded by a region of depressed flux, as though the defect is stealing charge from its neighboring pixels. Figure 12 shows an example of a vampire pixel near the center of R22\_S11 on an *r*-band flat.

From studies on evenly illuminated images, vampires appear to conserve charge. Unfortunately, no unique optimum way exists to redistribute this stolen flux so, following visual inspection, a defect mask was created to exclude them from processing. We have found some similar features on the ITL detectors on LSSTCam, and will use the same approach to exclude them.

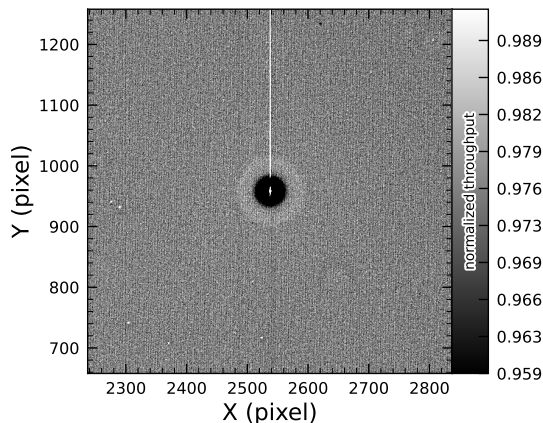


**Figure 12.** A large vampire pixel near the center of R22\_S11, as seen on the *r*-band flat. This clearly shows the central hot “vampire” pixels, surrounded by a region of depressed signal, with a brighter ring surrounding that caused by the local electric field effects. The charge contained in the central pixels is incompletely shifted as the image is read, and that charge leaks out into subsequent rows as they are shifted through the remnant charge. The columns that contain the hot pixels are masked as defects in all processing, as this feature cannot be otherwise corrected.

### 5.1.2. Phosphorescence

Some regions of the LSSTComCam CCD raft were seen to contain large numbers of bright defects. An example is shown in Figure 13 in a *g*-band flat. On further investigation, it appears that on some detectors a layer of photoresist wax was incompletely removed from the detector surface during production. As this wax is now trapped below the surface coatings, there is no way to physically clean these surfaces. If this wax responded to all wavelengths equally, then it would likely result in quantum efficiency dips, which might be removable during flat correction. However, it appears that this wax is slightly phosphorescent, with a decay time on the order of minutes, resulting in the brightness of these defects being dependent on the illumination of prior exposures. The worst of these regions were excluded with manual masks.

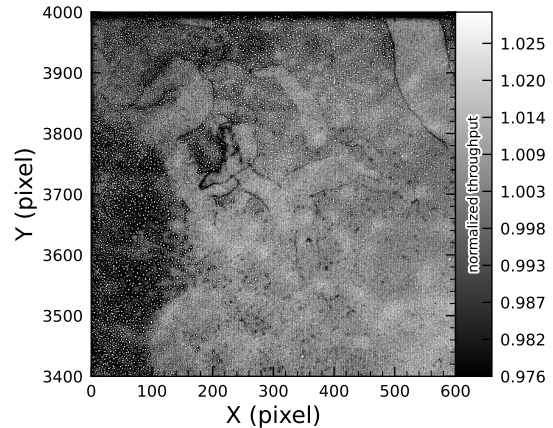


**Figure 13.** The top left corner of R22\_S01 in the *g*-band flat, showing the many small defect features that are caused by the remnant photoresist wax. A single large defect box masks this region from further analysis to prevent these features from contaminating measurements.

### 5.1.3. Crosstalk

Crosstalk refers to unwanted signal interference between adjacent pixels or amplifiers. We use an average inter-amp crosstalk correction based on laboratory measurements with LSSTCam. These average corrections proved satisfactory, and so have been used as-is for DP1 processing. There are, however, some residual crosstalk features present post-correction, with a tendency towards over-subtraction. Figure 14 shows an example of a bright star with over-subtracted crosstalk residuals visible on neighboring amplifiers to both sides on exposure 2024120600239, detector R22\_S02.

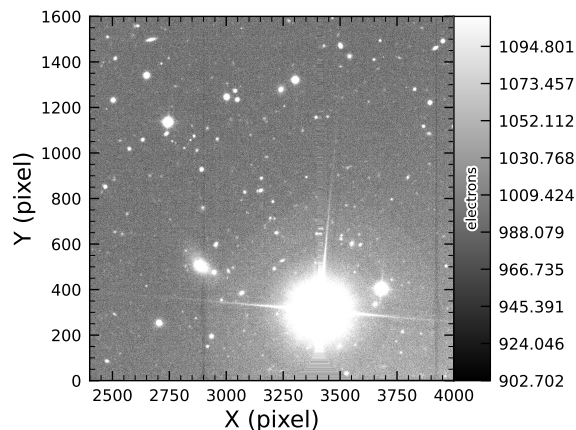


**Figure 14.** An example of a bright star with over-subtracted crosstalk residuals visible on neighboring amplifiers to both sides (exposure 2024120600239, detector R22\_S02). The horizontal banding stretching from the center of the star shows the interpolation stretching covering the saturated core and the ITL edge bleed near the serial register.

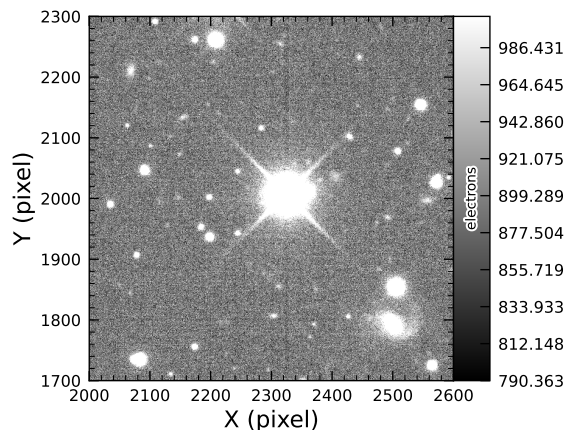


**Figure 15.** A bright star showing the “ITL dip” phenomenon, in which a dark trail extends out from the star to the top and bottom edges of the detector (exposure: 2024121000503, detector: R22\_S21).

#### 5.1.4. Bleed Trails

Bleed trails are produced when charge from saturated pixels spills into adjacent pixels. Bleed trails were anticipated on LSSTComCam sensors, but they appear in more dramatic forms than had been expected. As a bleed trail nears the serial register, it fans out into a “trumpet” shaped feature. Although bright, these features do not have consistently saturated pixels. In DP1 these “edge bleeds” were identified and masked.

Saturated sources can create a second type of bleed, where the central bleed drops below the background level. The depressed columns along these trails extend across the entire readout column of the detector, crossing the detector mid-line. We developed a model for these to identify which sources are sufficiently saturated to result in such a trail, which is then masked. As this kind of trail appears only on the ITL detectors, we’ve named these features “ITL dips”. Figure 15 shows an example of a bright star exhibiting the “ITL dip” phenomenon on exposure: 2024121000503, detector: R22\_S21.

#### 5.2. PSF Models

To characterize PSF performance, we use adaptive second moments (G. M. Bernstein & M. Jarvis 2002) measured on PSF stars and on the PSF model using the HSM implementation (C. Hirata & U. Seljak 2003; R. Mandelbaum et al. 2005). All measurements are expressed in the pixel coordinate frame of each detector. We characterize the performance of the PSF using the classical trace of the second moment matrix  $T$ , along

with the ellipticity parameters  $e^1$  and  $e^2$ . Measurements on the observed PSF stars are denoted as  $T_{\text{PSF}}$ ,  $e_{\text{PSF}}^1$ ,  $e_{\text{PSF}}^2$ , while those from PSF models are denoted as  $T_{\text{model}}$ ,  $e_{\text{model}}^1$ ,  $e_{\text{model}}^2$ . We compare two PSF modeling approaches:

- Piff with second-order polynomial interpolation (Piff O2), the pipeline’s default, and
- Piff with fourth-order polynomial interpolation (Piff O4), which serves as the final DP1 PSF model.

Table 5 summarizes each model’s ability to reconstruct the mean  $T$ , a negative residual bias in the reconstructed PSF size, with Piff O4

An alternative approach to evaluating the performance of the PSF model is to examine the average  $\delta T/T$ , where  $\delta T$  is  $T_{\text{PSF}} - T_{\text{model}}$ , across visits, projected onto focal-plane coordinates, as shown in Figure 16. Piff reveals strong spatial correlations in the residuals, including a systematic offset consistent with the results presented in Table 5. The presence of these spatial structures motivated the adoption of fourth-order polynomial interpolation in all bands except  $u$ -band. Although not shown in Figure 16, residual patterns persist even with third-order interpolation, indicating that it is insufficient to capture the complexity of the PSF variation. Increasing the interpolation order to five would nominally reduce the residuals further, but the limited number of stars available on some CCDs would not provide adequate constraints for such a model, while the resulting improvement would likely be minimal. Preliminary analysis of LSSTCam data in the laboratory at SLAC National Accelerator Laboratory (SLAC) shows that the

**Table 5.** Observed mean values and comparison of model residuals, across all visits and filters

Quantity	Observed	Piff O2	Piff O4
		$\times 10^{-4}$	$\times 10^{-4}$
$\langle T \rangle$ (pixel <sup>2</sup> )	$11.366 \pm 0.003$		
$\langle e^1 \rangle$	$(-6.07 \pm 0.05) \times 10^{-3}$		
$\langle e^2 \rangle$	$(-4.57 \pm 0.05) \times 10^{-3}$		
$\langle e \rangle$	$(8.794 \pm 0.004) \times 10^{-2}$		
$\langle \delta T/T \rangle$		$-4.0 \pm 0.2$	$-5.0 \pm 0.2$
$\langle \delta e^1 \rangle$		$0.6 \pm 0.1$	$0.5 \pm 0.1$
$\langle \delta e^2 \rangle$		$0.0 \pm 0.1$	$0.0 \pm 0.1$

ITL sensors exhibit the same pattern as ITL sensors on LSSTComCam.

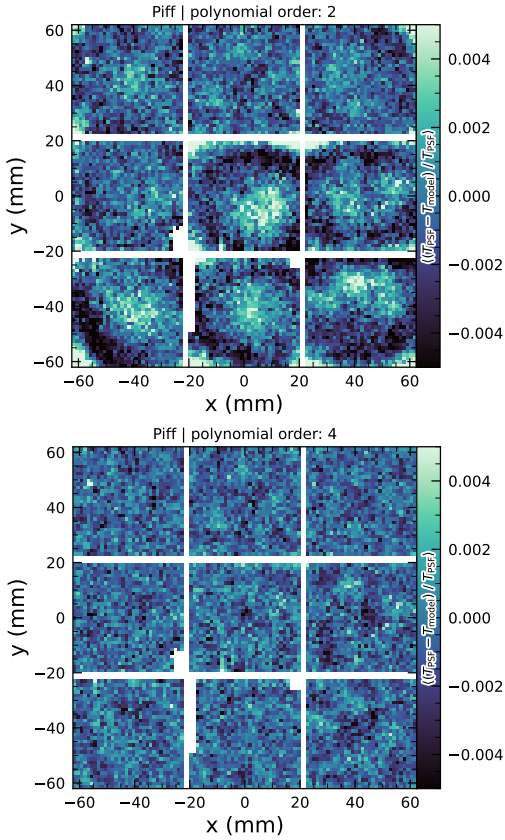


**Figure 16.** Average across all visits of  $\delta T/T$  for Piff O2 and Piff O4 modeling on LSSTComCam. Averages are computed using a  $120 \times 120$  binning.

Another way to look at the PSF modeling quality is via whisker plots of the PSF second and fourth moments and their modeling residuals projected on a part of the sky. In addition to the second moment, the spin-2 fourth

moments,  $e^{(4)}$ , are defined as:

$$e_1^{(4)} = M_{40} - M_{04}$$

$$e_2^{(4)} = 2(M_{31} - M_{13}),$$

where  $M_{pq}$  are the standardized higher moments as defined in T. Zhang et al. (2023) measured on stars and PSF models. Figure 17 shows the whisker plots of  $e$ ,  $e^{(4)}$  (top rows), and  $\delta e$ ,  $\delta e^{(4)}$  in the ECDFS field. The direction of a whisker represents the orientation of the shape, while the length represents the amplitude  $|e|$  or  $|e^{(4)}|$ . We observe coherent patterns in both the PSF moments and the residuals, the latter of which warrants further investigation if it persists in future data releases.

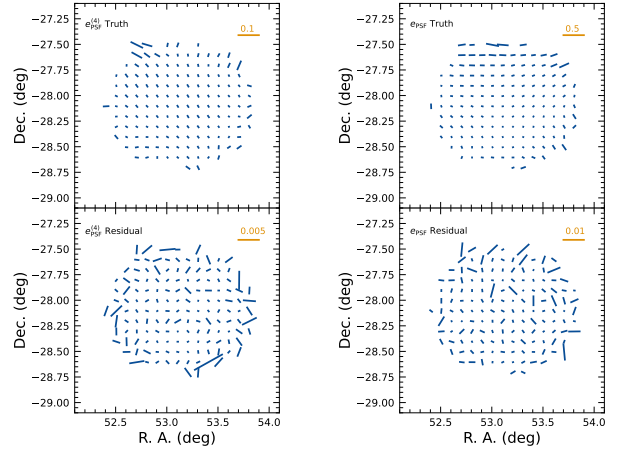
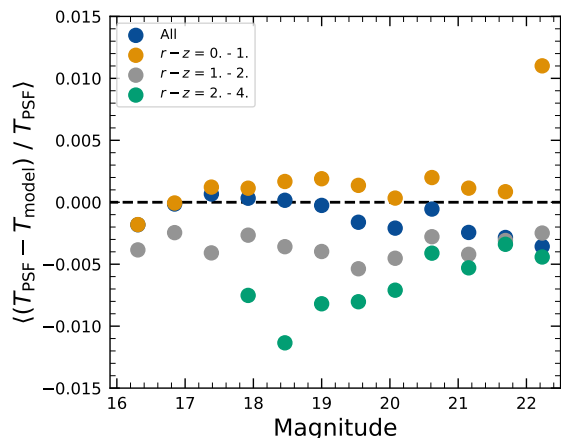


**Figure 17.** Whisker plots for the ECDFS field for  $e$ ,  $e^{(4)}$  and  $\delta e$ ,  $\delta e^{(4)}$ .

Figure 18 shows a plot of  $\delta T/T$  versus stellar magnitude, which can reveal any dependencies between PSF size and flux. We also repeat this analysis in color bins to probe chromatic effects. Binning by color uncovers a clear color dependence, as was also seen in DES (M.

2085 Jarvis et al. 2021). The residual is consistent with Ta-  
 2086 ble 5 and its cause is unknown. DP1 does not include the  
 2087 color correction implemented in the DES Year 6 anal-  
 2088 ysis, T. Schutt et al. (2025). This will be included in  
 2089 processing of future data releases.



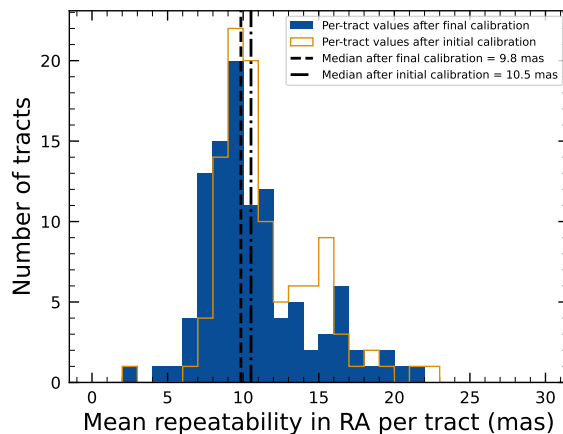
2090 **Figure 18.** Binned  $\delta T/T$  as a function of magnitude across  
 2091 all visits and filters and in bins of stellar colors.

2092 As noted in Rubin Observatory Science Pipelines De-  
 2093 velopers (2025), two key Piff features were not used in  
 2094 the DP1 processing. PSF color dependence was not im-  
 2095 plemented, and, while Rubin software allows Piff to work  
 2096 with sky coordinates (including WCS transformations),  
 2097 it does not yet correct for sensor-induced astrometric  
 2098 distortions such as tree rings (H. Y. Park et al. 2017).  
 2099 Both features are planned for upcoming releases.

### 2100 5.3. Astrometry

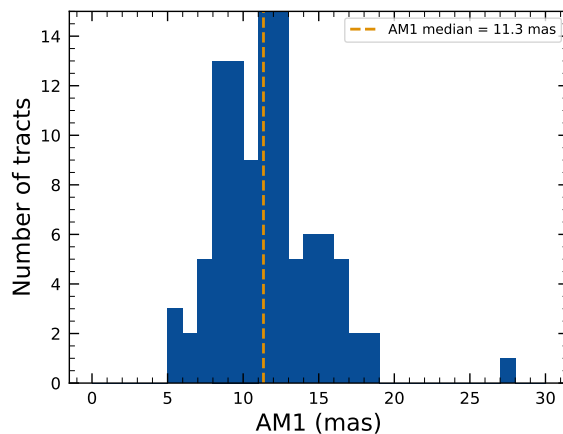
2101 To characterize astrometric performance, we evaluate  
 2102 both internal consistency and agreement with an exter-  
 2103 nal reference. The primary measure of internal consis-  
 2104 tency is the repeatability of position measurements for  
 2105 the same object, defined as the RMS of the astrometric  
 2106 distance distribution for stellar pairs having a specified  
 2107 separation in arcminutes. We associate isolated point  
 2108 sources across visits and compute the rms of their fitted  
 2109 positions, rejecting any stars with another star within  
 2110  $2''$ . Figure 19 shows the median per-tract rms astro-  
 2111 metric error in RA for all isolated point sources, both  
 2112 after the initial calibration and after the final calibra-  
 2113 tion, which includes proper motion corrections. The re-  
 2114 sults indicate that the astrometric solution is already  
 2115 very good after the initial calibration. Global calibra-  
 2116 tion yields only modest improvement, likely due to the  
 2117 short time span of DP1 and the minimal distortions  
 2118 in the LSSTComCam. In the main survey, the longer  
 2119 time baseline and greater distortions near the LSSTCam

2120 field edges will make global calibration more impactful.  
 2121 An additional measure of internal consistency is the re-



2122 **Figure 19.** Mean per-tract astrometric repeatability of  
 2123 measurements of isolated point sources in RA in visits across  
 2124 all bands.

2125 repeatability of separations between objects at a given dis-  
 2126 tance. To compute this, we identify pairs of objects that  
 2127 are separated by a specified distance and measure their  
 2128 precise separation during each visit in which both ob-  
 2129 jects are observed. The scatter in these separation mea-  
 2130 surements provides an indication of the internal consis-  
 2131 tency of the astrometric model. Figure 20 shows the  
 2132 median separation for pairs of objects separated by ap-  
 2133 proximately 5 arcminutes, computed per tract after the  
 2134 final calibration. These values are already approaching  
 the design requirement of 10 mas.



2135 **Figure 20.** Median per-tract repeatability in separations  
 2136 between isolated point sources 5 arcmin apart in visits across  
 all bands.

To assess external consistency, we consider the median separation between sources not included in the astrometric fit and associated objects from a reference catalog (§3.3.3). For this, we use the Gaia DR3 catalog, with the object positions shifted to the observation epoch using the Gaia proper motion parameters. Figure 21 shows the median separation for each visit in the  $r$ -band in `tract` 4849 in the ECDFS fields (Table 6). The calculated values are almost all within 5 mas, well below the design requirement of 50 mas for the main survey. By examining the astrometric residuals, we can assess whether there are distortions not accounted for by the astrometric model. In some cases, residuals from a single visit exhibit behavior consistent with atmospheric turbulence, as shown in Figure 22, which is characterized by a curl-free gradient field in the two-point correlation function of the residuals (E-mode), P. F. Léget et al. (2021) and W. F. Fortino et al. (2021). However, as seen in Figure 23, the residuals in many visits also have correlation functions with a non-negligible divergence-free B-mode, indicating that some of the remaining residuals are due to unmodeled instrumental effects, such as rotations between visits.

We can see unmodeled camera distortions by stacking the astrometric residuals over many visits as a function of the focal plane position. Figure 24 shows the median residuals in  $x$  and  $y$  directions for 1792 visits. Spatial structures are evident at the CCD level, as well as at the mid-line break, the discontinuity between the two rows of amplifiers, in the  $y$ -direction residuals. Further stacking all the detectors makes certain effects particularly clear. Figure 25 shows distortions very similar to those measured for an LSSTCam ITL sensor in a laboratory setting in J. H. Esteves et al. (2023).

#### 5.4. Differential Chromatic Refraction

Differential Chromatic Refraction (DCR) occurs when light passes through Earth’s atmosphere, refracting more for shorter wavelengths, which causes blue light to appear shifted closer to the zenith. This wavelength-dependent effect results in the smearing of point sources along the zenith direction, specifically parallel to the parallactic angle. The DCR effect is observable in LSSTComCam data, particularly in the angular offset versus  $g-i$  band magnitude difference plots, as shown in Figure 26. These plots contain 228 visits chosen to maximize the range of observed airmass. When looking at data perpendicular to the parallactic angle, sources exhibit no discernible DCR effect, which is expected, and form a clear vertical distribution on the two-dimensional density plots in Figure 26.

In contrast, sources aligned with the parallactic angle exhibit a tilted, linear distribution, clearly demonstrating that the relationship between angular offset and the  $g-i$  band magnitude difference, thereby providing a visual indication of the DCR effect. The DCR effect will be addressed in future releases.

#### 5.5. Stellar Photometry

The photometric repeatability for isolated bright unresolved sources following the FGCM fits was excellent. For the 10% of unresolved sources withheld from the fit and having signal-to-noise ratios greater than 100, the photometric repeatability after applying chromatic correction was 7.1, 5.4, 5.4, 5.1, 5.9, and 6.5 mmag in the  $ugrizy$  bands respectively, across all fields. After accounting for photometric noise, the intrinsic photometric repeatability was approximately 4.8, 2.7, 1.7, 1.0, 2.0, and 1.1 mmag in  $ugrizy$ . The DP1 processing does not yet include chromatic corrections in the final photometry. In this case the delivered photometric repeatability was 3–8 mmag for  $grizy$ .

In Figure 27, we show the stellar loci for  $ugriz$  for unresolved sources in the DP1 Object table (§3.2). These unresolved sources were selected using the extendedness parameter (§3.2) in the Object catalog. This parameter is assigned a value of 0 (unresolved) or 1 (resolved) in each band based on the difference between the PSF and CModel magnitudes. The extendedness is set to 1 when this magnitude difference exceeds 0.016 mag, as the PSF flux for extended sources is biased low relative to the CModel flux. This method has been previously employed by the SDSS pipelines, and its statistical properties, including the optimal combination of information from different bands and repeated measurements, are discussed in C. T. Slater et al. (2020).

Figure 28 illustrates the behavior of the extendedness parameter. Its behavior in the  $g$  and  $r$  bands is similar, with unresolved sources scattered around the vertical line centered on zero. The width of the distribution increases towards fainter magnitudes. Resolved sources are found to the right and the dashed lines in the top panels show the adopted “star-galaxy” separation boundary. The morphology of the two color-magnitude diagrams in the bottom panels suggest that the unresolved sample suffers from increasing contamination by galaxies for  $r > 24$ . This behavior is consistent with simulation-based predictions from C. T. Slater et al. (2020).

#### 5.6. Detection Completeness on Coadds

We characterize completeness by injecting synthetic sources into coadded images, and by comparing source

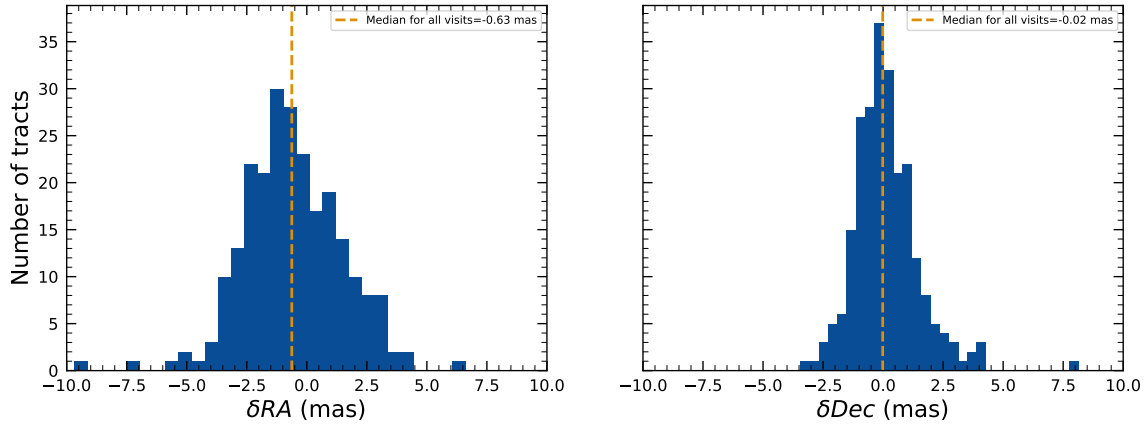


**Figure 21.** Median absolute offset for all visits in  $r$ -band in [tract 4849](#) in the ECDFS field. The offset is the difference between the positions of isolated point sources that were reserved from the astrometric fit and matched objects from the Gaia DR3 catalog.

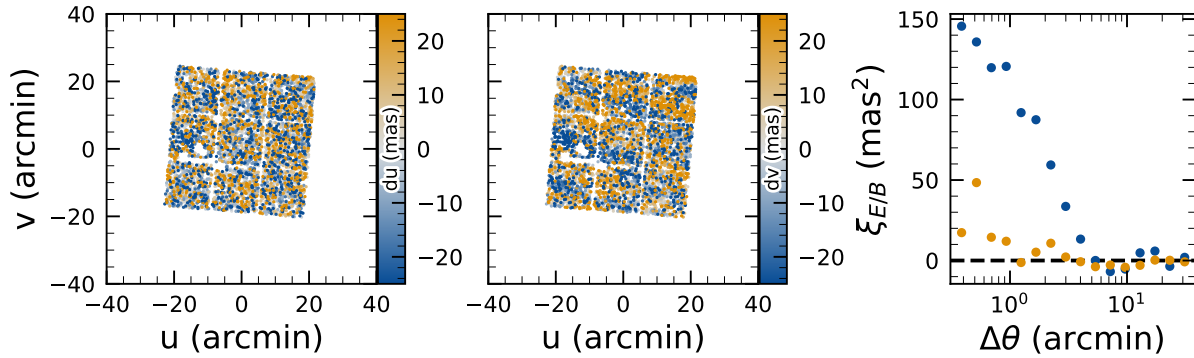


**Figure 22.** Astrometric residuals in  $u$  (left panel) and  $v$  (center panel) directions with the E (blue) and B (orange) modes of the two-point correlation function (right panel) seen in visit 2024120200359 in [tract 2393](#) in  $u$  band. The residuals show a wave-like pattern characteristic of atmospheric turbulence, and there is significant E-mode and negligible B-mode in the correlation function.

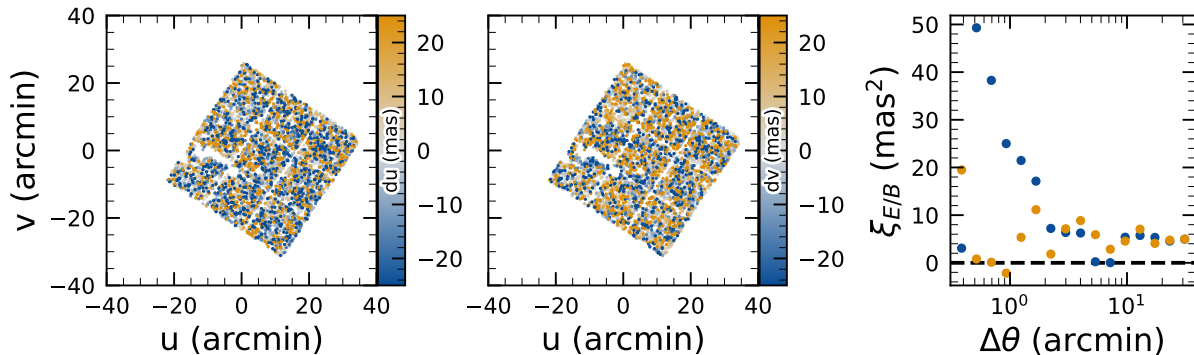


**Figure 23.** Astrometric residuals in  $u$  (left panel) and  $v$  (center panel) directions, with the E (blue) and B (orange) modes of the two-point correlation function (right panel) seen in visit 2024120700527 in [tract 2393](#) in  $u$  band. There are coherent residuals, but without the wave-like pattern seen in [Figure 22](#), and the correlation function has significant values for both E and B-modes.

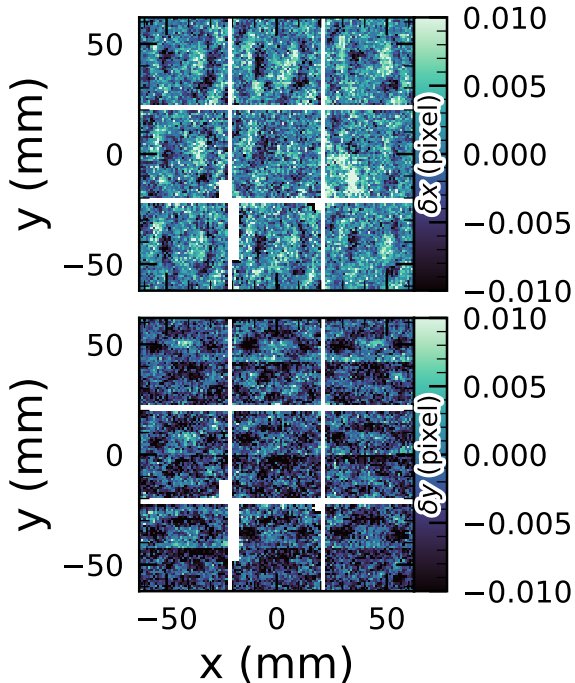


**Figure 24.** Median astrometric residuals as a function of focal plane position, shown in the left panel for the  $x$  direction and in the right panel for the  $y$  direction, for all nine [LSSTComCam](#) CCDs independently. The range of the color scale is  $\pm 0.01$  pixels, corresponding to 2 mas, showing that the effect is small.

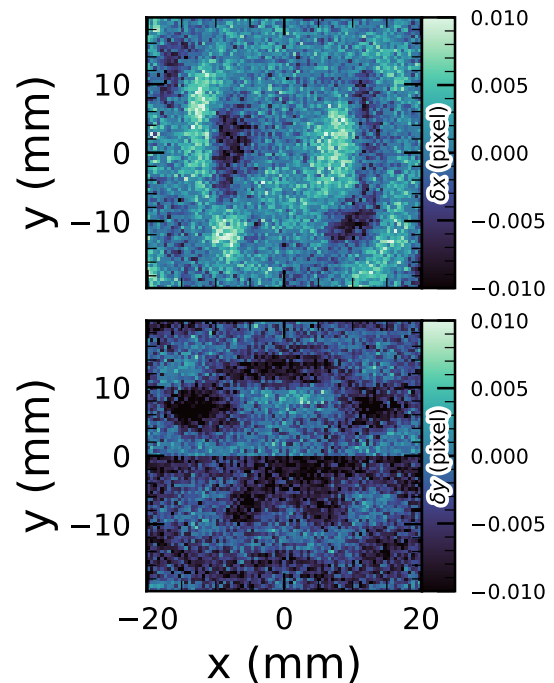


**Figure 25.** Median residuals as a function of pixel position, shown in the left panel for the  $x$  direction and in the right panel for the  $y$  direction. These residuals are aggregated across all nine CCDs that comprise the central [LSSTComCam](#) raft. The range of the color scale is  $\pm 0.01$  pixels, corresponding to 2 mas, showing that the effect is small.

2245 reference objects, in order of descending brightness, to  
 2246 the most likely target within a  $0''.5$  radius.

2247 We inject sources in 12 of the patches of the [ECDFS](#)  
 2248 region with the deepest coverage. The input catalog con-  
 2249 tains stars and galaxies from part of the [Data Challenge](#)  
 2250 [2 \(DC2\) simulations \(LSST Dark Energy Science Col-](#)  
 2251 [laboration \(LSST DESC\) et al. 2021](#)), where the galaxies  
 2252 consist of an exponential disk and de Vaucouleurs (G.  
 2253 de Vaucouleurs 1948, 1953) bulge. To avoid deblender  
 2254 failures from excessive increases in object density, stars  
 2255 with a total flux (i.e., summed across all six bands)  
 2256 brighter than 17.5 mag are excluded, as are galaxies  
 2257 whose total flux is brighter than 15 mag or fainter than  
 2258 26.5 mag. Half of the remaining objects are selected for  
 2259 injection. Afterwards, individual bulge and disk compo-  
 2260 nents fainter than 29 mag are also excluded, both  
 2261 for computational expediency and because their struc-  
 2262 tural properties are less likely to be representative of  
 2263 real galaxies.

2265 [Figure 29](#) shows completeness as a function of mag-  
 2266 nitude for these injected objects in the [ECDFS](#) field.  
 2267 These completeness estimates are comparable to results  
 2268 from matching external catalogs. Matching to the Hub-

2269 ble Legacy Field catalog (G. [Illingworth et al. 2016](#);  
 2270 K. E. [Whitaker et al. 2019](#)) reaches 50% completeness  
 2271 at  $F775W = 26.13$ , or about  $i = 25.83$  from differences  
 2272 in matched object magnitudes. Similarly, completeness  
 2273 drops below 90% at  $VIS = 23.80$  from matching to  
 2274 Euclid Q1 ([Euclid Collaboration et al. 2025](#)) objects,  
 2275 equivalent to roughly  $i = 23.5$ . The Euclid imaging is of  
 2276 comparable or shallower depth, so magnitude limits at  
 2277 lower completeness percentages than 90% are unreliable,  
 2278 whereas the HST images cover too small and irregular of  
 2279 an area to accurately characterize 80-90% completeness  
 2280 limits.

2281 At the 80% completeness limit, nearly 20% of objects,  
 2282 primarily injected galaxies, are incorrectly classified as  
 2283 stars based on their reference band extendedness. Simi-  
 2284 larly, the fraction of correctly classified injected stars  
 2285 drops to about 50% at  $i = 23.8$  (corresponding to 90%  
 2286 completeness).

2287 This analysis has several caveats. The selection of  
 2288 objects for matching in any catalog is not trivial. Some  
 2289 fraction of the detections are spurious, particularly close  
 2290 to bright stars and their diffraction spikes. Additionally,  
 2291 some objects lie in masked regions of one survey but not

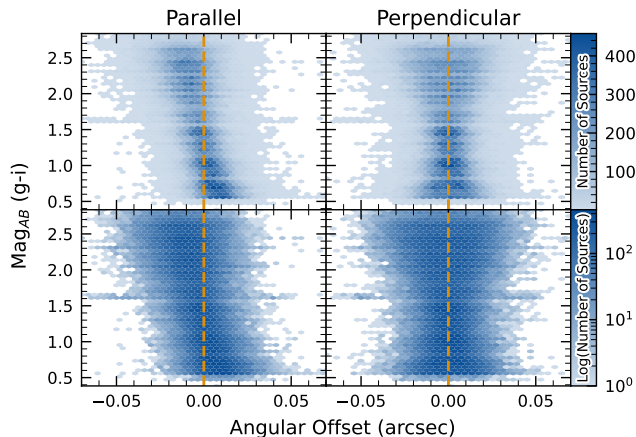


**Figure 26.** Visualization of [Differential Chromatic Refraction \(DCR\)](#) observed in the [LSSTComCam](#) commissioning campaign. The  $g - i$  color is computed for every source in the reference catalog (§3.3.3) that is matched to a direct source in the science image, and the binned density for the full survey is plotted against the angular offset between the reference and detected positions. The angular offset is projected along coordinates parallel and perpendicular to the parallactic angle of the observation, and shows a characteristic correlation along the parallel axis with no correlation along the perpendicular axis. The orange vertical dashed line indicates the expected  $g - i$  magnitude distribution at zero angular offset.

2292 another, which has not been accounted for. For injected  
 2293 source matching, the reference catalog (§3.3.3) does not  
 2294 include real on-sky objects. Based on prior analyses of  
 2295 the [DC2](#) simulations, purity is generally greater than  
 2296 completeness at any given magnitude. Similarly, for  
 2297 bright ( $i < 23$ ) objects classified as stars by reference  
 2298 band extendedness,  $< 5\%$  are either unmatched to a Eu-  
 2299 clid or HST object, or misclassified - that is, selecting on  
 2300 extendedness alone yields a fairly pure but incomplete  
 2301 sample of stars. We expect to remedy some of these  
 2302 shortcomings in future releases.

### 2303 5.7. Model Flux and Shape Measurement

2304 [Figure 30](#) shows  $i$ -band magnitude residuals for  
 2305 CModel and Sérsic measurements using the matched in-  
 2306 jected galaxies described in §5.6. Similar behavior is  
 2307 seen in other bands. Sérsic fluxes show reduced scatter  
 2308 for galaxies with  $i < 22.5$ , though CModel fluxes are  
 2309 less biased, with median residuals closer to zero and less  
 2310 magnitude-dependent. For fainter objects, Sérsic fluxes  
 2311 are more biased and less accurate. The magnitude of  
 2312 this bias is considerably larger than previously seen in  
 2313 simulated data. Subsequent testing indicates that this  
 2314 bias can be (roughly) halved by fitting an exponential  
 2315 model first, and then using those parameters to initialize

2316 a free Sérsic fit. This approach will be adopted in future  
 2317 releases. Aperture fluxes - including Kron and [GAaP](#) -  
 2318 are not shown as they are not corrected to yield total  
 2319 fluxes. The correction for Kron fluxes can be derived  
 2320 from the Sérsic index ([A. W. Graham & S. P. Driver](#)  
 2321 [2005](#)), but this correction is not provided in object ta-  
 2322 bles.

2323 [Figure 31](#) shows  $g - i$  color residuals versus  $r$ -band  
 2324 magnitude for the same sample of galaxies as [Figure 30](#).  
 2325 For this and most other colors, [GAaP](#) (with a  $1''$  aper-  
 2326 ture) and Sérsic colors both yield lower scatter; however,  
 2327 the CModel colors have the smallest bias. Curiously,  
 2328 the [GAaP](#) bias appears to be magnitude-dependent,  
 2329 whereas the Sérsic bias remains stable from  $19 < r < 26$ .  
 2330 Any of these color measurements are suitable for use  
 2331 for deriving quantities like photometric redshifts, stellar  
 2332 population parameters, etc.

2333 In addition to photometry, some algorithms include  
 2334 measurements of structural parameters like size, ellip-  
 2335 ticity, and Sérsic index. One particular known issue is  
 2336 that many (truly) faint objects have significantly overes-  
 2337 timated sizes and fluxes. This was also seen in the Dark  
 2338 Energy Survey ([K. Bechtol et al. 2025](#)), who dubbed  
 2339 such objects “super-spreaders”. These super-spreaders  
 2340 contribute significantly to overestimated fluxes at the  
 2341 faint end (see e.g. [Figure 30](#)), and are particularly prob-  
 2342 lematic for the Kron algorithm ([R. G. Kron 1980](#)), which  
 2343 should only be used with caution.

2344 As mentioned in §4.5, the Sérsic fits include a free  
 2345 centroid, which is initialized from the fiducial centroid  
 2346 of the object. Preliminary analyses of matched injected  
 2347 objects suggest that the Sérsic model galaxy [astrom-](#)  
 2348 [etry](#) residuals are somewhat smaller than for the stan-  
 2349 dard centroids used in other measurements, and so users  
 2350 of the Sérsic photometry should also use these centroid  
 2351 values. One caveat is that for faint objects and/or in  
 2352 crowded regions with unreliable deblending, free cen-  
 2353 troids can drift significantly and potentially towards  
 2354 other objects, so objects with large differences between  
 2355 the fiducial and Sérsic [astrometry](#) should be discarded  
 2356 or used with caution.

2357 Sérsic model parameter uncertainties are estimated  
 2358 by computing and inverting the Hessian matrix with  
 2359 the best-fit parameter values, after replacing the pixel  
 2360 data (but not uncertainties) by the best-fit model values.  
 2361 Currently, only the on-diagonal dispersion term (square  
 2362 root of the variance) is provided as an error estimate for  
 2363 each parameter. Future releases may provide more off-  
 2364 diagonal terms of the covariance matrix - particularly  
 2365 for the structural parameters, which are known to be  
 2366 correlated.

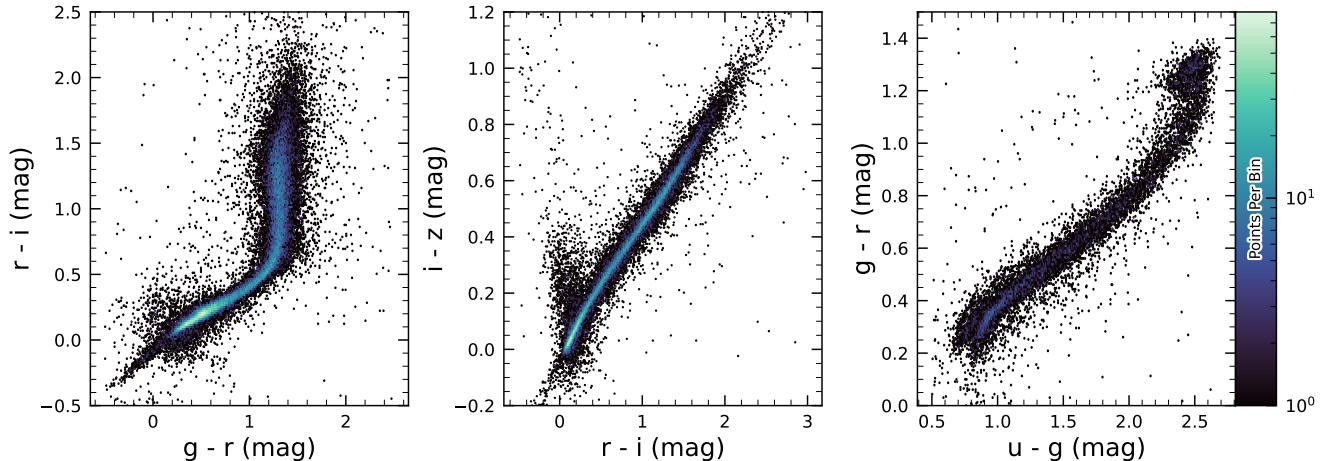


**Figure 27.** Examples of stellar loci for unresolved sources from the DP1 dataset. From left to right: *gri* stellar locus containing 63,236 stars with signal-to-noise ratio  $> 200$  in the *i* band; *riz* stellar locus containing 46,760 stars with signal-to-noise ratio  $> 200$  in the *i* band; *ugr* stellar locus containing 12,779 stars with signal-to-noise ratio  $> 50$  in the *u* band.

A major outstanding issue is that many parameter uncertainties - including but not limited to those for fluxes - are underestimated. This is at least partly (but not wholly) due to the fact that coaddition introduces covariance between pixels, which is not captured in per-pixel variances.

The degree to which uncertainties are underestimated can depend on the parameter in question and on the brightness of the object. In plots of uncertainty-scaled residuals, the ideal behavior is for the median (i.e. the bias) to lie close to zero, and for the  $\pm 1\sigma$  lines to lie at  $\pm 1$ , without any dependence on magnitude. Figure 32 shows that flux and color uncertainties for PSF model magnitudes of injected stars are both underestimated, but by a factor of approximately 1.7–2 that is not very sensitive to SNR. This holds for astrometric/centroid parameters as well.

In turn, Figure 33 shows that CModel color uncertainties of galaxies are underestimated by a similar factor at the faint end, but with appreciable scaling with magnitude (and thereby SNR). Flux error underestimation is both larger than for colors and scales more strongly with SNR. This indicates that systematic effects dominate the errors in fluxes, particularly for bright galaxies. This is also at least partly but not wholly due to so-called model inadequacy - that is, the fact that galaxy models, parametric or otherwise, are insufficiently complex to capture the structure of real galaxies.

Figure 34 shows that Sérsic model fluxes and colors have similar behavior as CModel, but with a greater degree of overestimation. This may be partly due to the fact that Sérsic parameter uncertainties are estimated along with the free centroid and structural (shape and

Sérsic index) parameters, whereas the forced CModel fluxes and errors are derived from linear flux fits with a fixed shape and centroid.

Efforts are underway to investigate and quantify the origin of uncertainty underestimates and future releases will, at the least, provide recommendations for mitigations.

## 5.8. Difference Imaging

We assessed the performance of image differencing using both human vetting (§5.8.1) and source injection (§5.8.2).

### 5.8.1. Difference Imaging Purity

Members of the DP1 team labeled more than 9,500 DIASource image triplets, each consisting of cutouts from the science, template, and difference images. An internal labeling service (TASSO) was deployed within the USDF environment. A random subset of approximately 500,000 DIASources was selected and uploaded to the service, which remained active for roughly three months. Access to the labeling service was granted to all individuals with commissioning data access. Each DIASource was classified exactly once, with a total of 35 volunteers contributing labels. Volunteers reviewed PNG images displaying the template, science, and difference stamps; each stamp had dimensions of  $51 \times 51$  pixels, matching the input size required by the machine-learning model. Figure 35 show an example of one of the image triplets consisting of cutouts from the science, template, and difference images that volunteers were asked to label.

The labeled sources were classified into multiple categories representing real astrophysical events and artifacts. Prior to any filtering, the raw artifact-to-real ratio

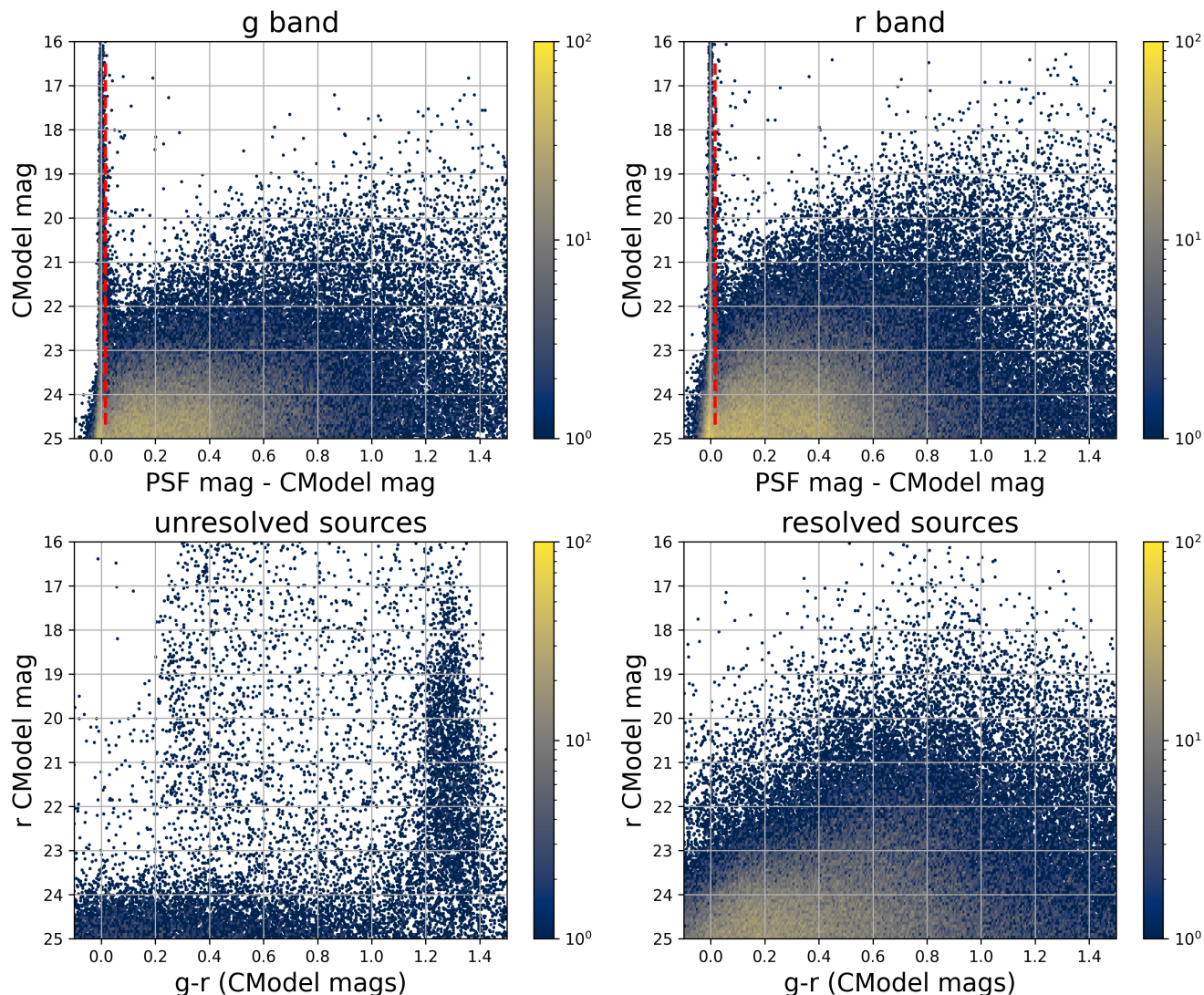


**Figure 28.** The top two panels show the difference between the PSF and CModel magnitudes as a function of CModel magnitude in the  $g$  and  $r$  bands for 178,547 sources with  $CModel_r < 25$  from the ECDFS field. The vertical dashed line in each panel marks the minimum value (0.016 mag) for setting the extendedness parameter to 1. The bottom two panels show the  $r$  vs.  $g - r$  color-magnitude diagrams for 14,701 unresolved (left) and 163,666 resolved (right) sources. Note the unresolved sample suffers from increasing contamination by galaxies for  $r > 24$ .

2433 was approximately 9:1. Bright stars were identified as  
 2434 the dominant source of artifacts, while correlated noise,  
 2435 particularly in the  $u$  and  $g$  bands, also produced spuri-  
 2436 ous detections near the flux threshold. We expect to be  
 2437 able to mitigate these effects in future LSSTCam data.

2438 Applying a reliability threshold improves the purity of  
 2439 transient detections but has limited impact on variable  
 2440 stars. This limitation arises from technical constraints  
 2441 at the time of model training, which prevented the in-  
 2442 jection of variable stars into the synthetic training set.  
 2443 Future reliability models for LSSTCam data, described  
 2444 in §4.6.1, will be trained using a broader and more rep-  
 2445 resentative range of input data.

### 2446 5.8.2. Difference Imaging Detection Completeness

2447 We assess the performance of our difference imaging  
 2448 pipeline using synthetic source injection on the science  
 2449 images prior to differencing. We construct a catalog of  
 2450 injected sources by joining two different samples of point  
 2451 sources, a set of hosted sources to emulate transients in  
 2452 galaxies and second set of hostless sources. The hosts  
 2453 are selected from the pipeline source catalog that is pro-  
 2454 duced upstream by imposing a cut on their extendedness  
 2455 measurement and selecting  $N_{\text{src}} = \min(100, N \times 0.05)$  of  
 2456 the  $N$  available sources per detector. For each host we  
 2457 pick a random position angle and radius using its light  
 2458 profile shape to decide where to place the source, and

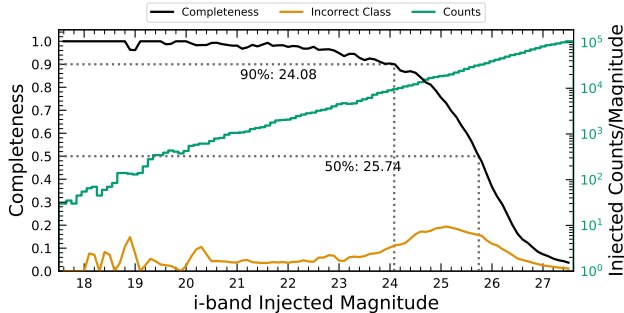


**Figure 29.** Completeness and incorrect classification fraction as a function of  $i$ -band CModel magnitude (Reference Magnitude) for DC2-based injected objects into a portion of the ECDFS field. The “Incorrect Class” line shows the proportion of objects that are matched but classified incorrectly by their reference-band extendedness, i.e. stars with extendedness of 1 or galaxies with extendedness of 0 in the reference band.

also a random value of brightness for the injected source, with magnitudes higher than the host source.

The hostless sources instead have random positions in the CCD focal plane, and magnitudes chosen from a random uniform distribution with  $20 \geq m \geq m_{lim} + 1$ , where  $m_{lim}$  is the limiting magnitude of the image. We used the `LSST source_injection` package<sup>103</sup> to include these sources in our test images. We performed a coordinate cross-match task, with a threshold of 0.5 to find which of these sources were detected and which were lost, enabling the calculation of a set of performance metrics.

In Figure 36 we show the detection completeness as a function of the SNR, for sources in the ECDFS field, for filters *griz*. We observe a completeness  $> 95\%$  for sources with  $SNR > 6$ , with mean completeness  $\simeq 99\%$  and standard deviation of  $\simeq 0.7\%$ . In Figure 37 we show the distribution of the residuals of the recovered sky coordinates for the detected synthetic sources. The marginal distributions are both centered at zero, and for sources of  $SNR > 20$  the residuals are compatible with normal distributions  $\mathcal{N}(\mu = 0, \sigma^2 = (0''.02)^2)$ . In Figure 38 we show photometry results for our detected synthetic sources in the  $i$  filter, using PSF photometry on the difference images. We include both the magnitude residuals as well as the flux pulls, defined as  $(f_{PSF} - f_{True})/\sigma_{f_{PSF}}$  for PSF flux  $f_{PSF}$  and error  $\sigma_{f_{PSF}}$ , as a function of the true magnitude of the synthetic sources, including the running median and median absolute deviation (MAD) for the whole brightness

<sup>103</sup> <https://pipelines.lsst.io/modules/lsst.source.injection/index.html>

range. We also include the true magnitude distribution as well as the detection completeness on the top panel, and for reference the 90% and 50% completeness magnitude values in vertical lines. On the right panels we include the marginal distribution for sources brighter than  $mag < 22.5$ , splitting the data into hosted and hostless, as well as the robust mean and standard deviation. From this figure we can see that our flux measurements are accurate within a wide range of magnitudes, for both hosted and hostless synthetic sources. We find that the median offset is below 0.002 mag for true magnitudes below 21, and with a maximum  $\sigma_{MAD}$  scatter of about 0.02 mag in this range. For true  $m_i < 22.5$ , the robust running median PSF magnitude residuals are  $< 0.02$  mag, and when splitting into hosted and hostless both robust median are well below 0.01, and robust  $\sigma$ , i.e.  $\sigma_{MAD}$  are also well below 0.05. For all sources with  $m_i < 21.5$  the running median is always  $|\langle \delta \rangle| < 0.1$ , and  $MAD \sigma_\delta < 1$ . Extending to sources with  $m_i < 22.5$  then hostless sources have a robust mean pull below 0.02, with a robust standard deviation  $< 1.15$ , while these parameters increase to 0.2 and 1.2 for hosted sources, suggesting that we might have contamination from host background sources potentially biasing our fluxes.

## 5.9. Solar System

### 5.9.1. Asteroid Linking Performance

The evaluation of asteroid linking performance in DP1 focused on demonstrating discovery capability. The solar system discovery pipeline produced 269,581 tracklets, 5,691 linkages, and 281 post-processed candidates.

As described in §4.6.3, post-processing of the `heliolinc` output with `link_purify` produced a final set of 281 candidate linkages, ranked with the most promising first. We then used `find_orb` (B. Gray 2025) to derive orbit fits for each candidate, sorting the resulting list by  $\chi^2_{dof}$ , a measure of fit quality. A conservative manual investigation of these candidates yielded a curated list of 93 probable new asteroid discoveries. Manual inspection of the linkages indicated that those ranked 0–137 corresponded to unique real asteroids; ranks 138–200 contained additional real objects intermixed with some spurious linkages; and ranks higher than 200 were essentially all spurious. This analysis indicates that it will be possible to identify cuts on quality metrics such as  $\chi^2$  to define discovery candidate samples with high purity; determining the exact quantitative cut values requires more data with LSSTCam. We next removed all observations matched to known asteroids (using Minor Planet Center (MPC)’s MPCChecker service), reducing the number of candidates to 97. Of these, four had strong astrometric and/or photometric outliers, likely

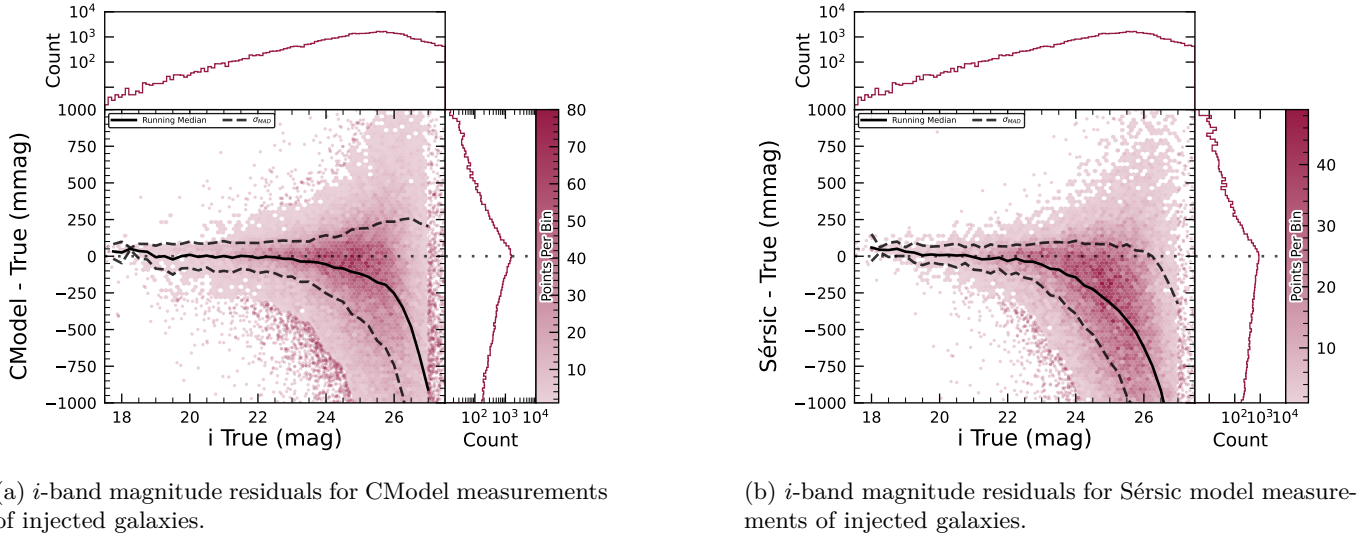


**Figure 30.**  $i$ -band magnitude residuals for matched injected DC2 galaxies with the CModel and Sérsic algorithms in a portion of the ECDFS region, including the median and scatter thereof. The black line is the median.

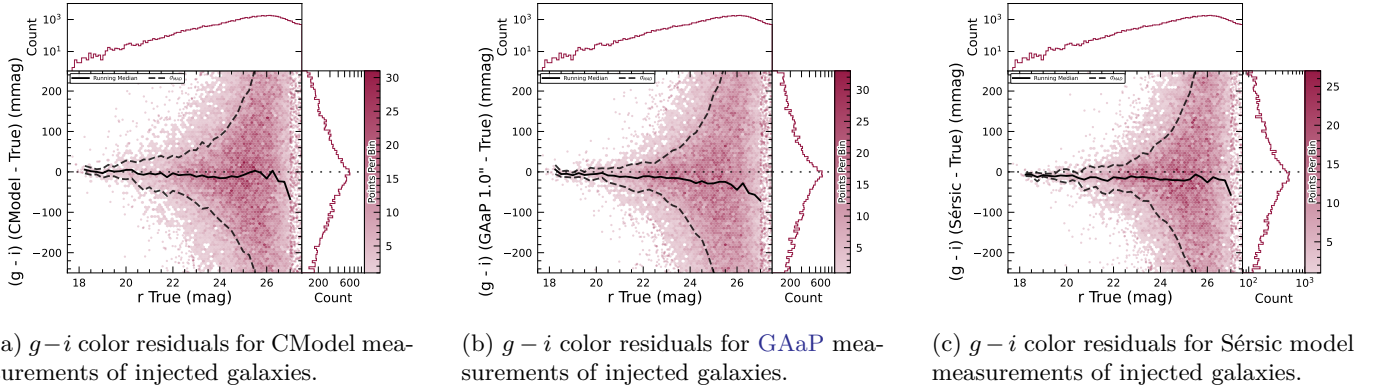


**Figure 31.**  $g - i$  color residuals versus true  $r$ -band magnitude for matched injected DC2 galaxies with the CModel, GAaP and Sérsic algorithms in a portion of the ECDFS region.

2543 due to self-subtraction in difference images due to the  
 2544 unavoidable limitations of template generation from the  
 2545 limited quantity of data available from LSSTComCam.  
 2546 We suspect these four linkages do correspond to real objects,  
 2547 but have chosen to discard them out of an abundance of caution.  
 2548 The remaining 93 were submitted to the Minor Planet Center  
 2549 and accepted as discoveries, demonstrating the LSST pipelines  
 2550 are able to successfully discover new solar system objects.  
 2551

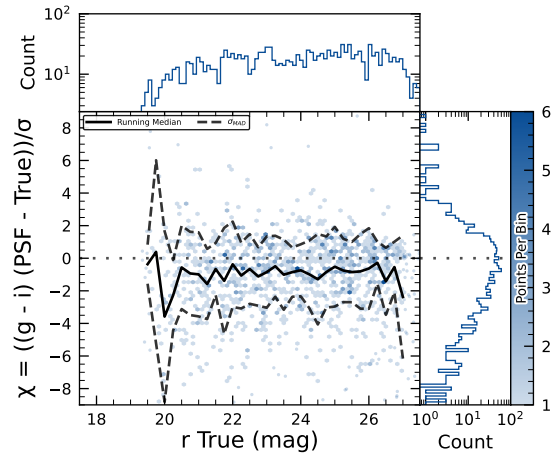
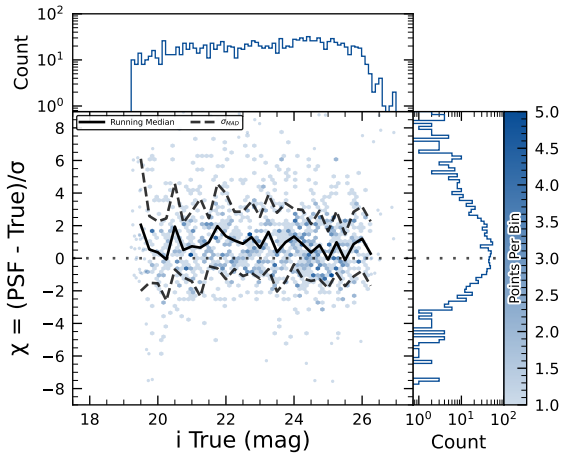
### 2552 5.9.2. Asteroid Association Performance

2553 During the Solar System association step, 5988 DiaSources  
 2554 were linked to 431 unique Solar System objects, These include  
 2555 3,934 DiaSources with 338 previously known objects cataloged  
 2556 by the MPC, and 2,054 DiaSources with the 93 newly-discovered  
 2557 objects. An additional 143 detections of these newly discovered  
 2558 objects were also recovered. These detections were not  
 2559

2560 initially identified by the discovery pipelines, as they  
 2561 did not meet the required criteria for tracklet formation,  
 2562 specifically the minimum number of detections and/or  
 2563 the maximum allowed time span between observations.

The astrometric residuals of known asteroid associations  
 2564 are shown in Figure 39. The astrometric precision for solar  
 2565 system sources is excellent, with the majority of objects  
 2566 detected within  $0''.1$  of their expected positions.

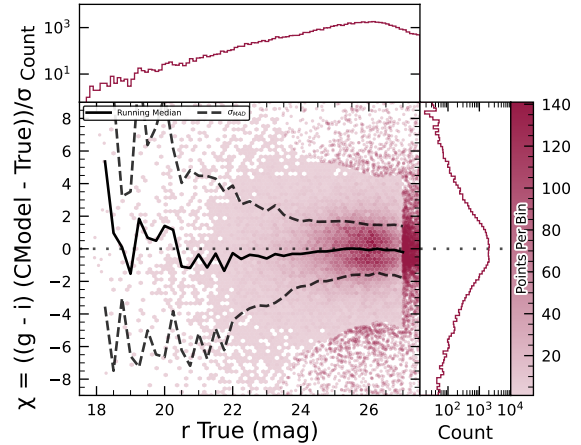
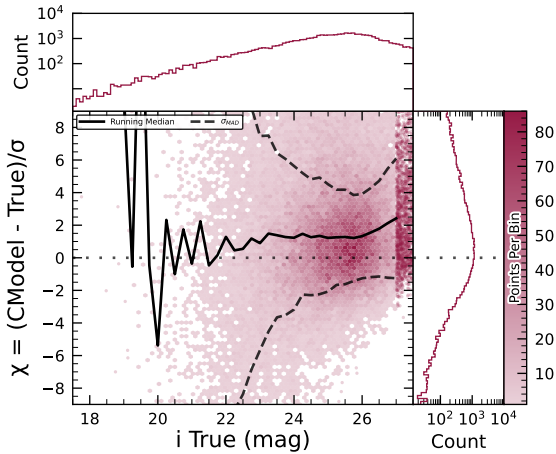
By analyzing the signed median residuals to search for  
 2567 biases, we find that previously-known objects have mean  
 2568 residuals of  $0''.001$  and  $-0''.016$  in the RA and Dec directions  
 2569 respectively, whereas newly-discovered objects have mean  
 2570 residuals of  $-0''.035$  and  $-0''.010$  in the RA and Dec  
 2571 directions, respectively. These mean residuals are small  
 2572 enough to eliminate the possibility of a timing offset greater  
 2573 than the second-scale shutter motion, which is consistent with  
 2574 the timing studies presented in §2.2.2.  
 2575  
 2576  
 2577



(a)  $i$ -band flux uncertainty-scaled residuals for PSF model measurements of injected stars.

(b)  $g - i$  color uncertainty-scaled residuals for PSF model measurements of injected stars.

**Figure 32.** Color and flux uncertainty-scaled residuals for matched injected DC2 stars’ PSF model measurements in a portion of the ECDIFS region.



(a)  $i$ -band flux uncertainty-scaled residuals for CModel measurements of injected galaxies.

(b)  $g - i$  color uncertainty-scaled residuals for CModel measurements of injected galaxies.

**Figure 33.** Color and flux uncertainty-scaled residuals for matched injected DC2 galaxies’ CModel measurements in a portion of the ECDIFS region.

2578 The wider scatter in the RA residuals is due to objects  
 2579 whose measured orbital elements are less well con-  
 2580 strained, translating to larger along-track positional er-  
 2581 rors in the predicted positions. Observations of objects  
 2582 with large residuals are the most valuable ones from the  
 2583 point of view of improving the orbit, which is why we  
 2584 kept a generous matching radius. However, in future re-  
 2585 leases we are likely to couple this with either orbit fit-  
 2586 ting to verify the “singleton” match, or require two near-in-  
 2587 time observations (a tracklet) that match the expected  
 2588 motion vector as well.

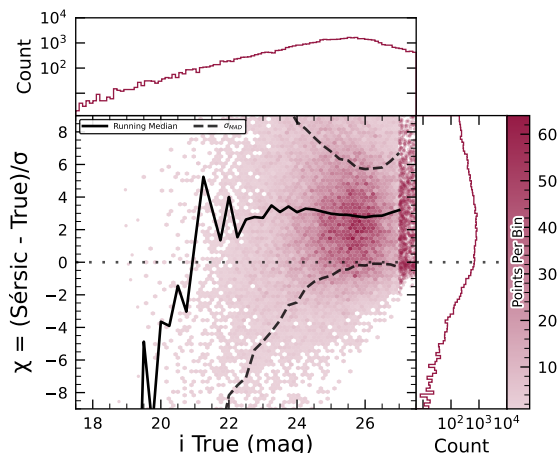
2589 Optimal moving source attribution is an area of ac-  
 2590 tive work that we expect to fully converge in time of  
 2591 [Data Release 1 \(DR1\)](#). In the meantime, for DP1 we’ve

2592 opted to start with simple, more easily understandable,  
 2593 criteria.

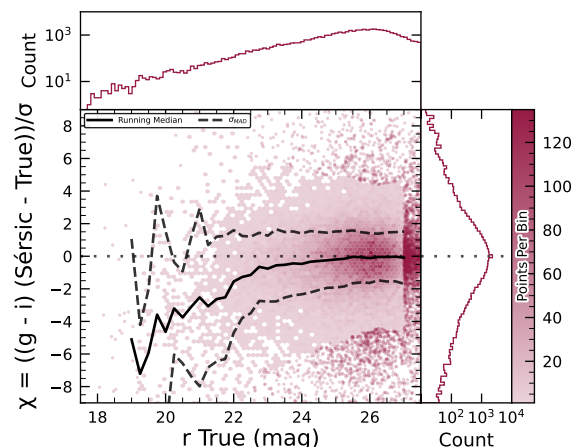
### 5.10. Crowded Fields

2594 Among the seven Rubin DP1 target fields, two stand  
 2595 out for their severe stellar crowding: the globular cluster  
 2596 47 Tucanae (47\_Tuc) and the Fornax dwarf spheroidal  
 2597 galaxy (Fornax dSph). These fields were selected in part  
 2598 to stress-test the LSST Science Pipelines under high-  
 2599 density conditions. While both exhibit high stellar den-  
 2600 sities, the nature and spatial extent of the crowding dif-  
 2601 fer significantly.

2602 47 Tuc presents extreme crowding across much of the  
 2603 field, encompassing its dense core and the eastern re-  
 2604



(a)  $i$ -band flux uncertainty-scaled residuals for Sérsic model measurements of injected galaxies.



(b)  $g-i$  color uncertainty-scaled residuals for Sérsic model measurements of injected galaxies.

**Figure 34.** Color and flux uncertainty-scaled residuals for matched injected DC2 galaxies' Sérsic measurements in a portion of the ECDFS region.

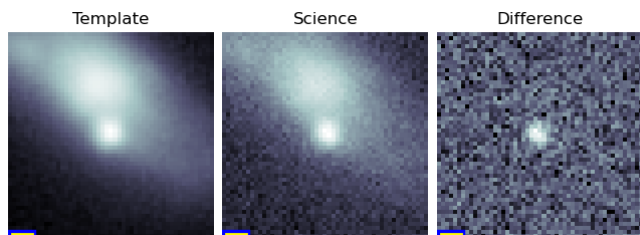


**Figure 35.** An example an image triplet consisting of cutouts showing, from left to right, the science, template, and difference images that volunteers were asked to label.

2605 regions influenced by the Small Magellanic Cloud (SMC).  
 2606 This pervasive crowding leads to persistent challenges  
 2607 for deblending and reliable source detection, exposing  
 2608 field-wide limitations in the current pipeline performance (Y. Choi et al. 2025). In contrast, Fornax dSph  
 2609 shows significant crowding only in its central region,  
 2610 with outer areas remaining well resolved and easier to  
 2611 process.  
 2612

2613 In both 47Tuc and Fornax, extreme crowding led  
 2614 to the deblending step being skipped frequently when  
 2615 memory or runtime limits were exceeded, typically due  
 2616 to an excessive number of peaks, or large parent foot-  
 2617 prints. However, the impact of these limitations differed:  
 2618 in 47Tuc, deblending was often skipped across the  
 2619 entire field, resulting in large gaps and substantially re-  
 2620 duced completeness. In Fornax, these issues were largely  
 2621 confined to the central region, with much better recov-  
 2622 ery in the outskirts. This contrast highlights how the  
 2623 pipeline's limitations depend on the spatial extent of  
 2624 high-density regions: 47Tuc exposed systematic, field-  
 2625 wide challenges, whereas Fornax revealed more localized,  
 2626 density-driven limits.

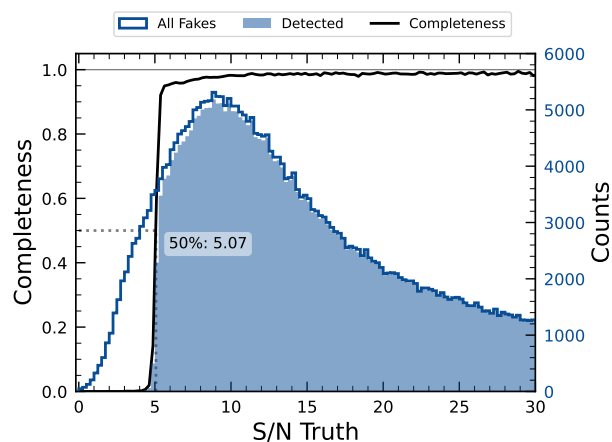


**Figure 36.** The difference image detection completeness for injected sources in the ECDFS field, for filters  $griz$ , as a function of the estimated signal to noise ratio SNR. This completeness is the ratio between the found fake sources (shaded histogram) and all the sources (solid line). The horizontal dashed line represents where the 50% completeness level is reached, at approximately SNR  $\simeq 5.07$ .

2627 T. M. Wainer et al. (2025) explored the Rubin DP1  
 2628 DiaObject catalog (§3.2) in the 47Tuc field, which con-  
 2629 tains sources detected in difference images. Because  
 2630 forced photometry is performed at these positions across  
 2631 all single-epoch images, this dataset bypasses the coadd-  
 2632 based detection and deblending stages that often fail  
 2633 in crowded regions. By computing the median of the  
 2634 forced photometry for each DiaObject across available  
 2635 visits, they recovered approximately three times more  
 2636 candidate cluster members than found in the standard  
 2637 Object table (Y. Choi et al. 2025). This result un-

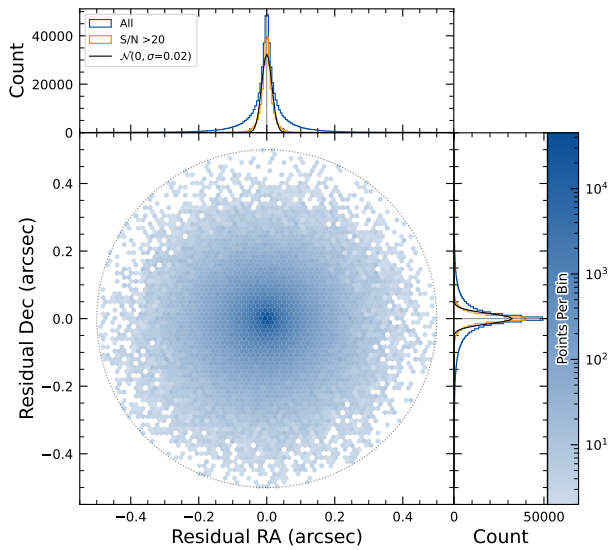


**Figure 37.** Coordinate residuals for detected synthetic sources in difference images, between recovered and true position of the sources in the ECDFS field. In the top and right panels we include the distribution of these offsets, for all sources as well as for sources with SNR > 20. These high SNR sources show gaussian coordinate residual distributions with  $\sigma = 0''.02$  (black solid lines). The circle reflects the matching radius of  $0''.5$ .

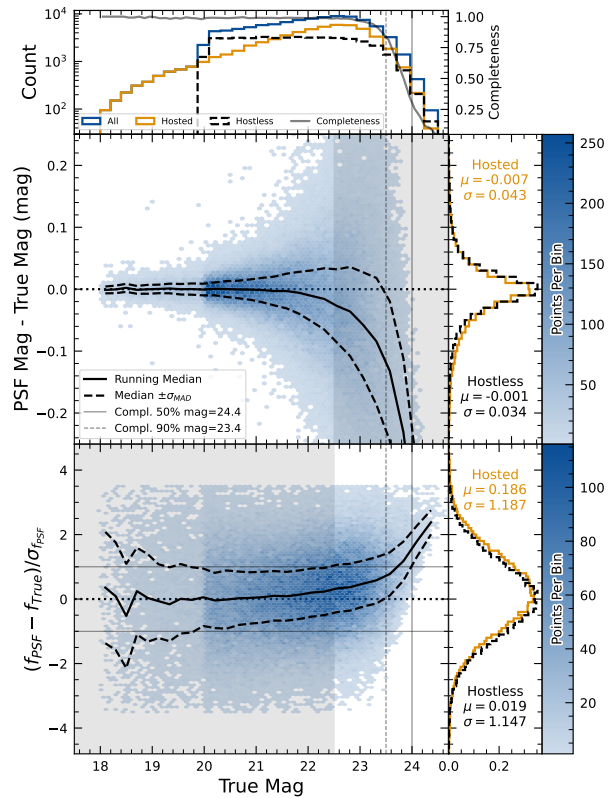


**Figure 38.** Magnitude residuals and flux pulls for *i*-band PSF photometry on difference images for ECDFS field in *i* for detected injected sources. Top panel: Distribution of true magnitudes for injected sources (blue), and split into hostless (black dash) and hosted (orange) sources, with detection completeness as a function of true magnitude (gray line). Vertical dashed lines indicate the 90% and 50% completeness magnitude limits. Center left panel: 2D hexbin plot of PSF magnitude residuals (measured minus true) versus true magnitude for detected sources, with running median (solid black) and  $\sigma_{MAD}$  (dashed black) overlaid. Center right panel: Marginalized distributions of PSF magnitude residuals for hostless (blue) and hosted (orange) sources with true magnitude  $m_i < 22.5$ , annotated with robust mean and standard deviation. Bottom left panel: 2D hexbin plot of PSF flux pulls versus true magnitude for detected sources, with running median (solid black) and  $\sigma_{MAD}$  (dashed black) overlaid. Bottom right panel: Marginalized distributions of PSF flux pulls for hostless (blue) and hosted (orange) sources with true magnitude  $m_i < 22.5$ , annotated with robust mean and standard deviation.

2638 derscores the value of difference-imaging-based catalogs  
 2639 for probing dense stellar regions inaccessible to standard  
 2640 coadd processing in DP1.

2641 Although the DP1 pipeline was not optimized for  
 2642 crowded-field photometry, these early studies of 47 Tuc  
 2643 and Fornax provide critical benchmarks. They highlight  
 2644 both the limitations and opportunities for science with  
 2645 Rubin data in crowded environments, and they inform  
 2646 future pipeline development aimed at robust source re-  
 2647 covery in complex stellar fields.

## 2648 6. RUBIN SCIENCE PLATFORM

2649 The RSP (M. Jurić et al. 2019) is a powerful, cloud-  
 2650 based environment for scientific research and analysis  
 2651 of petascale-scale astronomical survey data. It serves  
 2652 as the primary interface for scientists to access, visual-  
 2653 ize, and conduct next-to-the-data analysis of Rubin and  
 2654 LSST data. The RSP is designed around a “bring the  
 2655 compute to the data” principle, eliminating the need for  
 2656 users to download massive datasets. Although DP1 is  
 2657 much smaller in size (3.5 TB) than many current sur-  
 2658 vey datasets, future LSST datasets will be far larger and  
 2659 more complex, making it crucial to co-locate data and  
 2660 analysis for effective scientific discovery.

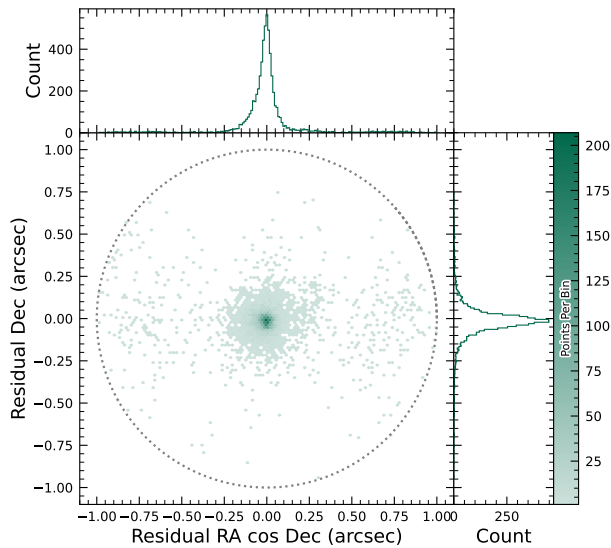


**Figure 39.** Astrometric residuals between expected and observed positions of Solar System Objects in DP1. The median residuals are  $0''.001$  and  $-0''.016$  in R.A./Dec direction, with standard deviations of  $0''.19$  and  $0''.10$ , respectively. No detectable systematic offset from zero indicates there are no major errors in either timing or astrometry delivered by the Rubin system. The wider scatter in the RA direction is due to objects whose measured orbital elements are less well constrained, translating to larger along-track positional errors in the predicted positions.

2661 The RSP provides users with access to data and  
 2662 services through three distinct user-facing Aspects: a  
 2663 *Portal*, which facilitates interactive exploration of the  
 2664 data; a JupyterLab-based *Notebook* environment for  
 2665 data analysis using Python; and an extensive set of  
 2666 *Application Programming Interfaces (APIs)* that enable  
 2667 programmatic access to both data and services. The  
 2668 three Aspects are designed to be fully integrated, en-  
 2669 abling seamless workflows across the RSP. The data  
 2670 products described in §3 are accessible via all three  
 2671 Aspects, and the system facilitates operations such as  
 2672 starting a query in one Aspect and retrieving its results  
 2673 in another. Figure 40 shows the Rubin Science Platform  
 2674 landing page in the Google cloud.

2676 The RSP is supported by a number of back-end ser-  
 2677 vices, including databases, files, and batch comput-  
 2678 ing. Support for collaborative work through shared  
 2679 workspaces is also included in the RSP.

2680 A preview of the RSP was launched on Google Cloud  
 2681 in 2022, operating under a shared-risk model to support  
 2682 Data Preview 0 (W. O’Mullane et al. 2024a). This al-  
 2683 lowed the community to test the platform, begin prepa-

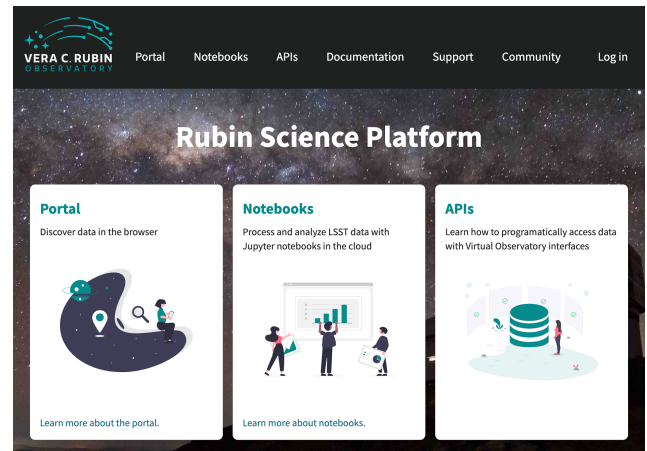


**Figure 40.** The Rubin Science Platform landing page at <https://data.lsst.cloud/> showing the three user-facing Aspects as well as links to documentation and support information.

2684 rations for science, and provide valuable feedback to in-  
 2685 form ongoing development. It was the first time an as-  
 2686 tronomical research environment was hosted in a cloud  
 2687 environment. The DP1 release brings major updates to  
 2688 RSP services, enhancing scientific analysis capabilities.  
 2689 The RSP remains under active development, with incre-  
 2690 mental improvements being rolled out as they mature.  
 2691 During the Rubin Early Science Phase, the RSP will  
 2692 continue to operate under a shared-risk model. This  
 2693 section outlines the RSP functionality available at the  
 2694 time of the DP1 release and provides an overview of  
 2695 planned future capabilities.

### 2696 6.1. Rubin Data Access Center

2697 The Rubin US Data Access Center (US DAC) utilizes  
 2698 a novel hybrid on-premises-cloud architecture, which  
 2699 combines on-premises infrastructure at the USDF at  
 2700 SLAC with flexible and scalable resources in the Google  
 2701 cloud. This architecture has been deployed and tested  
 2702 using the larger simulated data set of DP0.2 (W.  
 2703 O’Mullane et al. 2024b).

2704 In this hybrid model, user-facing services are deployed  
 2705 in the cloud to support dynamic scaling in response to  
 2706 user demand and to simplify the provisioning and man-  
 2707 agement of large numbers of science user accounts. The  
 2708 majority of the static data products described in §3 are  
 2709 stored on-premises at the USDF to benefit from cost-  
 2710 effective mass storage and close integration with Ru-  
 2711 bin data processing infrastructure, also located at the  
 2712 USDF. For imaging data, the Data Butler (§6.2.2) pro-  
 2713 vides the interface between the cloud-based users and  
 2714 data services, and the on-premises data. For catalog  
 2715 data, a cloud-based TAP client (§6.2.1) submits queries  
 2716 to the on-premises Qserv database cluster (§6.5) and re-

trieves the results. In the initial DP1 deployment, catalog data is hosted at the USDF while image data is stored in the cloud. The full hybrid model will be rolled out and further tested following the release of DP1. The RSP features a single-sign-on authentication and authorization system to provide secure access for Rubin data rights holders (R. Blum & the Rubin Operations Team 2020).

## 6.2. API Aspect

The API Aspect provides a comprehensive set of user-facing interfaces for programmatic access to the DP1 data products, through both IVOA-compliant services and the Rubin Data Butler. IVOA services enable standard queries and integration with existing tools, while the Butler facilitates advanced data processing within the LSST Science Pipelines.

At the time of the DP1 release, some IVOA services are unavailable, and certain data products are only accessible via the Butler. This section provides an overview of the available IVOA services and Butler access.

### 6.2.1. IVOA Services

Rubin has adopted a Virtual Observatory (VO)-first design philosophy, prioritizing compliance with IVOA standard interfaces to foster interoperability, standardization, and collaboration. In cases where standardized protocols have yet to be established, additional services have been introduced to complement these efforts. This approach ensures that the RSP can be seamlessly integrated with community-standard tools such as Tool for Operations on Catalogues And Tables (TOPCAT) (M. Taylor 2011) and Aladin (F. Bonnarel et al. 2000; T. Boch & P. Fernique 2014; M. Baumann et al. 2022), as well as libraries such as PyVO (M. Graham et al. 2014).

The user-facing APIs are also used internally within the RSP, creating a unified design that ensures consistent and reproducible workflows across all three Aspects. This reduces code duplication, simplifies maintenance, and ensures all users, both internal and external, access data in the same way. For example, an Astronomical Data Query Language (IVOA standard) (ADQL) query on the Object catalog via TAP yields identical results whether run from the Portal, Notebook, or an external client.

The following IVOA services are available at the time of the DP1 release:

- **Table Access Protocol (TAP) Service:** A TAP service (P. Dowler et al. 2019) enables queries of catalog data via the IVOA-standard ADQL, a

dialect of SQL92 with spherical geometry extensions. The main TAP service for DP1 runs on the Rubin-developed Qserv database (§ 6.5), which hosts the core science tables described in §3.2, as well as the Visit database. It also provides image metadata in the IVOA ObsCore format via the standard `ivoa.ObsCore` table, making it an “ObsTAP” service (ObsTAP; M. Louys et al. 2017). The TAP service is based on the Canadian Astronomy Data Centre (CADC)’s open-source Java TAP implementation<sup>104</sup>, modified for the exact query language accepted by Qserv. It currently supports a large subset of ADQL, with limitations documented in the data release materials (see §7.1) and exposed via the TAP **capabilities** endpoint where possible.

The TAP service provides metadata annotations consistent with the standard, including table and column descriptions, indications of foreign-key relationships between tables, and column metadata such as units and IVOA Unified Content Descriptors (UCDs).

- **Image Access Services:** Rubin image access services are compliant with IVOA SIAv2 (Simple Image Access Protocol, version 2; T. Jenness et al. 2024; P. Dowler et al. 2015) for discovering and accessing astronomical images based on metadata. SIAv2 is a REpresentational State Transfer (REST)-based protocol designed for the discovery and retrieval of image data. It allows, for instance, querying all images in a given band over a defined sky region and time period.

Users identify an image or observation of interest and query the service. The result set includes metadata about the image, such as the sky position, time, or band, and a data access URL, which includes an IVOA Identifier uniquely identifying the dataset (T. Jenness & G. P. Dubois-Felsmann 2025), allowing the dataset to be retrieved or a cutout requested via Server-side Operations for Data Access (IVOA standard) (SODA).

- **Image Cutout Service:** The Rubin Cutout Service (R. Allbery 2023, 2024) is based on the IVOA SODA standard (F. Bonnarel et al. 2017). Users submit requests specifying sky coordinates and the cutout size as the radius from the coordinates, and the service performs the operation on the full im-

<sup>104</sup> <https://github.com/opencadc/tap>

age and returns a result set. For *DP1*, the cutout service is a single cutout service only where  $N$  cutout requests will require  $N$  independent synchronous calls. We expect some form of bulk cutout service by mid 2026.

- **HiPS Data Service:** An authenticated HiPS (P. Fernique et al. 2017) data service for seamless pan-and-zoom access to large-scale co-adds. It supports fast interactive progressive image exploration at a range of resolutions.
- **WebDAV:** A Web Distributed Authoring and Versioning (WebDAV) service is provided to enable users to remotely manage, edit, and organize files and directories on the RSP as if they were local files on their own computer. This is especially useful for local development.

### 6.2.2. Data Butler

The Rubin Data Butler (T. Jenness et al. 2022; N. B. Lust et al. 2023), is a high-level interface designed to facilitate seamless access to data for both users and software systems. This includes managing storage formats, physical locations, data staging, and database mappings. A Butler repository contains two components:

- the *Data Store*: A physical storage system for datasets, e.g., a Portable Operating System Interface (POSIX) file system or S3 object store; and
- the *Registry*: An Structured Query Language (SQL)-compatible database that stores metadata about the datasets in the data store.

For *DP1*, the Butler repository is hosted in the Google Cloud, using an (Amazon) Simple Storage Service (S3)-compatible store for datasets and AlloyDB, a PostgreSQL-compatible database, for the registry.

In the context of the Butler, a *dataset* refers to a unique data product, such as an image, catalog or map, generated by the observatory or processing pipelines. Datasets belong to one of the various types of data products, described in §3. The Butler ensures that each dataset is uniquely identifiable by a combination of three pieces of information: a data coordinate, a dataset type, and a run collection. For example, a dataset that represents a single raw image in the *i* band taken on the night starting 2024-11-11 with exposure ID 2024111100074 would be represented as `dataId='exposure':2024111100074, 'band':'i', 'instrument':'LSSTComCam'` and is associated with the `raw` DatasetType. For a deep coadd on a `patch` of

**Table 6.** Tract coverage of each *DP1* field. The size of a tract is larger than the LSSTComCam field of view; however, since each observed field extends across more than one tract, each field covers multiple tracts.

Field Code	Tract ID
47_Tuc	453, 454
ECDFS	4848, 4849, 5062, 5063, 5064
EDFS_comcam	2234, 2235, 2393, 2394
Fornax_dSph	4016, 4017, 4217, 4218
Rubin_SV_095_-25	5305, 5306, 5525, 5526
Rubin_SV_38_7	10221, 10222, 10463, 10464, 10704, 10705
Seagull	7610, 7611, 7849, 7850

sky in the Seagull field, there would be no exposure dimensions and instead the tract, `patch` and `band` would be specified as `dataId='tract':7850, 'patch':6, 'band':'g', 'instrument':'LSSTComCam', 'skymap='lsst_cells_v1'` and is associated with the `deep_coadd` DatasetType. The tract identification numbers and corresponding target names for these tracts are listed in Table 6.

The data coordinate is used to locate a dataset in multi-dimensional space, where dimensions are defined in terms of scientifically meaningful concepts, such as instrument, visit, detector or band. For example, a calibrated single-visit image (§3.1) has dimensions including band, instrument, and detector. In contrast, the visit table (§3.2), a catalog of all calibrated single-epoch visits in *DP1*, has only the instrument dimension. The main dimensions used in *DP1* are listed, together with a brief description, in Table 7. To determine which dimensions are relevant for a specific dataset, the Butler defines dataset types, which associate each dataset with its specific set of relevant dimensions, as well as the associated Python type representing the dataset. The dataset type defines the kind of data a dataset represents, such as a raw image (`raw`), a processed catalog (`object_forced_source`), or a sky map (`skyMap`). Table 8 lists all the dataset types available via the Butler in *DP1*, together with the dimensions needed to uniquely identify a specific dataset and the number of unique datasets of each type.

It is important to highlight a key difference between accessing catalog data via the TAP service versus the Butler. While the TAP service contains entire catalogs, many of the same catalogs in the Butler are split into multiple separate catalogs. This is partly due to how these catalogs are generated, but also because of the

**Table 7.** Descriptions of and valid values for the key data dimensions in DP1. YYYYMMDD signifies date and # signifies a single 0–9 digit.

Dimension	Format/Valid values	Description
day_obs	YYYYMMDD	A day and night of observations that rolls over during daylight hours.
visit	YYYYMMDD#####	A sequence of observations processed together; synonymous with “exposure” in DP1.
exposure	YYYYMMDD#####	A single exposure of all nine ComCam detectors.
instrument	LSSTComCam	The instrument name.
detector	0–8	A ComCam detector.
skymap	lsst_cells_v1	A set of tracts and patches that subdivide the sky into rectangular regions with simple projections and intentional overlaps.
tract	See Table 6	A large rectangular region of the sky.
patch	0–99	A rectangular region within a tract.
physical_filter	u_02, g_01, i_06, r_03, z_03, y_04	A physical filter.
band	u, g, r, i, z, y	An conceptual astronomical passband.

way data is stored within and retrieved from the Butler repository – it is inefficient to retrieve the entire `Source` catalog, for example, from the file system. Instead, because the `Source` catalog contains data for sources detected in the `visit_images`, there is one `Source` catalog in the Butler for each `visit_image`. Similarly, there is one `Object` catalog for each `deep_coadd`. All the catalogs described in §3.2, aside from the `CcdVisit`, `SSObject`, `SSSource`, and `Calibration` catalogs, are split within the Butler.

A dataset is associated with one or more *Collections*; logical groupings of datasets within the Butler system that were created or processed together by the same batch operation. Collections allow multiple datasets with the same data coordinate to coexist without conflict. Collections support flexible, parallel processing by enabling repeated analyses of the same input data using different configurations. The DP1 Butler is read-only; a writeable Butler is expected by mid-2026.

### 6.2.3. Remote Programmatic Access

The Rubin RSP API can be accessed from a local system by data rights holders outside of the RSP, by creating a user security token. This token can then be used as a bearer token for API calls to the RSP TAP service. This capability is especially useful for remote data analysis using tools such as TOPCAT, as well as enabling third-party systems, e.g., Community Alert Brokers, to access Rubin data. Additionally, it supports remote development, allowing for more flexible workflows and integration with external systems.

### 6.3. Portal Aspect

The Portal Aspect provides an interactive web-based environment for exploratory data discovery, filtering, querying, and visualization of both image and catalog data, without requiring programming expertise. It enables users to access and analyze large datasets via tools for catalog queries, image browsing, time-series inspection, and cross-matching.

The Portal is built on Firefly (X. Wu et al. 2019), a web application framework developed by the Infrared Processing and Analysis Center (IPAC). Firefly provides interactive capabilities such as customizable table views, image overlays, multi-panel visualizations, and synchronized displays linking catalog and image data.

Designed to support both exploratory data access and detailed scientific investigation, the Portal delivers an intuitive user experience, allowing users to visually analyze data while retaining access to underlying metadata and query controls.

### 6.4. Notebook Aspect

The Notebook Aspect provides an interactive, web-based environment built on Jupyter Notebooks, enabling users to write and execute Python code directly on Rubin and LSST data without downloading it locally. It offers programmatic access to Rubin and LSST data products, allowing users to query and retrieve datasets, manipulate and display images, compute derived properties, plot results, and reprocess data using the LSST Science Pipelines (§4.1). The environment comes pre-installed with the pipelines and a broad set of widely used astronomical software tools, supporting immediate and flexible data analysis.

**Table 8.** The name and number of each type of data product in the Butler and the dimensions required to identify a specific dataset.

Data Product	Name in Butler	Required Dimensions	Number in DP1
<b>Image Data Products</b>			
raw	raw	instrument, detector, exposure	16125
visit_image	visit_image	instrument, detector, visit	15972
deep_coadd	deep_coadd	band, skymap, tract, patch	2644
template_coadd	template_coadd	band, skymap, tract, patch	2730
difference_image	difference_image	instrument, detector, visit	15972
<b>Catalog Data Products</b>			
Source	source	instrument, visit	1786
Object	object	skymap, tract	29
ForcedSource	object_forced_source	skymap, tract, patch	636
DiaSource	dia_source	skymap, tract	25
DiaObject	dia_object	skymap, tract	25
ForcedSourceOnDiaObject	dia_object_forced_source	skymap, tract, patch	597
SSSource	ss_source	–	1
SSObject	ss_object	–	1
Visit	visit_table	instrument	1
CCDVisit	visit_detector_table	instrument	1

## 6.5. Databases

The user-facing Aspects of the RSP are supported by several backend databases that store catalog data products, image metadata, and other derived datasets. The schema for DP1 and other Rubin databases are available online at <https://sdm-schemas.lsst.io>.

### 6.5.1. Qserv

The final 10-year LSST catalog is expected to reach 15 PB and contain measurements for billions of stars and galaxies across trillions of detections. To support efficient storage, querying, and analysis of this dataset, Rubin Observatory developed Qserv (D. L. Wang et al. 2011; F. Mueller et al. 2023) – a scalable, parallel, distributed SQL database system. Qserv partitions data over approximately equal-area regions of the celestial sphere, replicates data to ensure resilience and high availability, and uses shared scanning to reduce overall I/O load. It also supports a package of scientific user-defined functions (SciSQL: <https://smonkewitz.github.io/scisql/>) simplifying complex queries involving spherical geometry, statistics, and photometry. Qserv is built on robust production-quality components, including MariaDB (<https://www.mariadb.org/>) and XRootD (<https://xrootd.org/>). Qserv runs at the USDF and user access to catalog data is via the TAP service (§6.2.1). This enables catalog-based analysis through both the RSP Portal and Notebook Aspects.

Although the small DP1 dataset does not require Qserv’s full capabilities, we nevertheless chose to use it for DP1 to accurately reflect the future data access environment and to gain experience with scientifically-motivated queries ahead of full-scale deployment. Qserv is open-source and available on GitHub: <https://github.com/lsst/qserv>.

## 7. SUPPORT FOR COMMUNITY SCIENCE

The Rubin Observatory has a science community that encompasses thousands of individuals worldwide, with a broad range of experience and expertise in astronomy in general, and in the analysis of optical imaging data specifically.

Rubin’s model to support this diverse community to access and analyze DP1 emphasizes self-help via documentation and tutorials, and employs an open platform for asynchronous issue reporting that enables crowd-sourced solutions. These two aspects of community support are augmented by virtual engagement activities. In addition, Rubin supports its Users Committee to advocate on behalf of the science community, and supports the eight LSST Science Collaborations (§7.6).

All of the resources for scientists that are discussed in this section are discoverable by browsing the For Scientists pages of the Rubin Observatory website<sup>105</sup>.

### 7.1. Documentation

The data release documentation for DP1<sup>106</sup> provides an overview of the LSSTComCam observations, detailed descriptions of the data products, and a high-level summary of the processing pipelines. Although much of its content overlaps significantly with this paper, the documentation is presented as a searchable, web-based resource built using Sphinx<sup>107</sup>, with a focus on enabling scientific use of the data products.

### 7.2. Tutorials

A suite of tutorials (NSF-DOE Vera C. Rubin Observatory 2021) that demonstrate how to access and analyze DP1 using the RSP accompanies the DP1 release<sup>108</sup>. Jupyter Notebook tutorials are available via the “Tutorials” drop-down menu within the Notebook aspect of the RSP. Tutorials for the Portal and API aspects of the RSP can be found in the data release documentation.

These tutorials are designed to be inclusive, accessible, clear, focused, and consistent. Their format and contents follow a set of guidelines (M. L. Graham et al. 2026) that are informed by modern standards in technical writing.

### 7.3. Community Forum

The venue for all user support is the Rubin Community Forum<sup>109</sup>.

Questions about any and all aspects of the Rubin data products, pipelines, and services – including DP1 – should be posted as new topics in the Support category. This includes beginner-level and “how-to” questions, advanced scientific analysis questions, technical bug reports, account and data access issues, and everything in between. The Support category of the Forum is monitored by Rubin staff, who follow an established internal workflow for following-up and resolving all reported issues.

The Rubin Community Forum is built on the open-source Discourse platform. It was chosen because, for a worldwide community of ten thousand Rubin users, a traditional (i.e., closed) help desk represents a risk to

Rubin science (e.g., many users with the same question having to wait for responses). The open nature of the Forum enables self-help by letting users search for similar issues, and enables crowd-sourced problem solving (and avoids knowledge bottlenecks) by letting users help users.

The Rubin Community Forum, and the internal staff workflows for user support, were set up, tested, and refined with /glsDP0 so that it was ready for use with DP1.

### 7.4. Engagement Activities

A variety of live virtual and in-person workshops and seminars offer learning opportunities to scientists and students working with the Rubin data products, services, and tools.

- Rubin Science Assemblies (weekly, virtual, 1 hour): alternates between hands-on tutorials based on the most recent data release and open drop-in “office hours” with Rubin staff.
- Rubin Data Academy (annual, virtual, 3-4 days): an intense set of hands-on tutorials based on the most recent data release, along with co-working and networking sessions.
- Rubin Community Workshop (annual, virtual, 5 days), a science-focused conference of contributed posters, talks, and sessions led by members of the Rubin science community and Rubin staff.

Following the release of DP1, all of these engagement activities focused on use of DP1 by the science community. In particular, the 2025 Rubin Data Academy was run the week of the DP1 release, in order to immediately facilitate community access. The 2025 Rubin Community Workshop had several sessions to introduce people to the DP1 dataset and demonstrate how to access and analyze it with the RSP.

For schedules, connection information, zoom recordings, and associated materials, visit the For Scientists pages of the Rubin Observatory website<sup>110</sup>. Requests for custom tutorials and presentations for research groups are also accommodated.

### 7.5. Users Committee

This committee is charged with soliciting feedback from the science community, advocating on their behalf, and recommending science-driven improvements to the LSST data products and the Rubin Science Platform

<sup>105</sup> <https://rubinobservatory.org/for-scientists>

<sup>106</sup> <https://dp1.lsst.io>

<sup>107</sup> <https://www.sphinx-doc.org/>

<sup>108</sup> <https://dp1.lsst.io/tutorials>

<sup>109</sup> <https://community.lsst.org/>

<sup>110</sup> <https://rubinobservatory.org/for-scientists/events-deadlines>

tools and services. Community members are encouraged to attend their virtual meetings and raise issues to their attention, so they can be included in the committee’s twice-yearly reports to the Rubin Observatory Director.

Like the Forum, the Users Committee was established and began its work with DP0, and that feedback was implemented for DP1. The community’s response to DP1 will be especially valuable input to DP2 and DR1, and the Users Committee encourages all users to interact with them. For a list of members and contact information, visit the For Scientists pages of the Rubin Observatory website.

### 7.6. Science Collaborations

The eight LSST Science Collaborations are independent, worldwide communities of scientists, self-organized into collaborations based on their research interests and expertise. Members work together to apply for funding, build software infrastructure and analysis algorithms, and incorporate external data sets into their LSST-based research.

The Science Collaborations also provide valuable advice to Rubin Observatory on the operational strategies and data products to accomplish specific science goals, and Rubin Observatory supports the collaborations via staff liaisons and regular virtual meetings with Rubin operations leadership.

The Science Collaborations have been functioning for many years, and their engagement and feedback on DP0 was implemented into the community science model for DP1, as it will for future data releases.

## 8. SUMMARY AND FUTURE RELEASES

Rubin Data Preview 1 offers an initial look at the first on-sky data products and access services from the Vera C. Rubin Observatory. DP1 forms part of Rubin’s Early Science Program, and provides the scientific community with an early opportunity to familiarize themselves with the data formats and access infrastructure for the forthcoming Legacy Survey of Space and Time. This early release has a proprietary period of two years, during which time it is available to Rubin data rights holders only via the cloud-based RSP.

In this paper we have described the completion status of the observatory at the time of data acquisition, the commissioning campaign that forms the basis of DP1, and the processing pipelines used to produce early versions of data products. We provide details on the data products, their characteristics and known issues, and describe the Rubin Science Platform for access to and analysis of DP1.

The data products described in this paper derive from observations obtained by LSSTComCam. LSSTComCam contains only around 5% the number of CCDs as the full LSST Science Camera (LSSTCam), yet the DP1 dataset that it has produced will already enable a very broad range of science. At 3.5 TB in size, DP1 covers a total area of  $\sim 15 \text{ deg}^2$  and contains 1792 single-epoch images, 2644 deep coadded images and 2.3 million distinct astrophysical objects, including 93 new asteroid discoveries.

While some data products anticipated from the LSST are not yet available, e.g., cell-based coadds, DP1 includes several products that will not be provided in future releases. Notably, difference images are included in DP1 as pre-generated products; in future releases, these will instead be generated on demand via dedicated services. The inclusion of pre-generated difference images in DP1 is feasible due to the relatively small size of the dataset, an approach that will not scale to the significantly larger data volumes expected in subsequent releases.

The RSP is continually under development, and new functionality will continue to be deployed incrementally as it becomes available, and independent of the future data release schedule. User query history capabilities, context-aware documentation and a bulk cutout services are just a few of the services currently under development.

Coincident with the release of DP1, Rubin Observatory begins its Science Validation Surveys with the LSST Science Camera. This final commissioning phase will produce a dataset that will form the foundation for the second Rubin Data Preview, DP2. Full operations, marking the start of the LSST, are expected to commence in 2026.

## ACKNOWLEDGMENTS

. This material is based upon work supported in part by the National Science Foundation through Cooperative Agreements AST-1258333 and AST-2241526 and Cooperative Support Agreements AST-1202910 and AST-2211468 managed by the Association of Universities for Research in Astronomy (AURA), and the Department of Energy under Contract No. DE-AC02-76SF00515 with the SLAC National Accelerator Laboratory managed by Stanford University. Additional Rubin Observatory funding comes from private donations, grants to universities, and in-kind support from LSST-DA Institutional Members.

This work has been supported by the French National Institute of Nuclear and Particle Physics (IN2P3)

3196 through dedicated funding provided by the National  
3197 Center for Scientific Research (CNRS).

3198 This work has been supported by STFC fund-  
3199 ing for UK participation in LSST, through grant  
3200 ST/Y00292X/1.

3201 *Facilities:* Rubin:Simonyi (LSSTComCam), Ru-  
3202 bin:USDAC

3203 *Software:* Rubin Data Butler (T. Jenness et al.  
3204 2022), LSST Science Pipelines (Rubin Observatory Sci-  
3205 ence Pipelines Developers 2025), LSST Feature Based  
3206 Scheduler v3.0 (P. Yoachim et al. 2024; E. Naghib et al.  
3207 2019) Astropy (Astropy Collaboration et al. 2013, 2018,  
3208 2022) PIFF (M. Jarvis et al. 2021), GBDES (G. M.  
3209 Bernstein 2022), Qserv (D. L. Wang et al. 2011; F.  
3210 Mueller et al. 2023), Slurm, HTCondor, CVMFS, FTS3,  
3211 ESNNet

3212

## APPENDIX

## REFERENCES

- 3213 Abazajian, K., Adelman-McCarthy, J. K., Agüeros, M. A.,  
3214 et al. 2004, *AJ*, 128, 502, doi: [10.1086/421365](https://doi.org/10.1086/421365)
- 3215 Ahumada, R., Allende Prieto, C., Almeida, A., et al. 2020,  
3216 *ApJS*, 249, 3, doi: [10.3847/1538-4365/ab929e](https://doi.org/10.3847/1538-4365/ab929e)
- 3217 Aihara, H., AlSayyad, Y., Ando, M., et al. 2022, *PASJ*, 74,  
3218 247, doi: [10.1093/pasj/psab122](https://doi.org/10.1093/pasj/psab122)
- 3219 Allbery, R. 2023, IVOA SODA implementation experience,  
3220 SQuaRE Technical Note SQR-063, NSF-DOE Vera C.  
3221 Rubin Observatory. <https://sqr-063.lsst.io/>
- 3222 Allbery, R. 2024, Draft IVOA SODA web service  
3223 specification, SQuaRE Technical Note SQR-093,  
3224 NSF-DOE Vera C. Rubin Observatory.  
3225 <https://sqr-093.lsst.io/>
- 3226 AlSayyad, Y. 2018, Coaddition Artifact Rejection and  
3227 CompareWarp, Data Management Technical Note  
3228 DMTN-080, NSF-DOE Vera C. Rubin Observatory,  
3229 doi: [10.71929/rubin/2583441](https://doi.org/10.71929/rubin/2583441)
- 3230 Ansel, J., Yang, E., He, H., et al. 2024, in 29th ACM  
3231 International Conference on Architectural Support for  
3232 Programming Languages and Operating Systems, Volume  
3233 2 (ASPLOS '24) (ACM), doi: [10.1145/3620665.3640366](https://doi.org/10.1145/3620665.3640366)
- 3234 Antilogus, P., Astier, P., Doherty, P., Guyonnet, A., &  
3235 Regnault, N. 2014, *Journal of Instrumentation*, 9,  
3236 C03048, doi: [10.1088/1748-0221/9/03/C03048](https://doi.org/10.1088/1748-0221/9/03/C03048)
- 3237 Astropy Collaboration, Robitaille, T. P., Tollerud, E. J.,  
3238 et al. 2013, *A&A*, 558, A33,  
3239 doi: [10.1051/0004-6361/201322068](https://doi.org/10.1051/0004-6361/201322068)
- 3240 Astropy Collaboration, Price-Whelan, A. M., Sipőcz, B. M.,  
3241 et al. 2018, *AJ*, 156, 123, doi: [10.3847/1538-3881/aabc4f](https://doi.org/10.3847/1538-3881/aabc4f)
- 3242 Astropy Collaboration, Price-Whelan, A. M., Lim, P. L.,  
3243 et al. 2022, *ApJ*, 935, 167, doi: [10.3847/1538-4357/ac7c74](https://doi.org/10.3847/1538-4357/ac7c74)
- 3244 Baumann, M., Boch, T., Pineau, F.-X., et al. 2022, in  
3245 *Astronomical Society of the Pacific Conference Series*,  
3246 Vol. 532, *Astronomical Data Analysis Software and*  
3247 *Systems XXX*, ed. J. E. Ruiz, F. Pierfedereci, &  
3248 P. Teuben, 7
- 3249 Bechtol, K., Sevilla-Noarbe, I., Drlica-Wagner, A., et al.  
3250 2025, arXiv e-prints, arXiv:2501.05739,  
3251 doi: [10.48550/arXiv.2501.05739](https://doi.org/10.48550/arXiv.2501.05739)
- 3252 Berk, A., Anderson, G. P., Bernstein, L. S., et al. 1999, in  
3253 *Society of Photo-Optical Instrumentation Engineers*  
3254 *(SPIE) Conference Series*, Vol. 3756, *Optical*  
3255 *Spectroscopic Techniques and Instrumentation for*  
3256 *Atmospheric and Space Research III*, ed. A. M. Larar,  
3257 348–353, doi: [10.1117/12.366388](https://doi.org/10.1117/12.366388)
- 3258 Bernstein, G. M. 2022, gbdes: DECam instrumental  
3259 signature fitting and processing programs,, *Astrophysics*  
3260 *Source Code Library*, record ascl:2210.011  
3261 <http://ascl.net/2210.011>
- 3262 Bernstein, G. M., & Jarvis, M. 2002, *AJ*, 123, 583,  
3263 doi: [10.1086/338085](https://doi.org/10.1086/338085)
- 3264 Bernstein, G. M., Armstrong, R., Plazas, A. A., et al. 2017,  
3265 *PASP*, 129, 074503, doi: [10.1088/1538-3873/aa6c55](https://doi.org/10.1088/1538-3873/aa6c55)
- 3266 Bertin, E. 2011, in *Astronomical Society of the Pacific*  
3267 *Conference Series*, Vol. 442, *Astronomical Data Analysis*  
3268 *Software and Systems XX*, ed. I. N. Evans,  
3269 A. Accomazzi, D. J. Mink, & A. H. Rots, 435
- 3270 Bianco, F. B., Ivezić, Ž., Jones, R. L., et al. 2022, *ApJS*,  
3271 258, 1, doi: [10.3847/1538-4365/ac3e72](https://doi.org/10.3847/1538-4365/ac3e72)
- 3272 Blum, R., & the Rubin Operations Team. 2020, Vera C.  
3273 Rubin Observatory Data Policy, Data Management  
3274 Operations Controlled Document RDO-013, NSF-DOE  
3275 Vera C. Rubin Observatory. <https://ls.st/RDO-013>

- 3276 Boch, T., & Fernique, P. 2014, in *Astronomical Society of*  
 3277 *the Pacific Conference Series*, Vol. 485, *Astronomical*  
 3278 *Data Analysis Software and Systems XXIII*, ed.  
 3279 N. Manset & P. Forshay, 277
- 3280 Bonnarel, F., Dowler, P., Demleitner, M., Tody, D., &  
 3281 Dempsey, J. 2017, *IVOA Server-side Operations for Data*  
 3282 *Access Version 1.0*, *IVOA Recommendation 17 May 2017*  
 3283 doi: [10.5479/ADS/bib/2017ivoa.spec.0517B](https://doi.org/10.5479/ADS/bib/2017ivoa.spec.0517B)
- 3284 Bonnarel, F., Fernique, P., Bienaymé, O., et al. 2000,  
 3285 *A&AS*, 143, 33, doi: [10.1051/aas:2000331](https://doi.org/10.1051/aas:2000331)
- 3286 Bosch, J., Armstrong, R., Bickerton, S., et al. 2018, *PASJ*,  
 3287 70, S5, doi: [10.1093/pasj/psx080](https://doi.org/10.1093/pasj/psx080)
- 3288 Broughton, A., Utsumi, Y., Plazas Malagón, A. A., et al.  
 3289 2024, *PASP*, 136, 045003, doi: [10.1088/1538-3873/ad3aa2](https://doi.org/10.1088/1538-3873/ad3aa2)
- 3290 Burke, D. L., Rykoff, E. S., Allam, S., et al. 2018, *AJ*, 155,  
 3291 41, doi: [10.3847/1538-3881/aa9f22](https://doi.org/10.3847/1538-3881/aa9f22)
- 3292 Chambers, K. C., Magnier, E. A., Metcalfe, N., et al. 2016,  
 3293 *arXiv e-prints*, arXiv:1612.05560,  
 3294 doi: [10.48550/arXiv.1612.05560](https://doi.org/10.48550/arXiv.1612.05560)
- 3295 Choi, Y., Olsen, K. A. G., Carlin, J. L., et al. 2025, *arXiv*  
 3296 *e-prints*, arXiv:2507.01343,  
 3297 doi: [10.48550/arXiv.2507.01343](https://doi.org/10.48550/arXiv.2507.01343)
- 3298 de Vaucouleurs, G. 1948, *Annales d'Astrophysique*, 11, 247
- 3299 de Vaucouleurs, G. 1953, *MNRAS*, 113, 134,  
 3300 doi: [10.1093/mnras/113.2.134](https://doi.org/10.1093/mnras/113.2.134)
- 3301 Dowler, P., Bonnarel, F., & Tody, D. 2015, *IVOA Simple*  
 3302 *Image Access Version 2.0*, *IVOA Recommendation 23*  
 3303 *December 2015*  
 3304 doi: [10.5479/ADS/bib/2015ivoa.spec.1223D](https://doi.org/10.5479/ADS/bib/2015ivoa.spec.1223D)
- 3305 Dowler, P., Rixon, G., Tody, D., & Demleitner, M. 2019,  
 3306 *Table Access Protocol Version 1.1*, *IVOA*  
 3307 *Recommendation 27 September 2019*  
 3308 doi: [10.5479/ADS/bib/2019ivoa.spec.0927D](https://doi.org/10.5479/ADS/bib/2019ivoa.spec.0927D)
- 3309 Eggl, S., Juric, M., Moeyens, J., & Jones, L. 2020, in  
 3310 *AAS/Division for Planetary Sciences Meeting Abstracts*,  
 3311 *Vol. 52*, *AAS/Division for Planetary Sciences Meeting*  
 3312 *Abstracts*, 211.01
- 3313 Esteves, J. H., Utsumi, Y., Snyder, A., et al. 2023, *PASP*,  
 3314 135, 115003, doi: [10.1088/1538-3873/ad0a73](https://doi.org/10.1088/1538-3873/ad0a73)
- 3315 Euclid Collaboration, Romelli, E., Kümmel, M., et al. 2025,  
 3316 *arXiv e-prints*, arXiv:2503.15305,  
 3317 doi: [10.48550/arXiv.2503.15305](https://doi.org/10.48550/arXiv.2503.15305)
- 3318 Fagrelis, P., & Rykoff, E. S. 2025, *Rubin Observatory*  
 3319 *Baseline Calibration Plan*, *Commissioning Technical*  
 3320 *Note SITCOMTN-086*, *NSF-DOE Vera C. Rubin*  
 3321 *Observatory*, doi: [10.71929/rubin/2583850](https://doi.org/10.71929/rubin/2583850)
- 3322 Ferguson, P. S., Rykoff, E. S., Carlin, J. L., Saunders, C., &  
 3323 Parejko, J. K. 2025, *The Monster: A reference catalog*  
 3324 *with synthetic ugrizy-band fluxes for the Vera C. Rubin*  
 3325 *observatory*, *Data Management Technical Note*  
 3326 *DMTN-277*, *NSF-DOE Vera C. Rubin Observatory*,  
 3327 doi: [10.71929/rubin/2583688](https://doi.org/10.71929/rubin/2583688)
- 3328 Fernique, P., Allen, M. G., Boch, T., et al. 2015, *A&A*, 578,  
 3329 A114, doi: [10.1051/0004-6361/201526075](https://doi.org/10.1051/0004-6361/201526075)
- 3330 Fernique, P., Allen, M., Boch, T., et al. 2017, *HiPS -*  
 3331 *Hierarchical Progressive Survey Version 1.0*, *IVOA*  
 3332 *Recommendation 19 May 2017*  
 3333 doi: [10.5479/ADS/bib/2017ivoa.spec.0519F](https://doi.org/10.5479/ADS/bib/2017ivoa.spec.0519F)
- 3334 Fortino, W. F., Bernstein, G. M., Bernardinelli, P. H., et al.  
 3335 2021, *AJ*, 162, 106, doi: [10.3847/1538-3881/ac0722](https://doi.org/10.3847/1538-3881/ac0722)
- 3336 Gaia Collaboration, Montegriffo, P., Bellazzini, M., et al.  
 3337 2023a, *A&A*, 674, A33,  
 3338 doi: [10.1051/0004-6361/202243709](https://doi.org/10.1051/0004-6361/202243709)
- 3339 Gaia Collaboration, Vallenari, A., Brown, A. G. A., et al.  
 3340 2023b, *A&A*, 674, A1, doi: [10.1051/0004-6361/202243940](https://doi.org/10.1051/0004-6361/202243940)
- 3341 Górski, K. M., Hivon, E., Banday, A. J., et al. 2005, *ApJ*,  
 3342 622, 759, doi: [10.1086/427976](https://doi.org/10.1086/427976)
- 3343 Graham, A. W., & Driver, S. P. 2005, *PASA*, 22, 118,  
 3344 doi: [10.1071/AS05001](https://doi.org/10.1071/AS05001)
- 3345 Graham, M., Plante, R., Tody, D., & Fitzpatrick, M. 2014,  
 3346 *PyVO: Python access to the Virtual Observatory*,,  
 3347 *Astrophysics Source Code Library*, record ascl:1402.004
- 3348 Graham, M. L., Carlin, J. L., Adair, C. L., et al. 2026,  
 3349 *Guidelines for User Tutorials*, *Technical Note RTN-045*,  
 3350 *NSF-DOE Vera C. Rubin Observatory*,  
 3351 doi: [10.71929/rubin/2584020](https://doi.org/10.71929/rubin/2584020)
- 3352 Gray, B. 2025, *find\_orb: Orbit determination from*  
 3353 *observations*, [https://github.com/Bill-Gray/find\\_orb](https://github.com/Bill-Gray/find_orb)
- 3354 Guy, L. P., Bechtol, K., Bellm, E., et al. 2026, *Rubin*  
 3355 *Observatory Plans for an Early Science Program*,  
 3356 *Technical Note RTN-011*, *NSF-DOE Vera C. Rubin*  
 3357 *Observatory*, doi: [10.71929/rubin/2584021](https://doi.org/10.71929/rubin/2584021)
- 3358 Heinze, A., Eggl, S., Juric, M., et al. 2022, in *AAS/Division*  
 3359 *for Planetary Sciences Meeting Abstracts*, *Vol. 54*,  
 3360 *AAS/Division for Planetary Sciences Meeting Abstracts*,  
 3361 504.04
- 3362 Heinze, A., Juric, M., & Kurlander, J. 2023, *heliolinx: Open*  
 3363 *Source Solar System Discovery Software*,  
 3364 <https://github.com/heliolinx/heliolinx>
- 3365 Hirata, C., & Seljak, U. 2003, *MNRAS*, 343, 459,  
 3366 doi: [10.1046/j.1365-8711.2003.06683.x](https://doi.org/10.1046/j.1365-8711.2003.06683.x)
- 3367 Holman, M. J., Payne, M. J., Blankley, P., Janssen, R., &  
 3368 Kuindersma, S. 2018, *AJ*, 156, 135,  
 3369 doi: [10.3847/1538-3881/aad69a](https://doi.org/10.3847/1538-3881/aad69a)

- 3370 Howard, J., Reil, K., Claver, C., et al. 2018, in Society of  
 3371 Photo-Optical Instrumentation Engineers (SPIE)  
 3372 Conference Series, Vol. 10700, Ground-based and  
 3373 Airborne Telescopes VII, ed. H. K. Marshall &  
 3374 J. Spyromilio, 107003D, doi: [10.1117/12.2312684](https://doi.org/10.1117/12.2312684)
- 3375 Illingworth, G., Magee, D., Bouwens, R., et al. 2016, arXiv  
 3376 e-prints, arXiv:1606.00841,  
 3377 doi: [10.48550/arXiv.1606.00841](https://doi.org/10.48550/arXiv.1606.00841)
- 3378 Ingraham, P., Fagrelus, P., Stubbs, C. W., et al. 2022, in  
 3379 Society of Photo-Optical Instrumentation Engineers  
 3380 (SPIE) Conference Series, Vol. 12182, Ground-based and  
 3381 Airborne Telescopes IX, ed. H. K. Marshall,  
 3382 J. Spyromilio, & T. Usuda, 121820R,  
 3383 doi: [10.1117/12.2630185](https://doi.org/10.1117/12.2630185)
- 3384 Ivezić, Ž., Kahn, S. M., Tyson, J. A., et al. 2019a, ApJ,  
 3385 873, 111, doi: [10.3847/1538-4357/ab042c](https://doi.org/10.3847/1538-4357/ab042c)
- 3386 Ivezić, Ž., Kahn, S. M., Tyson, J. A., et al. 2019b, ApJ,  
 3387 873, 111, doi: [10.3847/1538-4357/ab042c](https://doi.org/10.3847/1538-4357/ab042c)
- 3388 Jarvis, M., et al. 2021, Mon. Not. Roy. Astron. Soc., 501,  
 3389 1282, doi: [10.1093/mnras/staa3679](https://doi.org/10.1093/mnras/staa3679)
- 3390 Jenness, T., & Dubois-Felsmann, G. P. 2025, IVOA  
 3391 Identifier Usage at the Rubin Observatory, Data  
 3392 Management Technical Note DMTN-302, NSF-DOE Vera  
 3393 C. Rubin Observatory, doi: [10.71929/rubin/2583848](https://doi.org/10.71929/rubin/2583848)
- 3394 Jenness, T., Voutsinas, S., Dubois-Felsmann, G. P., &  
 3395 Salnikov, A. 2024, arXiv e-prints, arXiv:2501.00544,  
 3396 doi: [10.48550/arXiv.2501.00544](https://doi.org/10.48550/arXiv.2501.00544)
- 3397 Jenness, T., Bosch, J. F., Salnikov, A., et al. 2022, in  
 3398 Society of Photo-Optical Instrumentation Engineers  
 3399 (SPIE) Conference Series, Vol. 12189, Software and  
 3400 Cyberinfrastructure for Astronomy VII, 1218911,  
 3401 doi: [10.1117/12.2629569](https://doi.org/10.1117/12.2629569)
- 3402 Jones, R. L., Yoachim, P., Ivezić, Ž., Neilsen Jr., E. H., &  
 3403 Ribeiro, T. 2021, Survey Strategy and Cadence Choices  
 3404 for the Vera C. Rubin Observatory Legacy Survey of  
 3405 Space and Time (LSST), Project Science Technical Note  
 3406 PSTN-051, NSF-DOE Vera C. Rubin Observatory,  
 3407 doi: [10.71929/rubin/2584084](https://doi.org/10.71929/rubin/2584084)
- 3408 Juric, M. 2025, mpsky: Multi-purpose sky catalog  
 3409 cross-matching, <https://github.com/mjuric/mpsky>
- 3410 Jurić, M., Ciardi, D., Dubois-Felsmann, G., & Guy, L.  
 3411 2019, LSST Science Platform Vision Document, Systems  
 3412 Engineering Controlled Document LSE-319, NSF-DOE  
 3413 Vera C. Rubin Observatory, doi: [10.71929/rubin/2587242](https://doi.org/10.71929/rubin/2587242)
- 3414 Jurić, M., Axelrod, T. S., Becker, A. C., et al. 2023, Data  
 3415 Products Definition Document, Systems Engineering  
 3416 Controlled Document LSE-163, NSF-DOE Vera C. Rubin  
 3417 Observatory, doi: [10.71929/rubin/2587118](https://doi.org/10.71929/rubin/2587118)
- 3418 Kannawadi, A. 2025, Consistent galaxy colors with  
 3419 Gaussian-Aperture and PSF photometry, Data  
 3420 Management Technical Note DMTN-190, NSF-DOE Vera  
 3421 C. Rubin Observatory, doi: [10.71929/rubin/2583849](https://doi.org/10.71929/rubin/2583849)
- 3422 Kron, R. G. 1980, ApJS, 43, 305, doi: [10.1086/190669](https://doi.org/10.1086/190669)
- 3423 Kuijken, K. 2008, A&A, 482, 1053,  
 3424 doi: [10.1051/0004-6361:20066601](https://doi.org/10.1051/0004-6361:20066601)
- 3425 Lange, T., Nordby, M., Pollek, H., et al. 2024, in Society of  
 3426 Photo-Optical Instrumentation Engineers (SPIE)  
 3427 Conference Series, Vol. 13096, Ground-based and  
 3428 Airborne Instrumentation for Astronomy X, ed. J. J.  
 3429 Bryant, K. Motohara, & J. R. D. Vernet, 130961O,  
 3430 doi: [10.1117/12.3019302](https://doi.org/10.1117/12.3019302)
- 3431 Léget, P. F., Astier, P., Regnault, N., et al. 2021, A&A,  
 3432 650, A81, doi: [10.1051/0004-6361/202140463](https://doi.org/10.1051/0004-6361/202140463)
- 3433 Lim, K.-T. 2023, Proposal and Prototype for Prompt  
 3434 Processing, Data Management Technical Note  
 3435 DMTN-219, NSF-DOE Vera C. Rubin Observatory,  
 3436 doi: [10.71929/rubin/2585429](https://doi.org/10.71929/rubin/2585429)
- 3437 Louys, M., Tody, D., Dowler, P., et al. 2017, Observation  
 3438 Data Model Core Components, its Implementation in the  
 3439 Table Access Protocol Version 1.1., IVOA  
 3440 Recommendation 09 May 2017  
 3441 doi: [10.5479/ADS/bib/2017ivoa.spec.0509L](https://doi.org/10.5479/ADS/bib/2017ivoa.spec.0509L)
- 3442 LSST Dark Energy Science Collaboration (LSST DESC),  
 3443 Abolfathi, B., Alonso, D., et al. 2021, ApJS, 253, 31,  
 3444 doi: [10.3847/1538-4365/abd62c](https://doi.org/10.3847/1538-4365/abd62c)
- 3445 Lupton, R., Blanton, M. R., Fekete, G., et al. 2004, PASP,  
 3446 116, 133, doi: [10.1086/382245](https://doi.org/10.1086/382245)
- 3447 Lust, N. B., Jenness, T., Bosch, J. F., et al. 2023, arXiv  
 3448 e-prints, arXiv:2303.03313,  
 3449 doi: [10.48550/arXiv.2303.03313](https://doi.org/10.48550/arXiv.2303.03313)
- 3450 Mandelbaum, R., Hirata, C. M., Seljak, U., et al. 2005,  
 3451 MNRAS, 361, 1287,  
 3452 doi: [10.1111/j.1365-2966.2005.09282.x](https://doi.org/10.1111/j.1365-2966.2005.09282.x)
- 3453 Megias Homar, G., Kahn, S. M., Meyers, J. M., Crenshaw,  
 3454 J. F., & Thomas, S. J. 2024, The Astrophysical Journal,  
 3455 974, 108, doi: [10.3847/1538-4357/ad6cdc](https://doi.org/10.3847/1538-4357/ad6cdc)
- 3456 Megias Homar, G., Tighe, R., Thomas, S., et al. 2024, in  
 3457 Ground-based and Airborne Telescopes X, ed. H. K.  
 3458 Marshall, J. Spyromilio, & T. Usuda, Vol. 13094,  
 3459 International Society for Optics and Photonics (SPIE),  
 3460 130943C, doi: [10.1117/12.3019031](https://doi.org/10.1117/12.3019031)
- 3461 Melchior, P., Moolekamp, F., Jerdee, M., et al. 2018,  
 3462 Astronomy and Computing, 24, 129,  
 3463 doi: [10.1016/j.ascom.2018.07.001](https://doi.org/10.1016/j.ascom.2018.07.001)
- 3464 Mueller, F., et al. 2023, in ASP Conf. Ser., Vol. TBD,  
 3465 ADASS XXXII, ed. S. Gaudet, S. Gwyn, P. Dowler,  
 3466 D. Bohlender, & A. Hincks (San Francisco: ASP), in  
 3467 press. <https://dmtn-243.lsst.io>

- 3468 Naghib, E., Yoachim, P., Vanderbei, R. J., Connolly, A. J.,  
3469 & Jones, R. L. 2019, *The Astronomical Journal*, 157, 151,  
3470 doi: [10.3847/1538-3881/aafece](https://doi.org/10.3847/1538-3881/aafece)
- 3471 NSF-DOE Vera C. Rubin Observatory. 2021, Rubin  
3472 Observatory LSST Tutorials [Computer Software],  
3473 NSF-DOE Vera C. Rubin Observatory,  
3474 doi: [10.11578/rubin/dc.20250909.20](https://doi.org/10.11578/rubin/dc.20250909.20)
- 3475 NSF-DOE Vera C. Rubin Observatory. 2025a, Legacy  
3476 Survey of Space and Time Data Preview 1 [Data set],  
3477 NSF-DOE Vera C. Rubin Observatory,  
3478 doi: [10.71929/RUBIN/2570308](https://doi.org/10.71929/RUBIN/2570308)
- 3479 NSF-DOE Vera C. Rubin Observatory. 2025b, Legacy  
3480 Survey of Space and Time Data Preview 1: raw dataset  
3481 type [Data set], NSF-DOE Vera C. Rubin Observatory,  
3482 doi: [10.71929/RUBIN/2570310](https://doi.org/10.71929/RUBIN/2570310)
- 3483 NSF-DOE Vera C. Rubin Observatory. 2025c, Legacy  
3484 Survey of Space and Time Data Preview 1: visit\_image  
3485 dataset type [Data set], NSF-DOE Vera C. Rubin  
3486 Observatory, doi: [10.71929/RUBIN/2570311](https://doi.org/10.71929/RUBIN/2570311)
- 3487 NSF-DOE Vera C. Rubin Observatory. 2025d, Legacy  
3488 Survey of Space and Time Data Preview 1:  
3489 template\_coadd dataset type [Data set], NSF-DOE Vera  
3490 C. Rubin Observatory, doi: [10.71929/RUBIN/2570314](https://doi.org/10.71929/RUBIN/2570314)
- 3491 NSF-DOE Vera C. Rubin Observatory. 2025e, Legacy  
3492 Survey of Space and Time Data Preview 1:  
3493 difference\_image dataset type [Data set], NSF-DOE Vera  
3494 C. Rubin Observatory, doi: [10.71929/RUBIN/2570312](https://doi.org/10.71929/RUBIN/2570312)
- 3495 NSF-DOE Vera C. Rubin Observatory. 2025f, Legacy  
3496 Survey of Space and Time Data Preview 1: Source  
3497 searchable catalog [Data set], NSF-DOE Vera C. Rubin  
3498 Observatory, doi: [10.71929/RUBIN/2570323](https://doi.org/10.71929/RUBIN/2570323)
- 3499 NSF-DOE Vera C. Rubin Observatory. 2025g, Legacy  
3500 Survey of Space and Time Data Preview 1: Object  
3501 searchable catalog [Data set], NSF-DOE Vera C. Rubin  
3502 Observatory, doi: [10.71929/RUBIN/2570325](https://doi.org/10.71929/RUBIN/2570325)
- 3503 NSF-DOE Vera C. Rubin Observatory. 2025h, Legacy  
3504 Survey of Space and Time Data Preview 1: ForcedSource  
3505 searchable catalog [Data set], NSF-DOE Vera C. Rubin  
3506 Observatory, doi: [10.71929/RUBIN/2570327](https://doi.org/10.71929/RUBIN/2570327)
- 3507 NSF-DOE Vera C. Rubin Observatory. 2025i, Legacy  
3508 Survey of Space and Time Data Preview 1: DiaSource  
3509 searchable catalog [Data set], NSF-DOE Vera C. Rubin  
3510 Observatory, doi: [10.71929/RUBIN/2570317](https://doi.org/10.71929/RUBIN/2570317)
- 3511 NSF-DOE Vera C. Rubin Observatory. 2025j, Legacy  
3512 Survey of Space and Time Data Preview 1: DiaObject  
3513 searchable catalog [Data set], NSF-DOE Vera C. Rubin  
3514 Observatory, doi: [10.71929/RUBIN/2570319](https://doi.org/10.71929/RUBIN/2570319)
- 3515 NSF-DOE Vera C. Rubin Observatory. 2025k, Legacy  
3516 Survey of Space and Time Data Preview 1:  
3517 ForcedSourceOnDiaObject searchable catalog [Data set],  
3518 NSF-DOE Vera C. Rubin Observatory,  
3519 doi: [10.71929/RUBIN/2570321](https://doi.org/10.71929/RUBIN/2570321)
- 3520 NSF-DOE Vera C. Rubin Observatory. 2025l, Legacy  
3521 Survey of Space and Time Data Preview 1: SSOBJect  
3522 searchable catalog [Data set], NSF-DOE Vera C. Rubin  
3523 Observatory, doi: [10.71929/RUBIN/2570335](https://doi.org/10.71929/RUBIN/2570335)
- 3524 NSF-DOE Vera C. Rubin Observatory. 2025m, Legacy  
3525 Survey of Space and Time Data Preview 1: SSSource  
3526 searchable catalog [Data set], NSF-DOE Vera C. Rubin  
3527 Observatory, doi: [10.71929/RUBIN/2570333](https://doi.org/10.71929/RUBIN/2570333)
- 3528 NSF-DOE Vera C. Rubin Observatory. 2025n, Legacy  
3529 Survey of Space and Time Data Preview 1: CcdVisit  
3530 searchable catalog [Data set], NSF-DOE Vera C. Rubin  
3531 Observatory, doi: [10.71929/RUBIN/2570331](https://doi.org/10.71929/RUBIN/2570331)
- 3532 NSF-DOE Vera C. Rubin Observatory. 2025o, Legacy  
3533 Survey of Space and Time Data Preview 1: survey  
3534 property dataset type [Data set], NSF-DOE Vera C.  
3535 Rubin Observatory, doi: [10.71929/RUBIN/2570315](https://doi.org/10.71929/RUBIN/2570315)
- 3536 Oke, J. B., & Gunn, J. E. 1983, *ApJ*, 266, 713,  
3537 doi: [10.1086/160817](https://doi.org/10.1086/160817)
- 3538 O'Mullane, W., Economou, F., Huang, F., et al. 2024a, in  
3539 *Astronomical Society of the Pacific Conference Series*,  
3540 Vol. 535, *Astronomical Data Analysis Software and Systems*  
3541 XXXI, ed. B. V. Hugo, R. Van Rooyen, & O. M.  
3542 Smirnov, 227, doi: [10.48550/arXiv.2111.15030](https://doi.org/10.48550/arXiv.2111.15030)
- 3543 O'Mullane, W., AlSayyad, Y., Chiang, J., et al. 2024b, in  
3544 *Society of Photo-Optical Instrumentation Engineers*  
3545 (SPIE) Conference Series, Vol. 13101, *Software and*  
3546 *Cyberinfrastructure for Astronomy VIII*, ed. J. Ibsen &  
3547 G. Chiozzi, 131012B, doi: [10.1117/12.3018005](https://doi.org/10.1117/12.3018005)
- 3548 Onken, C. A., Wolf, C., Bessell, M. S., et al. 2019, *PASA*,  
3549 36, e033, doi: [10.1017/pasa.2019.27](https://doi.org/10.1017/pasa.2019.27)
- 3550 Park, H. Y., Nomerotski, A., & Tsybychev, D. 2017,  
3551 *Journal of Instrumentation*, 12, C05015,  
3552 doi: [10.1088/1748-0221/12/05/C05015](https://doi.org/10.1088/1748-0221/12/05/C05015)
- 3553 Petrosian, V. 1976, *ApJL*, 210, L53,  
3554 doi: [10.1086/18230110.1086/182253](https://doi.org/10.1086/18230110.1086/182253)
- 3555 Plazas, A. A., Shapiro, C., Smith, R., Huff, E., & Rhodes,  
3556 J. 2018, *Publications of the Astronomical Society of the*  
3557 *Pacific*, 130, 065004, doi: [10.1088/1538-3873/aab820](https://doi.org/10.1088/1538-3873/aab820)
- 3558 Plazas Malagón, A. A., Digel, S. W., Roodman, A.,  
3559 Broughton, A., & LSST Camera Team. 2025, *LSSTCam*  
3560 *and LSSTComCam Focal Plane Layouts*, Camera  
3561 Technical Note CTN-001, NSF-DOE Vera C. Rubin  
3562 Observatory, doi: [10.71929/rubin/2584019](https://doi.org/10.71929/rubin/2584019)

- 3563 Plazas Malagón, A. A., Waters, C., Broughton, A., et al.  
3564 2025, *Journal of Astronomical Telescopes, Instruments,*  
3565 *and Systems*, 11, 011209,  
3566 doi: [10.1117/1.JATIS.11.1.011209](https://doi.org/10.1117/1.JATIS.11.1.011209)
- 3567 Porter, M. N., Tucker, D. L., Smith, J. A., & Adair, C. L.  
3568 2025, *Photometric Transformation Relations for the*  
3569 *LSST Data Preview 1*, Technical Note RTN-099,  
3570 NSF-DOE Vera C. Rubin Observatory,  
3571 doi: [10.71929/rubin/3006074](https://doi.org/10.71929/rubin/3006074)
- 3572 Refregier, A. 2003, *ARA&A*, 41, 645,  
3573 doi: [10.1146/annurev.astro.41.111302.102207](https://doi.org/10.1146/annurev.astro.41.111302.102207)
- 3574 Reiss, D. J., & Lupton, R. H. 2016, *Implementation of*  
3575 *Image Difference Decorrelation*, Data Management  
3576 Technical Note DMTN-021, NSF-DOE Vera C. Rubin  
3577 Observatory, doi: [10.71929/rubin/2586490](https://doi.org/10.71929/rubin/2586490)
- 3578 Roodman, A., Rasmussen, A., Bradshaw, A., et al. 2024, in  
3579 *Society of Photo-Optical Instrumentation Engineers*  
3580 *(SPIE) Conference Series*, Vol. 13096, *Ground-based and*  
3581 *Airborne Instrumentation for Astronomy X*, ed. J. J.  
3582 Bryant, K. Motohara, & J. R. D. Vernet, 130961S,  
3583 doi: [10.1117/12.3019698](https://doi.org/10.1117/12.3019698)
- 3584 Rubin, V. C., & Ford, Jr., W. K. 1970, *ApJ*, 159, 379,  
3585 doi: [10.1086/150317](https://doi.org/10.1086/150317)
- 3586 Rubin, V. C., Ford, Jr., W. K., & Thonnard, N. 1980, *ApJ*,  
3587 238, 471, doi: [10.1086/158003](https://doi.org/10.1086/158003)
- 3588 Rubin Observatory Science Pipelines Developers. 2025, *The*  
3589 *LSST Science Pipelines Software: Optical Survey*  
3590 *Pipeline Reduction and Analysis Environment*, Project  
3591 Science Technical Note PSTN-019, NSF-DOE Vera C.  
3592 Rubin Observatory, doi: [10.71929/rubin/2570545](https://doi.org/10.71929/rubin/2570545)
- 3593 Rubin's Survey Cadence Optimization Committee, Bauer,  
3594 F. E., Brough, S., et al. 2022, *Survey Cadence*  
3595 *Optimization Committee's Phase 1 Recommendation*,  
3596 Project Science Technical Note PSTN-053, NSF-DOE  
3597 Vera C. Rubin Observatory, doi: [10.71929/rubin/2584276](https://doi.org/10.71929/rubin/2584276)
- 3598 Rubin's Survey Cadence Optimization Committee, Bauer,  
3599 F. E., Bianco, F. B., et al. 2023, *Survey Cadence*  
3600 *Optimization Committee's Phase 2 Recommendations*,  
3601 Project Science Technical Note PSTN-055, NSF-DOE  
3602 Vera C. Rubin Observatory, doi: [10.71929/rubin/2585249](https://doi.org/10.71929/rubin/2585249)
- 3603 Rubin's Survey Cadence Optimization Committee, Bianco,  
3604 F. B., Jones, R. L., et al. 2025, *Survey Cadence*  
3605 *Optimization Committee's Phase 3 Recommendations*,  
3606 Project Science Technical Note PSTN-056, NSF-DOE  
3607 Vera C. Rubin Observatory, doi: [10.71929/rubin/2585402](https://doi.org/10.71929/rubin/2585402)
- 3608 Rykoff, E. S., Tucker, D. L., Burke, D. L., et al. 2023, *arXiv*  
3609 *e-prints*, arXiv:2305.01695,  
3610 doi: [10.48550/arXiv.2305.01695](https://doi.org/10.48550/arXiv.2305.01695)
- 3611 Saunders, C. 2024, *Astrometric Calibration in the LSST*  
3612 *Pipeline*, Data Management Technical Note DMTN-266,  
3613 NSF-DOE Vera C. Rubin Observatory,  
3614 doi: [10.71929/rubin/2583846](https://doi.org/10.71929/rubin/2583846)
- 3615 Schutt, T., Jarvis, M., Roodman, A., et al. 2025, *The Open*  
3616 *Journal of Astrophysics*, 8, 26, doi: [10.33232/001c.132299](https://doi.org/10.33232/001c.132299)
- 3617 Sérsic, J. L. 1963, *Boletín de la Asociación Argentina de*  
3618 *Astronomía La Plata Argentina*, 6, 41
- 3619 Sersic, J. L. 1968, *Atlas de Galaxias Australes (Cordoba,*  
3620 *Argentina: Observatorio Astronomico)*
- 3621 Shanks, T., Metcalfe, N., Chehade, B., et al. 2015,  
3622 *MNRAS*, 451, 4238, doi: [10.1093/mnras/stv1130](https://doi.org/10.1093/mnras/stv1130)
- 3623 SLAC National Accelerator Laboratory, & NSF-DOE Vera  
3624 C. Rubin Observatory. 2024, *LSST Commissioning*  
3625 *Camera*, SLAC National Accelerator Laboratory (SLAC),  
3626 Menlo Park, CA (United States),  
3627 doi: [10.71929/RUBIN/2561361](https://doi.org/10.71929/RUBIN/2561361)
- 3628 Slater, C. T., Ivezić, Ž., & Lupton, R. H. 2020, *AJ*, 159, 65,  
3629 doi: [10.3847/1538-3881/ab6166](https://doi.org/10.3847/1538-3881/ab6166)
- 3630 Smith, G. E. 2010, *Rev. Mod. Phys.*, 82, 2307,  
3631 doi: [10.1103/RevModPhys.82.2307](https://doi.org/10.1103/RevModPhys.82.2307)
- 3632 Stalder, B., Reil, K., Claver, C., et al. 2020, in *Society of*  
3633 *Photo-Optical Instrumentation Engineers (SPIE)*  
3634 *Conference Series*, Vol. 11447, *Ground-based and*  
3635 *Airborne Instrumentation for Astronomy VIII*, ed. C. J.  
3636 Evans, J. J. Bryant, & K. Motohara, 114470L,  
3637 doi: [10.1117/12.2561132](https://doi.org/10.1117/12.2561132)
- 3638 Stalder, B., Reil, K., Aguilar, C., et al. 2022, in *Society of*  
3639 *Photo-Optical Instrumentation Engineers (SPIE)*  
3640 *Conference Series*, Vol. 12184, *Ground-based and*  
3641 *Airborne Instrumentation for Astronomy IX*, ed. C. J.  
3642 Evans, J. J. Bryant, & K. Motohara, 121840J,  
3643 doi: [10.1117/12.2630184](https://doi.org/10.1117/12.2630184)
- 3644 Stalder, B., Munoz, F., Aguilar, C., et al. 2024, in *Society*  
3645 *of Photo-Optical Instrumentation Engineers (SPIE)*  
3646 *Conference Series*, Vol. 13094, *Ground-based and*  
3647 *Airborne Telescopes X*, ed. H. K. Marshall, J. Spyromilio,  
3648 & T. Usuda, 1309409, doi: [10.1117/12.3019266](https://doi.org/10.1117/12.3019266)
- 3649 Swinbank, J. D., Axelrod, T. S., Becker, A. C., et al. 2020,  
3650 *Data Management Science Pipelines Design*, Data  
3651 Management Controlled Document LDM-151, NSF-DOE  
3652 Vera C. Rubin Observatory, doi: [10.71929/rubin/2587108](https://doi.org/10.71929/rubin/2587108)
- 3653 Taranu, D. S. 2025, *The MultiProFit astronomical source*  
3654 *modelling code*, Data Management Technical Note  
3655 DMTN-312, NSF-DOE Vera C. Rubin Observatory,  
3656 doi: [10.71929/rubin/2584108](https://doi.org/10.71929/rubin/2584108)
- 3657 Taylor, M. 2011, *TOPCAT: Tool for OPerations on*  
3658 *Catalogues And Tables*, *Astrophysics Source Code*  
3659 *Library*, record ascl:1101.010

- 3660 Thomas, S., Connolly, A., Crenshaw, J. F., et al. 2023, in  
3661 Adaptive Optics for Extremely Large Telescopes  
3662 (AO4ELT7), 67, doi: [10.13009/AO4ELT7-2023-069](https://doi.org/10.13009/AO4ELT7-2023-069)
- 3663 Tonry, J. L., Denneau, L., Heinze, A. N., et al. 2018, PASP,  
3664 130, 064505, doi: [10.1088/1538-3873/aabadf](https://doi.org/10.1088/1538-3873/aabadf)
- 3665 Wainer, T. M., Davenport, J. R. A., Bellm, E. C., et al.  
3666 2025, Research Notes of the American Astronomical  
3667 Society, 9, 171, doi: [10.3847/2515-5172/adecef](https://doi.org/10.3847/2515-5172/adecef)
- 3668 Wang, D. L., Monkewitz, S. M., Lim, K.-T., & Becla, J.  
3669 2011, in State of the Practice Reports, SC '11 (New  
3670 York, NY, USA: ACM), 12:1–12:11,  
3671 doi: [10.1145/2063348.2063364](https://doi.org/10.1145/2063348.2063364)
- 3672 Waters, C. Z., Magnier, E. A., Price, P. A., et al. 2020,  
3673 ApJS, 251, 4, doi: [10.3847/1538-4365/abb82b](https://doi.org/10.3847/1538-4365/abb82b)
- 3674 Whitaker, K. E., Ashas, M., Illingworth, G., et al. 2019,  
3675 ApJS, 244, 16, doi: [10.3847/1538-4365/ab3853](https://doi.org/10.3847/1538-4365/ab3853)
- 3676 Wu, X., Roby, W., Goldian, T., et al. 2019, in Astronomical  
3677 Society of the Pacific Conference Series, Vol. 521,  
3678 Astronomical Data Analysis Software and Systems  
3679 XXVI, ed. M. Molinaro, K. Shortridge, & F. Pasian, 32
- 3680 Xin, B., Claver, C., Liang, M., et al. 2015, ApOpt, 54,  
3681 9045, doi: [10.1364/AO.54.009045](https://doi.org/10.1364/AO.54.009045)
- 3682 Yoachim, P. 2022, Survey Strategy: Rolling Cadence,  
3683 Project Science Technical Note PSTN-052, NSF-DOE  
3684 Vera C. Rubin Observatory, doi: [10.71929/rubin/2584109](https://doi.org/10.71929/rubin/2584109)
- 3685 Yoachim, P., Jones, L., Eric H. Neilsen, J., & Becker, M. R.  
3686 2024, lsst/rubin\_scheduler: v3.0.0, v3.0.0 Zenodo,  
3687 doi: [10.5281/zenodo.13985198](https://doi.org/10.5281/zenodo.13985198)
- 3688 Zhang, T., Almoubayyed, H., Mandelbaum, R., et al. 2023,  
3689 MNRAS, 520, 2328, doi: [10.1093/mnras/stac3350](https://doi.org/10.1093/mnras/stac3350)